NONLINEAR CONTROL SCHEMES FOR EXTREMUM POWER SEEKING AND TORSIONAL VIBRATION MITIGATION IN VARIABLE SPEED WIND TURBINE SYSTEMS

by

FARIBA FATEH

M.S., Marquette University, 2005

AN ABSTRACT OF A DISSERTATION

submitted in partial fulfillment of the requirements for the degree

DOCTOR OF PHILOSOPHY

Department of Electrical and Computer Engineering
College of Engineering

KANSAS STATE UNIVERSITY
Manhattan, Kansas

2015

Abstract

This dissertation presents nonlinear control schemes to improve the productivity and lifespan of doubly fed induction generator (DFIG)-based and permanent magnet generator (PMG)-based variable speed wind turbines. To improve the productivity, a nonlinear adaptive control scheme is developed to maximize power capture. This controller consists of three feedback loops. The first loop controls electrical torque of the generator in order to cancel the nonlinear term of the turbine equation of motion using the feedback linearization concept. The nonlinearity cancelation requires a real-time estimation of aerodynamic torque. This is achieved through a second loop which estimates the ratio of the wind turbine power capture versus the available wind power. A third loop utilizes this estimate to identify the shaft speed at which the wind turbine operates at a greater power output. Contrary to existing techniques in literature, this innovative technique does not require any prior knowledge of the optimum tip speed ratio. The presented technique does not need a dither or perturbation signal to track the optimum shaft speed at the maximum power capture. These features make this technique superior to existing methods.

Furthermore, the lifespan of variable speed wind turbines is improved by reducing stress on the wind turbine drivetrain. This is achieved via developing a novel vibration mitigation technique using sliding-mode control theory. The technique measures only generator speed as the input signal and then passes it through a high-pass filter in order to extract the speed variations. The filtered signal and its integral are then passed through identical band-pass filters centered at the dominant natural frequency of the drivetrain. These two signals formulate a sliding surface and consequently a control law to damp the drivetrain torsional stress oscillations caused by electrical and mechanical disturbances. This technique provides a robust mitigation approach compared with existing techniques. These control schemes are verified through holistic models of DFIG- and PMG-based wind turbines. Except for wind turbine aerodynamics, for which an existing simulator is used, the developed models of all components including DFIG, PMG, converters, multi-mass drivetrain, and power line are presented in this dissertation.

NONLINEAR CONTROL SCHEMES FOR EXTREMUM POWER SEEKING AND TORSIONAL VIBRATION MITIGATION IN VARIABLE SPEED WIND TURBINE SYSTEMS

by

FARIBA FATEH

M.S., Marquette University, 2005

A DISSERTATION

submitted in partial fulfillment of the requirements for the degree

DOCTOR OF PHILOSOPHY

Department of Electrical and Computer Engineering
College of Engineering

KANSAS STATE UNIVERSITY
Manhattan, Kansas

2015

Approved by:

Co-Major Professor
Dr. Warren White

Approved by:

Co-Major Professor
Dr. Don Gruenbacher

Copyright

Abstract

This dissertation presents nonlinear control schemes to improve the productivity and lifespan of doubly fed induction generator (DFIG)-based and permanent magnet generator (PMG)-based variable speed wind turbines. To improve the productivity, a nonlinear adaptive control scheme is developed to maximize power capture. This controller consists of three feedback loops. The first loop controls electrical torque of the generator in order to cancel the nonlinear term of the turbine equation of motion using the feedback linearization concept. The nonlinearity cancelation requires a real-time estimation of aerodynamic torque. This is achieved through a second loop which estimates the ratio of the wind turbine power capture versus the available wind power. A third loop utilizes this estimate to identify the shaft speed at which the wind turbine operates at a greater power output. Contrary to existing techniques in literature, this innovative technique does not require any prior knowledge of the optimum tip speed ratio. The presented technique does not need a dither or perturbation signal to track the optimum shaft speed at the maximum power capture. These features make this technique superior to existing methods.

Furthermore, the lifespan of variable speed wind turbines is improved by reducing stress on the wind turbine drivetrain. This is achieved via developing a novel vibration mitigation technique using sliding-mode control theory. The technique measures only generator speed as the input signal and then passes it through a high-pass filter in order to extract the speed variations. The filtered signal and its integral are then passed through identical band-pass filters centered at the dominant natural frequency of the drivetrain. These two signals formulate a sliding surface and consequently a control law to damp the drivetrain torsional stress oscillations caused by electrical and mechanical disturbances. This technique provides a robust mitigation approach compared with existing techniques. These control schemes are verified through holistic models of DFIG- and PMG-based wind turbines. Except for wind turbine aerodynamics, for which an existing simulator is used, the developed models of all components including DFIG, PMG, converters, multi-mass drivetrain, and power line are presented in this dissertation.

Table of Contents

List of Figures

List of Tables

Acknowledgements

I would like to express my sincere gratitude to my PhD advisers, Dr. Warren White and Dr. Don Gruenbacher, for their guidance and advice while completing the work presented in my dissertation. I also would like to thank Dr. Medhat Morcos, Dr. Noel Schulz, and Dr. Caterina Scoglio, for serving on my dissertation committee and for their comments.

Special thanks to my husband, Behrooz, for his support throughout my graduate studies, and my lovely daughter, Saba, for her patience.

I wish to give heartfelt thanks to my parents. I am thankful to my mother for her unconditional love and care. My father will forever be my hero and role model in my life.

I am thankful to my brothers, Farhad and Ali, and friends for being my laughter and stress release when needed.

I also acknowledge the Electric Power Affiliation Program (EPAP) at Kansas State University for funding this research.

Dedication

To my daughter, Saba!

Chapter 1 – Introduction

This chapter begins with a brief background on the need for clean energy sources for electricity generation and a description of the growth of installed wind energy capacity in the past decade. Problem statements are expressed regarding two technical challenges of variable speed wind turbines, including extremum power seeking and mitigation of torsional vibrations. An overview of prior investigations of these two challenges is studied in order to provide a baseline for contributions presented in this dissertation. In this chapter, the objectives, main contributions, and published papers by the author on these subjects are also highlighted. This chapter concludes with the organization of the dissertation.

1.1 Background

Electricity generation worldwide reached 23,536 TWh in 2014 demonstrating 34% growth in usage during the past decade [1]. In particular, the United States, with 0.7% growth was the second largest electricity producer in 2014 generating 4,093 TWh, with energy resources of coal (38.8%), natural gas (27.4%), nuclear (19.5%), renewable energy sources (13.2%), and other (1.2%), as shown in Figure 1.1. This means that 67% of electricity generation in the United States

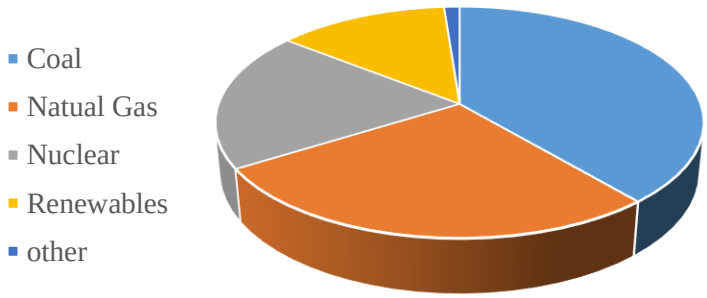

Figure 1.1 Energy sources of electricity generation in the United States in 2014 [1].

is produced from combustion of fossil fuels. Unfortunately, the carbon intensity of coal and natural gas thermal combustions are as high as 1029 kg/MWh, and 515kg/MWh, respectively [2] meaning that, for 1MWh electricity generation from power plants fueled by coal and natural gas, 1029 and 515 kg CO_2 are produced, respectively. A simple calculation, (i.e., $\{(0.388 \times 1029) + (0.274 \times 515)\}10^{-6} \times (4093)10^{18}$) tells us that 9073×10^{18} kg CO_2 pollution was emitted in 2014 alone for the 67% of electricity generation in the United States.

During the last decade, increased attention has been paid to employing renewable energy sources to solve environmental problems worldwide. Today, wind turbines are one of the most important renewable power sources for electricity generation. Installed capacity of wind turbines has grown from 48 GW in 2004 to 370 GW in 2014, as shown in Figure 1.2. The United States has the second largest share of installed capacity of wind turbines, with over 65 GW compared to the top three countries in the wind energy in 2014 (i.e., China, the United States, and Germany, share approximately 60% of the global wind energy generation market) [3], [4].

In addition to the growth in installed capacity, the size of wind turbines has grown over the last three decades because larger wind turbines have better power capturing and lower energy cost. Wind turbines currently in the power range of 4.5- 8 MW are being developed by most turbine

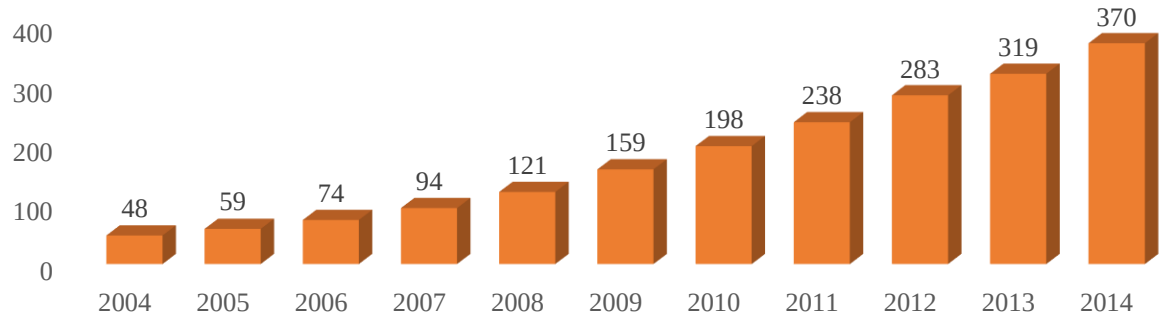

Figure 1.2 Wind energy capacity in GW in the past decade [3].

manufacturers and it is expected that larger wind turbines as high powered as 10MW will appear in 2018 for economic advantages [5].

Wind turbines indeed have some adverse environmental impacts, including noise and degradation of wildlife habitats. For example, spinning turbine blades with diameters as high as 120 m are a threat to flying wildlife such as birds and bats. However, in comparison to traditional energy generation resources, the wind provides a net environmental benefit to the world. In 2014, 4% of electricity generation in the United States was from wind energy, that is $\{(0.04 \times 1029)\}10^{-6} \times (4093)10^{18} = 169 \times 10^{12}$ kg less CO_2 was emitted compared to if the same amount of electricity would have been generated by coal thermal combustion power plants.

Presently, the wind energy market is demanding design optimization of high performance wind turbines for capital and maintenance cost reductions. Therefore, further active control schemes are required to reduce mechanical stress and to increase the lifespan of wind turbines. Application of advanced nonlinear adaptive control schemes can help capture more wind power, and thus improving efficiency of the overall system [6].

1.2 Problem Statement

Desired growth in wind energy provides motivation to conduct many investigations to improve *productivity* and *reliability* of these systems. A fundamental challenge of improving productivity of wind turbines is development of a robust control scheme for extremum power seeking in the presence of wind speed variations. A technical challenge for improving reliability and productivity is stress reduction in mechanical components through the mitigation of torsional vibrations caused by interaction between the wind turbine drivetrain and the rest of the system. These two concerns are elaborated in the following subsections.

1.2.1 *Extremum Power Seeking*

Power captured by wind turbines fluctuates due to the inherent variable nature of wind speed. As wind speed varies, maximum power, $P_{T\,MAX}$, that can be captured from a wind turbine occurs at various shaft speeds, as shown in Figure 1.3. Maximum power seeking is performed in the variable speed operational region, where the blade pitch angle is held constant and the electromagnetic torque and consequently rotor speed is controlled to track maximum wind power as wind speed varies. In the conventional technique, electrical torque is set to be proportional to the square of the rotor speed. However, the controller gain must be adaptively adjusted in real-time to obtain optimum results. Another set of techniques is known as the perturb-and-observe and hill-climbing techniques. However, the techniques may fail to seek maximum power in case of rapid wind speed changes. One challenge is to develop an adaptive technique with a higher dynamic performance than existing techniques in order to track the trajectory of maximum power points even in the event of sudden wind speed change.

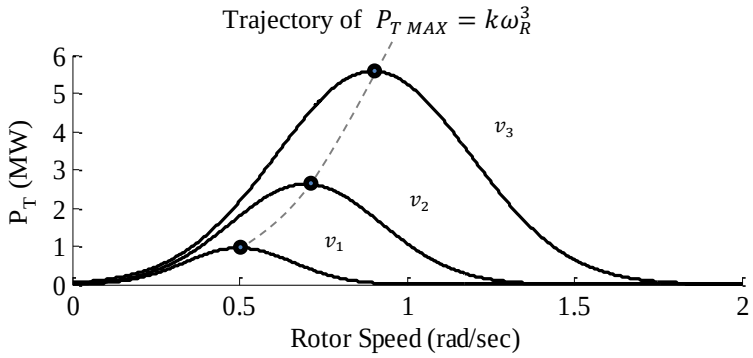

Figure 1.3 Captured power curves versus the rotor speed for various wind speeds.

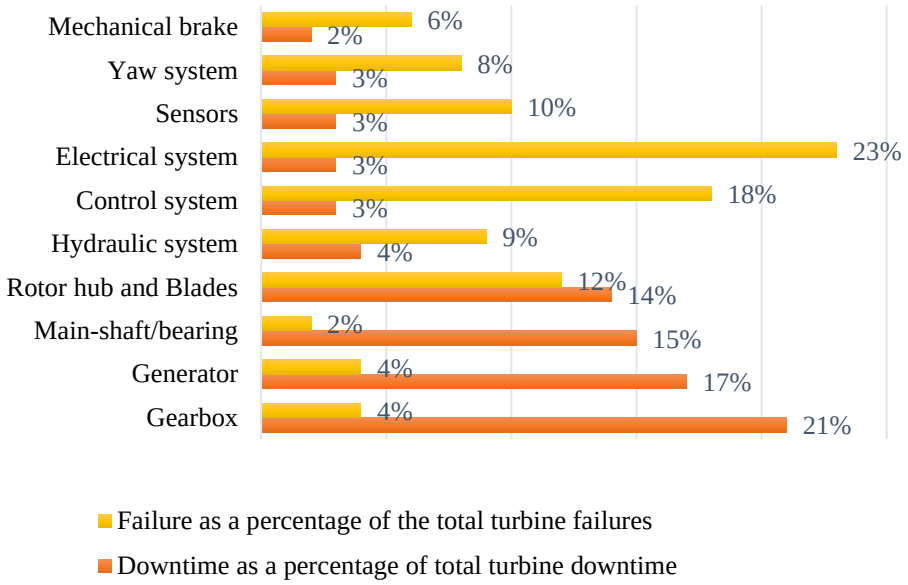

Figure 1.4 Failure and downtime percentages of wind turbine systems [7].

1.2.2 *Torsional Vibration Mitigation*

Torsional vibrations in the wind turbine drivetrain reduce the gearbox and shaft lifespans and increase wind turbine maintenance costs. Rapid changes in voltage magnitude (e.g., voltage sag, and transient phenomena such as a switching event in the power grid) can result in power oscillation and torsional vibrations in the drivetrain of wind turbines. The source of torsional vibrations can also originate from wind turbine aerodynamics (e.g., tower shadow and wind speed turbulence). In contrast to extremum power seeking, few investigations on internal gearbox torsional vibrations are reported in the literature. One technical challenge is to enhance the knowledge of torsional vibrations in order to increase the lifespan of wind turbines by reducing torsional vibrations caused by mechanical and electrical events. Figure 1.4 shows that failures of rotational components and the generator contribute the longest downtimes resulting in significant maintenance costs [7].

1.3 Brief Review of Previous Work

This section is divided into literature reviews of extremum power-seeking techniques and mitigation methods for torsional vibrations in wind turbines. This review is presented as an introduction to the contribution of this dissertation elaborated in Chapters 4 and 5.

1.3.1 *Extremum Power Seeking Techniques*

The literature describes many maximum power-capturing methods but all can be categorized into two main groups, as shown in Figure 1.5. Model-based methods require prior knowledge of turbine parameters in order to calculate the operating point. Non model-based methods rely on an iterative search of the optimum operating point using reference speed increments. In this subsection, some extremum power-seeking techniques for wind turbines are briefly reviewed. In the conventional control law, described by Leithead *et al*. in [8], and Johnson *et al.* in [9] and [10], desired electric torque is set to be proportional to the square of the rotor speed (*i.e.*, $k_{opt}\omega_R^2$). The square-law can best be understood from wind turbine power curves for different wind speeds, as discussed in Chapters 2 and 4. In wind turbines, trajectory of the maximum power falls in a $k_{opt}\omega_R^3$ curve as wind speed varies (Figure 1.3), meaning that the drivetrain torque must move on a $k_{opt}\omega_R^2$ curve. However, for a wide range of wind speed variation, the challenge is to adaptively find the optimal controller gain, k_{opt} [11]. Moreover, the maximum power trajectory

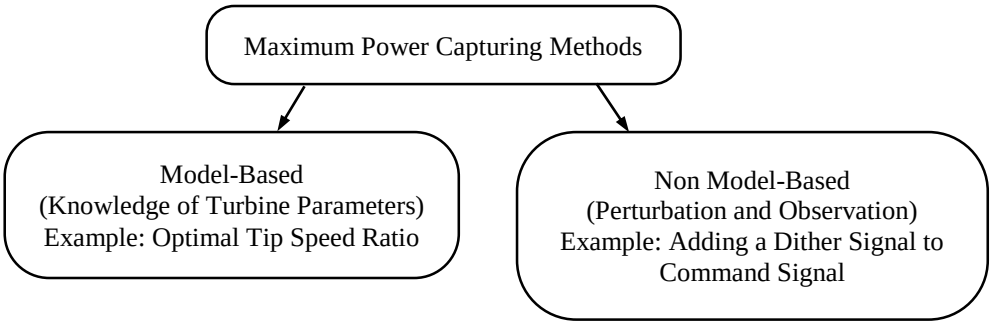

Figure 1.5 Extremum power seeking methods

moves with changes in environmental parameters (e.g., air-density) [12]. Thus, a lookup table methods, artificial intelligence algorithms, or adaptive control schemes may be implemented in conjunction with the square-law to find the real-time optimum value of the controller gain. The perturb-and-observe method, presented by Hawkins *et al.* in [13], uses the sign of the gradient of turbine captured-power with respect to rotor speed due to a perturbation added to the control signal. However, this technique can be sensitive to noise and perturbation size, particularly close to the power curve peak. Similarly, Ghaffari *et al.* [14] presented a maximum seeking algorithm using a sinusoidal dither signal added to the reference (command) rotor speed to estimate the gradient of the output power with respect to rotor speed. The dither signal frequency must be low and its amplitude should be sufficiently small compared to the rotor speed [14]. In these techniques, one major problem that can lead to failure of the seeking process is lack of distinction between power differences resulting from wind changes and those resulting from a power change due to adding a perturbation [11]. Fuzzy logic and neural network algorithms have also been used to reduce uncertainties faced by extremum power seeking in wind turbines [15], [16], [17], [18]. Two of those methods are briefly reviewed in this section. Simoes *et al.* [16] applied a fuzzy logic controller superimposed onto the hill-climbing concept. In this technique, the fuzzy controller updates the value of rotor speed change, $\Delta\omega_R$, in each hill-climbing step to track maximum output power. Although the technique is a non model-based method and insensitive to noisy signals, a rule-base table and membership functions are required as prior knowledge. Hui Li *et al.* [17] presented a technique based on the optimum tip-speed ratio as a known feature for a wind turbine. Therefore, wind speed is estimated using a neural network algorithm. In this scheme, input signals are the measured power and rotor speed, and the output is the desired rotor speed. Another neural network scheme is used to compensate for potential drift of the wind turbine power coefficient due

to environmental variations. This is performed by utilizing a pseudo-power curve. Adaptive control schemes have also been used to improve maximum power capture methods [19] [20] [21] [22] [23]. Two of those methods are briefly reviewed in this section. Iyasere *et al.* [21] presented a nonlinear control (electrical) torque that simultaneously minimizes errors between measured and desired values of blade pitch angle and rotor speed while the maximum power capture coefficient is considered as a known parameter for a wind turbine. Desired values of rotor speed and blade pitch angle are also updated in real-time, when the first and second derivatives of the desired variables are bounded. In this technique wind speed is assumed to be constant or slowly varying with time. Beltran, *et al.* [22] presented a hybrid technique in which a second order sliding mode controller is combined with the conventional square-law torque control. In this technique, mechanical (or aerodynamic) torque is estimated using a second order sliding mode observer, and an error is defined as the difference between the estimated torque and optimum torque values. Then, a second order sliding mode controller is designed to calculate desired electrical torque such that the error approaches zero in a finite time. In this technique, the optimum value of the square-law gain is considered as a known parameter for a wind turbine.

1.3.2 *Torsional Vibration Mitigation Techniques*

Recent investigations have shown that torsional vibrations in wind turbines can be mitigated by controlling generator torque through generator-side converter [7], [24], [25] and flexible ac transmission system (FACTS)-devices [26], [27], [28]. FACTS devices can mitigate power oscillations in the power grid as well as resultant torsional vibrations. However, FACTS devices cannot mitigate torsional vibrations caused by wind turbine aerodynamics. However, torsional vibrations caused by mechanical or electrical events can effectively be mitigated by adding a virtual inertia, damping, or stiffness component to generator torque as a compensation

torque as shown in Figure 1.6. In the following section, some of these methods are briefly reviewed.

Active damping of torsional vibrations caused by the tower shadow effect or resonance that occurs when the blades pass in front of the tower was addressed in [7] in which, the dominant resonant mode is damped by adding virtual inertia in the compensating torque. In [24], another generator torque control strategy was presented for decreasing mechanical stress caused by electric torque disturbances. The generator-side converter can create compensation torque components at dominant drivetrain natural frequencies that are superimposed on the normal torque in order to suppress mechanical vibrations. This methodology has been implemented in various approaches. For example, in [7], the virtual inertia controller (VIC) method was used to damp torsional vibrations caused by the tower shadow effect. In the VIC method, the first derivative of the generator speed is used as the input signal to create deceleration torque, which is added to the reference torque only at the dominant drivetrain natural frequency. The generator speed has also been used to create virtual damping torque at drivetrain natural frequencies in order to mitigate torsional vibrations caused by a step change in the generator torque [24], [25]. FACTS devices can also be employed to mitigate the sub-synchronous resonance (SSR) phenomenon [28]. For

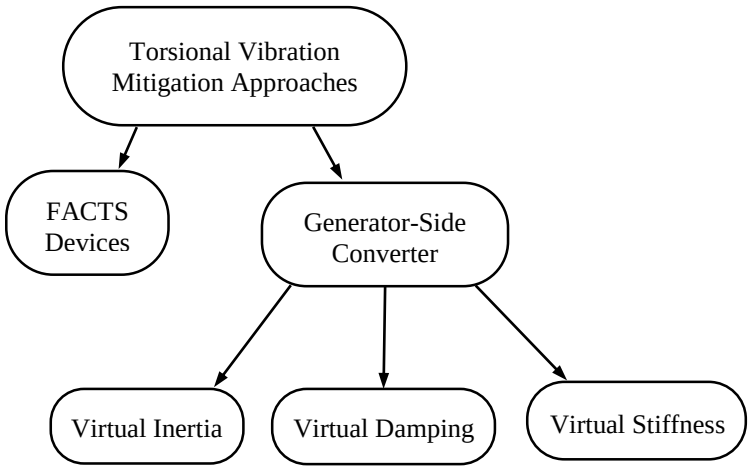

Figure 1.6 Mitigation approaches for torsional vibrations in wind turbines.

example, a gate-controlled series capacitor (GCSC), which contains a pair of switches in parallel with a capacitor and enables control of transmission line effective reactance and power flow, was used for SSR damping in [26].

1.4 Objectives of the Dissertation

Objectives of this dissertation are:

- To improve the *productivity* of wind turbines by developing novel nonlinear control schemes for extremum power seeking, and torsional vibration mitigation.
- To improve the *reliability* and *lifespan* of wind turbines using nonlinear control scheme for torsional vibration mitigation.

1.5 Scopes and Contributions of the Dissertation

The scope of this dissertation is horizontal axis variable speed wind turbines. Figure 1.7 shows the types of wind turbines that fall into this category. The main focus of this dissertation is on the second operational region of wind turbines where the pitch angle is held constant and shaft speed is controlled to capture maximum available wind power. The three main contributions of this dissertation are highlighted in the following paragraphs.

In this dissertation, holistic models of doubly fed induction generator DFIG- and permanent magnet generator PMG-based wind turbines, including state-space representations of generators, converters, controllers, power lines, and multi-mass drivetrains/gearboxes are developed in the Matlab/Simulink environment (based on existing knowledge [7], [29]) connected to the FAST (Fatigue, Aerodynamics, Structures, and Turbulence) simulator [30], [31]. This work is noticeable because most investigators who have studied wind turbines have mainly focused on mechanical or electrical aspects, while the presented model provides a comprehensive electro-mechanical

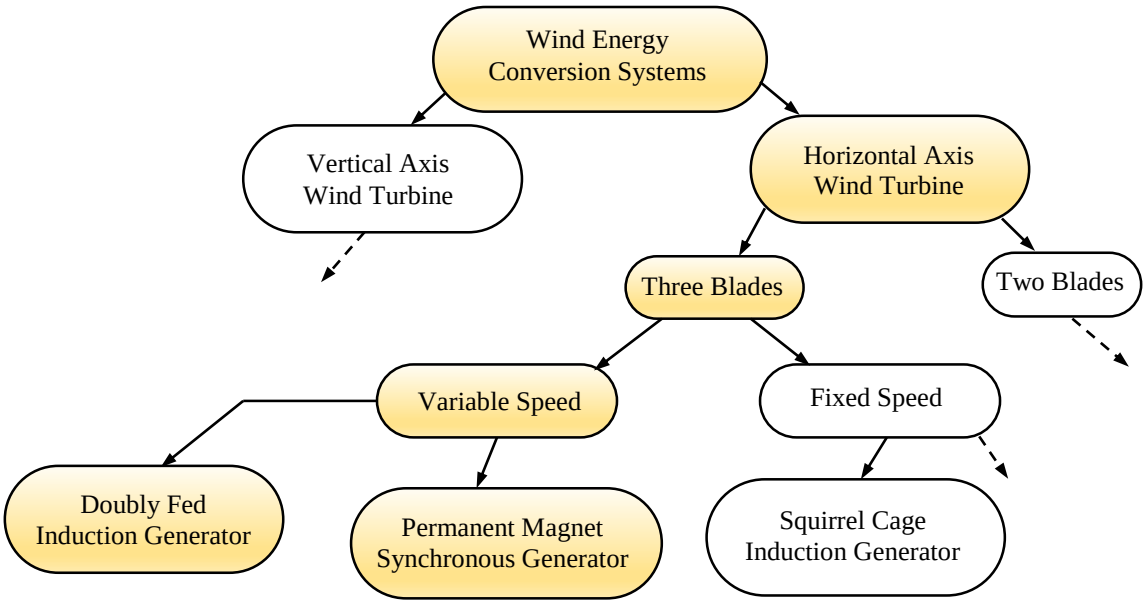

Figure 1.7. Scopes of the research

system. FAST is an open access code written by the National Renewable Energy Laboratory (NREL) in the Fortran programming language that emulates the aerodynamics of horizontal axis wind turbines including interactions of wind with turbine tower, blades, and nacelle that can be used in the Matlab/Simulink environment as an S-function block [32]. Models developed in this dissertation can be easily connected to the FAST simulator with capabilities of emulating various mechanical and electrical disturbances, and examining internal oscillations and interactions between subsystems.

For the second contribution of this dissertation, a novel nonlinear adaptive maximum power-seeking technique is developed for variable speed (DFIG)-based and (PMG)-based wind turbines [33], [34]. The presented technique is a novel version of the conventional method (i.e. the electrical torque is proportional to the square of the rotor speed), in which the proportional-coefficient is adaptively adjusted in real-time through three control laws. The first control law calculates the desired electrical torque using feedback linearization, assuming that the power

capture coefficient and the desired rotor speed are instantaneously identified. The second control law estimates real-time values of the power capture coefficient from a Lyapunov-based analysis, and the third control law provides the desired rotor speed. These control laws cause the turbine to adaptively adjust the rotor speed towards a desired speed in which the operating point moves in the direction of increasing the power capture coefficient. The proposed maximum power seeking method differs distinctly from the perturb-and-observe scheme by eliminating the need to add a dither or perturbation signal and robustly tracking the trajectory of maximum power points even in the event of a sudden wind speed change that would cause the perturb-and-observe technique to fail. Findings of this power capture work were validated using models developed for a 5 MW wind turbine model. The significance of the presented technique as compared to the aforementioned methods is that neither a perturbation signal, a lookup table, nor a power measurement is required. Also, the maximum power capture coefficient and the optimum tip-speed ratio are not assumed as known parameters. The presented technique demonstrates appropriate dynamic performance in the presence of wind turbulence and sudden speed changes, while some existing techniques are validated only for slowly varying wind speed.

The third contribution of this dissertation is a novel method to increase the lifespan of wind turbines by reducing torsional vibrations caused by mechanical or electrical events. The presented method uses only rotor speed as the feedback signal to create compensation torque, which is superimposed on the extremum power-seeking torque. This method is examined in a five-mass drivetrain of a (DFIG)-based and a (PMG)-based wind turbines. The simulated model includes aerodynamics of a 750kW wind turbine, as well as dynamics of the generator, gearbox, and back-to-back power converters. The presented control scheme is investigated for various scenarios to damp the drivetrain torsional vibrations including; a voltage dip occurring on the power grid,

switching of a series capacitor in the power line, and a wind speed variation [35], [36], [37]. The effectiveness of the new control method is investigated through simulations. Simulation results demonstrated that mechanical disturbances have similar impacts on the drivetrain torsional vibrations in DFIG-based and PMG-based wind turbines. However, electrical disturbances have more impacts on drivetrains in DFIG-based wind turbines than in PMG-based wind turbines.

1.6 Publications

Parts of the results presented in this dissertation can be found in the following articles.

1. Fariba Fateh, Warren N. White, and Don Gruenbacher, "A Maximum Power Seeking Technique for Grid-Connected DFIG-Based Wind Turbines," *the IEEE Journal of Emerging and Selected Topics in Power Electronics*, vol. 3, no.4 pp. 957 – 966, Oct. 2015.
2. Warren N. White, Fariba Fateh, and Don Gruenbacher, "Impact of Sliding Mode Bandwidth and Disturbance Estimation on Damping of Wind Turbine Torsional Vibration," (Invited paper) *in the Processing of the American Control Conference*, Boston, MA, July 2016.
3. Fariba Fateh, Warren N. White, and Don Gruenbacher, "Torsional Vibrations in the Drivetrain of DFIG- and PMG-based Wind Turbines — Comparison and Mitigation" (Invited paper) *in the Processing of the ASME Dynamic Systems and Control Conference*, Columbus, Ohio, Oct. 2015.
4. Fariba Fateh, Warren N. White, and Don Gruenbacher, "Mitigation of Torsional Vibrations in the Drivetrain of DFIG-based Grid-Connected Wind Turbine," *in the Processing of the IEEE Energy Convers Congress & Exposition*, Montreal, Quebec, Sep. 2015.
5. Warren N. White, Fariba Fateh, and Don Gruenbacher, "Torsional Resonance Active Damping in Grid Tied Wind Turbines with Gearbox, DFIG, and Power Converters," *in the Processing of the American Control Conference*, Chicago, Illinois, July 2015.
6. Fariba Fateh, Warren N. White, and Don Gruenbacher, "A Nonlinear Control Scheme for Extremum Power Seeking in Wind Turbine Energy Conversion Systems," *in the Processing of the American Control Conference*, Portland, Oregon, June 2014.

1.7 Organization of the Dissertation

In addition to this chapter, this dissertation is organized as follows

Chapter 2 begins with a description of topologies of wind turbine systems followed by, main formulations of the aerodynamics of wind turbines and the tool used in this dissertation to study all nonlinearities of wind turbine aerodynamics. A method to include a multi-mass drivetrain into the wind turbine system is also presented in details. At the end of the chapter, natural frequencies of a five-mass drivetrain are formulated to be used for analytical analysis and design of the torsional vibration mitigation technique described in Chapter 5.

All mathematical formulations of electrical parts of DFIG-based and PMG-based wind turbine systems are derived in Chapter 3. These formulations are used to develop block diagram representations of a doubly fed induction generator, permanent magnet synchronous generator, generator-side and grid-side converters, output filter of grid-side converter, power line between the grid and wind turbine system, and series capacitor compensation. In addition, the overall system is built in the Matlab/Simulink environment using the developed electrical and mechanical block diagrams and FAST simulator, and verified on overall dynamic behaviors of DFIG-based and PMG-based wind turbine systems.

In Chapter 4, background on two main maximum power seeking techniques is first presented followed by nonlinear Lyapunov and feedback linearization techniques as a background for deriving control laws later in the chapter. The proposed extremum-seeking technique developed based on nonlinear feedback linearization and Lyapunov function theories is presented and analyzed for DFIG-based and PMG-based wind turbines. The developed control scheme is verified on 5MW DFIG-based and PMG-based wind turbine systems. Also, a sensitivity analysis

of control parameters on maximum power seeking is presented. Finally, the proposed technique is compared to a conventional technique.

A novel vibration mitigation technique based on the nonlinear sliding mode theory is presented in Chapter 5. Prior to developing this technique, a background on the sliding mode theory is provided, and natural frequencies of the 750kW five-mass drivetrain are calculated. The developed method of torsional vibrations was tested on 750kW DFIG-based and PMG-based wind turbines, and results are compared to the results from virtual inertia technique.

A summary of key research outcomes and contributions along with suggestions for future work are presented for extremum power seeking and the mitigation of torsional vibration topics in variable speed wind turbines in Chapter 6.

Chapter 2 – Wind Turbine Classification and Aerodynamics

Various wind turbine classifications are expressed in Section 2.1 of this chapter. In Section 2.2, operating regions and aerodynamics of wind turbines are presented to explain the nonlinear behavior of wind turbines as wind speed varies. A brief explanation on the wind turbine aerodynamic simulator used in this work, FAST, is given in Section 2.3. The drivetrain is modeled for mechanical resonance (vibration) studies in Section 2.4.

2.1 Wind Turbine Classification

Wind turbine systems can be classified based on type of generator, rotor axis, control scheme, and ecological location. In Figure 2.1, two type of rotor axes, around which the turbine blades rotate, are shown. Most wind turbines are classified as horizontal axis, some wind turbines have blades that spin around a vertical axis [38]. Furthermore, the number of blades can differ in wind turbines, but most current wind turbines have three blades. The major components of wind turbines are blades, a rotor hub, drivetrain (bearing and gears), a generator, power converters and control systems. Wind turbine systems can be classified in terms of their connections to a local load (i.e. stand-alone applications, a utility power grid, i.e. grid-connected). In stand-alone applications, a wind turbine feeds one or several electric loads such as water pumping, communication stations, and light towers, that are isolated from the utility grid. In these applications, power captured by the wind turbine should be equal to the demand power (load). In grid-connected applications, a number of wind turbines typically form a wind farm and ideally run at the maximum power-seeking mode of operation. Most of wind turbine systems are designed as variable speed turbines to produce

Figure 2.1 Horizontal (right) and vertical (left) axis wind turbine structures [56].

more energy than fixed speed ones by using power electronic converters. Wind turbines can also be classified in terms of location as on-shore and off-shore turbines.

There are some limitations for the onshore application. Offshore wind turbines typically face higher wind speeds and, therefore, the amount of mechanical stress is higher. Due to limited accessibility and transportation difficulties, high water erosion, and high wind speeds, capital and maintenance costs for offshore wind turbines are also higher than onshore wind turbines.

The fixed speed, squirrel-cage induction generator operates at a speed slightly higher than the synchronous speed, $n_{syn} = \frac{120}{p} f_{grid}$ (rpm), where p is the number of poles and f_{grid} is the frequency of the power grid. Therefore, a high number of poles and/or a gearbox is required since the blades shaft speed is very low (e.g. as low as $7 - 12$ rpm for a 5MW wind turbine). Also, induction generators cannot produce any reactive power but they need reactive power to build the necessary internal magnetic field for the energy conversion process. Thus, reactive power compensation is implemented by capacitor banks at the generator terminals [39], as shown in Figure 2.2.

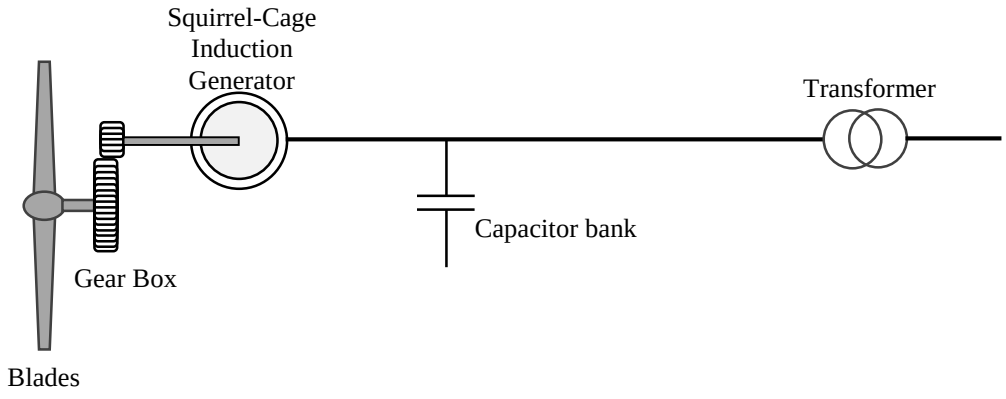

Figure 2.2 Fixed speed wind turbine topology

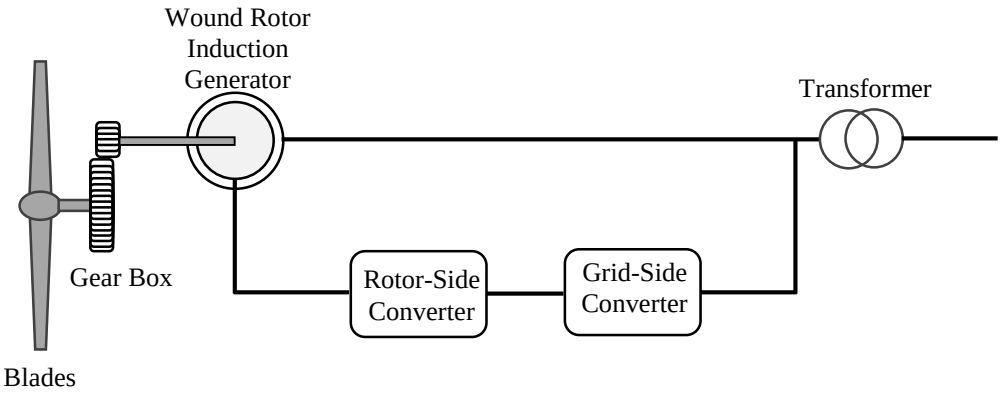

Figure 2.3 Variable speed DFIG-based wind turbine topology

A majority of wind turbines are variable speed in which, the developed torque of the generator is controlled by the generator-side converter, while the grid-side converter keeps the DC-bus voltage balanced by transferring input power to the grid. Variable speed wind turbines use either a (DFIG) or (PMG). In the DFIG-based wind turbine, approximately 30% of generated power transfers through the rotor circuit and a back-to-back converter and the rest of the generated power is directly injected into the grid through stator windings [40], [41], [42]. Therefore, a multi-stage gearbox is needed to provide the match between rotor speed and frequency of the voltage at the stator terminal for a chosen number of poles . In PMG-based wind turbine, 100% of generated power transfers through the stator terminal and a back-to-back converter [43]. In this case, a multi-stage gearbox is not essential when a high number of poles may be required.

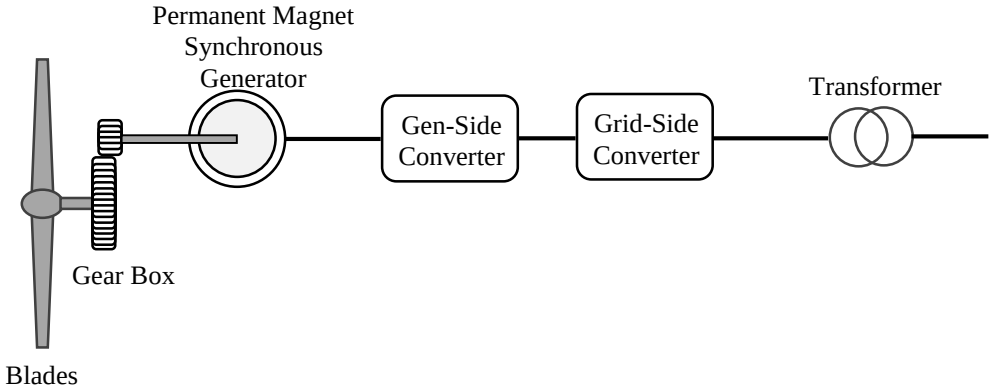

Figure 2.4 Variable speed PMG-based wind turbine topology

2.2 Wind Turbine Aerodynamics

There are different notations to specify various operational regions of wind turbines. Herein, operational regions are defined as Regions 1, 2, 2.5, 3, and 4, as shown in Figure 2.5. In Region 2, wind turbines start to produce power when the wind speed is above v_{min}, and the generated power can go up to the rated power of the overall wind turbine system, $P_{T\ rated}$. In this region, the wind turbine operates at a variable speed mode to capture maximum available power from the wind. In Region 3, the wind speed is above $v_{PT\ rated}$, at which the captured power is at its rated or nominal value, and the maximum wind speed, v_{max}. In this region, wind turbines operate at the rated power and the rated rotor speed by controlling the blades pitch angle. In Region 2.5, wind turbines operate around the rated rotor speed but below the rated power.

Power captured is performed only in Region 2, due to the inherent variable nature of the wind speed and therefore irregular available wind power. Again, in Region 1, the wind speed is below a minimum level for turbine operation and thus no power can be captured. In Region 2, rotor speed can be controlled to capture maximum power as the wind speed varies, with the blade pitch angle typically held constant at the optimal value providing maximum aerodynamic torque. In Region 3, the wind speed is above a maximum rated speed where no extremum power seeking

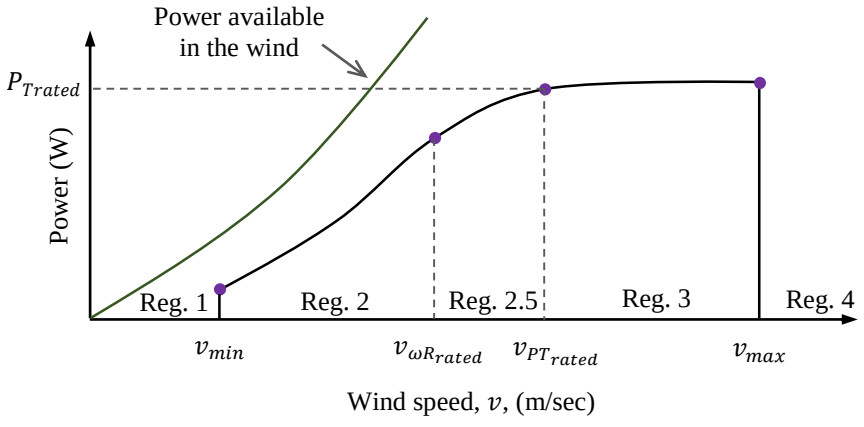

Figure 2.5 Different operational regions of wind turbine

is required so the goal is to use blade pitch control to control the generator speed at its rated value by reducing extra aerodynamic power. Control in Region 2 is a complicated because of nonlinear dynamics and immeasurable terms such as rotor aerodynamic torque and the power capture coefficient. Figure 2.5 shows the power captured by a turbine versus wind speed relationship for three wind speeds. The relationship between mechanical input power and wind speed normal to the turbine blades can be written in terms of available wind power, P_{avail}, as

$$P_{avail} = \frac{1}{2}\,\rho\, A\, v^3 \tag{2.2.1}$$

where ρ is the air density (1.225 kg/m^3), A is the rotor swept area, and v is the wind speed. The power captured by the turbine, P_T, is a fraction of the available power expressed as

$$P_T = P_{avail}.\, C_p(\lambda, \beta) \tag{2.2.2}$$

where $C_p(\lambda, \beta)$ is the power capture coefficient, β is the blade pitch angle in rad, and λ is the dimensionless tip speed ratio given by

$$\lambda = \frac{\omega_R R}{v} \tag{2.2.3}$$

where ω_R is the rotor speed in rad/sec, and R is the blade radius in meters. According to the Betz law [44], the power coefficient of a wind turbine is limited to $\frac{16}{27} \cong 0.593$. Let T_{aero} denote aerodynamic torque delivered to the turbine rotor, then captured power is

$$P_T = T_{aero}\omega_R. \tag{2.2.4}$$

Combining (2.2.1), (2.2.2), and (2.2.4) and then solving for T_{aero} (or mechanical torque, T_m) yields

$$T_{aero} = f(v, \omega_R) C_p(\lambda, \beta) \tag{2.2.5}$$

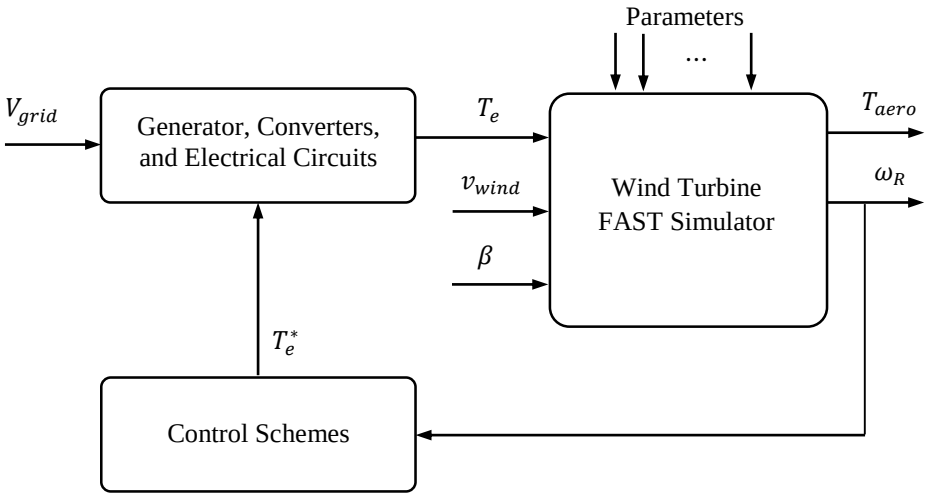

Figure 2.6 Block diagram of interfacing of FAST and electrical parts and controllers in the Matlab/Simulink

where $f = (1/2\omega_R)\rho A v^3$ for $\omega_R > 0$. Using the tip speed ratio of (2.2.3), T_{aero} is proportional to the square of the rotor speed. In addition to wind turbine aerodynamic equations, the equation of motion for a coupled wind turbine and generator, referred to the rotor shaft, is

$$J\frac{d\omega_R}{dt} = T_{aero} - T_e \tag{2.2.6}$$

where J is the equivalent lumped mass moment of inertia of the blades, rotor shaft, and drivetrain, and T_e is the electrical torque provided by the generator.

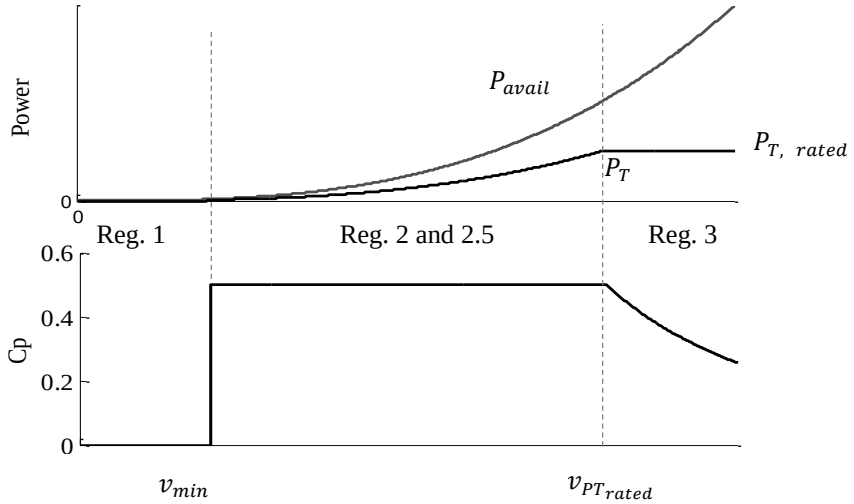

Figure 2.7 Ideal power capture coefficient,C_P, of a wind turbine in Regions 1, 2, 2.5 and 3.

2.3 FAST Tool for Modeling Wind Turbine Aerodynamics

The mechanical subsystem is modeled using the FAST (Fatigue, Aerodynamics, Structures, and Turbulence) simulator, which has been developed by the National Renewal Energy Laboratory (NREL). This wind turbine (mechanical parts) has been used as the analysis tool to examine the validity of numerous control schemes applied to wind turbines in the literature [45], [30], [31].

The FAST simulator includes the aerodynamics and mechanical aspects of a wind turbine. FAST reads mechanical and aerodynamic system parameters from input files and creates mechanical output files to exchange with the Simulink model. In this work, the key inputs to FAST are the wind speed profile and electrical torque, and the main outputs are mechanical (aerodynamic) torque, T_{aero}, and low-speed rotor speed, ω_R. In this dissertation, electrical parts and controllers, implemented by Simulink blocks, are coupled to the inputs and outputs of the FAST simulator, as shown in Figure 2.7.

2.3.1 *FAST Simulator Capabilities*

The FAST simulator enables analysis of nonlinear aerodynamics of tower, two-mass drivetrain, two- or three-blade, horizontal-axis rotor, and off-shore and on-shore (on-land) wind turbines. FAST, which is written in the Fortran programming language, can be used in a Simulink model as an S-Function block. Many parameters of a wind turbines are accessible and can be set prior to running the FAST simulator. Although a Thevenin's equivalent induction generator model exists in the FAST simulator, it is not as sophisticated as the model developed in this dissertation.

2.3.2 *FAST Simulator Models in this Dissertation*

Two different FAST models are used in this dissertation: a 5 MW and a 750 kW wind turbine model. The 5 MW model is used for the extremum power seeking study and the 750 kW model is used for the vibration mitigation study in this work justification. The following paragraphs provide, a short summary of the FAST models for each system.

The 5 MW system in this dissertation is built around the NREL 5 MW FAST model. In the turbine model the distance from the rotor apex to the blade tip is 63 m, the distance from the rotor apex to the blade root is 1.5 m, the height of tower above ground level is 87.6 m, the vertical distance from the top of the tower to the rotor shaft is 1.96 m, the rotor inertia is 38.759227 kg-m^2. Details of the model can be found in [31]. The turbine has a nominal shaft speed of 12.1 RPM at 11.4 m/s wind speed identifying the upper boundary of Region 2 for the 5 MW wind turbine.

The 750 kW system in this dissertation is built around the NREL 750 kW FAST model . In the turbine model the distance from the rotor apex to the blade tip is 24.1 m, the distance from the rotor apex to the blade root is 0.6 m, the height of the tower above ground level is 53.6 m, the vertical distance from the top of the tower to the rotor shaft is 1.2 m, the rotor inertia is 998138 kg-m^2, etc. Details on the model can be found in [46]. The turbine has a nominal shaft speed of 24 RPM at 11.4 m/s wind speed identifying the upper boundary of Region 2 for the 750 MW wind turbine.

2.4 **Modeling of Multi-Mass Drivetrain (Gearbox) System**

The drivetrain dynamic includes the rotor, the gearbox and the generator. For most studies, the wind turbine drivetrain has been modeled as a two-mass system coupled through a gearbox, thereby justifying neglect of the effects of the gearbox moment of inertia, damping, and stiffness [30], [47]. However, in a study of torsional vibration (resonance), a detailed model of a gearbox

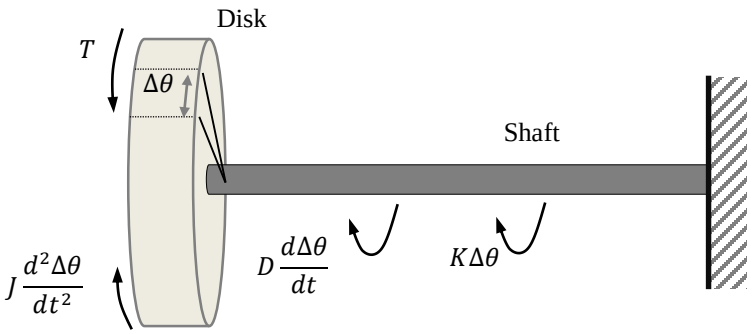

Figure 2.8 Torsional dynamic in a rotating system

must be considered [24], [30], [46] . A simple model for a rotational system is shown in Figure 2.8. As shown, the imposed torque, T, is balanced at any instant by the summation of torques generated by disk inertia, damping, and stiffness of the shaft as

$$T = J\frac{d^2\Delta\theta}{dt^2} + D\frac{d\Delta\theta}{dt} + K\Delta\theta \tag{2.4.1}$$

where $\Delta\theta$ is the angular displacement due to the imposed torque.

A five-mass model of the drivetrain is considered in this work, as shown in Figure 2.9. Thus, the equations of motion for the wind turbine coupled to the generator can be represented by a five-mass-spring-damper model with a three-mass gearbox and four torsional springs. In total, this five-degree-of-freedom model has five natural frequencies. A five-mass drivetrain can be described by the following differential equations [30], [24]:

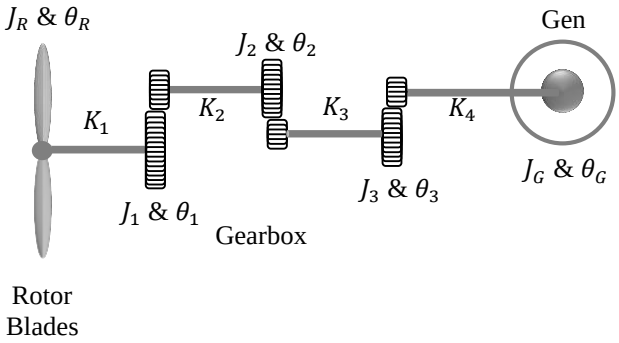

Figure 2.9 Five-mass drivetrain system

$$J_R \frac{d\omega_R}{dt} = T_{aero} - K_1(\theta_R - \theta_1) - D_1\,(\omega_R - \omega_1) \tag{2.4.2}$$

$$J_1 \frac{d\omega_1}{dt} = K_1(\theta_R - \theta_1) + D_1\,(\omega_R - \omega_1) - K_2(\theta_1 - \theta_2) - D_2\,(\omega_1 - \omega_2) \tag{2.4.3}$$

$$J_2 \frac{d\omega_2}{dt} = K_2(\theta_1 - \theta_2) + D_2\,(\omega_1 - \omega_2) - K_3(\theta_2 - \theta_3) - D_3\,(\omega_2 - \omega_3) \tag{2.4.4}$$

$$J_3 \frac{d\omega_3}{dt} = K_3(\theta_2 - \theta_3) + D_3\,(\omega_2 - \omega_3) - K_4(\theta_3 - \theta_G) - D_4\,(\omega_3 - \omega_G) \tag{2.4.5}$$

$$J_G \frac{d\omega_G}{dt} = K_4(\theta_3 - \theta_G) + D_4\,(\omega_3 - \omega_G) - T_e \tag{2.4.6}$$

where J represents the lumped moments of inertia for each mass, K represents the stiffness value of each shaft, and D represents the viscous damping coefficient. Since θ and ω are considered state variables, the order of a five-mass drivetrain (gearbox) system is described by 10 first-order differential equations. Herein, (2.4.2) through (2.4.6) only represent five of these equations, while the other five are given by simple differential equations: $\frac{d\theta_R}{dt} = \omega_R$, $\frac{d\theta_1}{dt} = \omega_1$, $\frac{d\theta_2}{dt} = \omega_2$, $\frac{d\theta_3}{dt} = \omega_3$, and $\frac{d\theta_G}{dt} = \omega_G$ .These equations can be formed in a 10×10 matrix format as

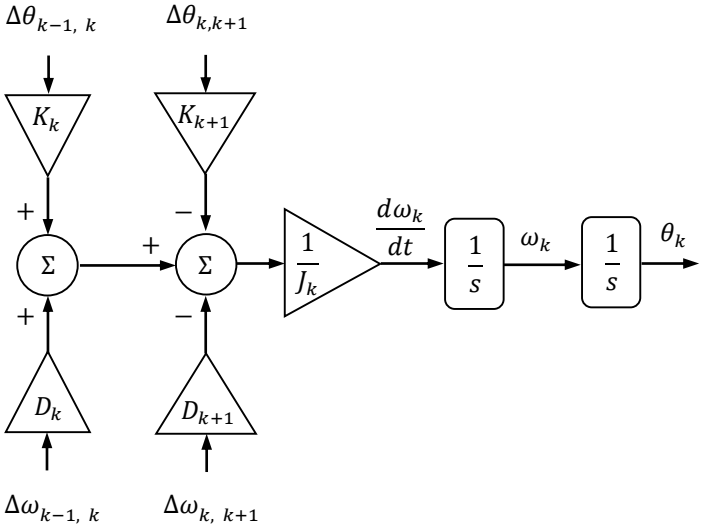

Figure 2.10 Gearbox stage model of a multi-mass drivetrain in a block diagram format

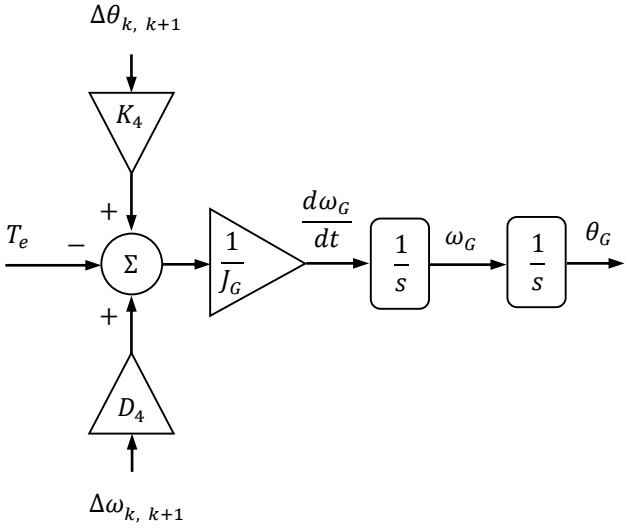

Figure 2.11 Generator dynamics as a part of the multi-mass drivetrain

$$\frac{d}{dt}\begin{bmatrix}[\theta]_{5\times1}\\ [J]_{5\times1}\ \ [\omega]_{5\times1}\end{bmatrix}=\begin{bmatrix}[0]_{5\times5} & [I]_{5\times5}\\ [K]_{5\times5} & [D]_{5\times5}\end{bmatrix}\begin{bmatrix}[\theta]_{5\times1}\\ [\omega]_{5\times1}\end{bmatrix}+\begin{bmatrix}[0]_{5\times1}\\ [T]_{5\times1}\end{bmatrix} \tag{2.4.7}$$

which can be rewritten as

$$\frac{d}{dt}\begin{bmatrix}[\theta]_{5\times1}\\ [\omega]_{5\times1}\end{bmatrix}=\begin{bmatrix}[0]_{5\times5} & [I]_{5\times5}\\ [J]^{-1}_{5\times5}[K]_{5\times5} & [J]^{-1}_{5\times5}[D]_{5\times5}\end{bmatrix}\begin{bmatrix}[\theta]_{5\times1}\\ [\omega]_{5\times1}\end{bmatrix}+\begin{bmatrix}[0]_{5\times1}\\ [J]^{-1}_{5\times5}[T]_{5\times1}\end{bmatrix} \tag{2.4.8}$$

where, $[\theta]=[\theta_R\quad\theta_1\quad\theta_2\quad\theta_3\quad\theta_G]^T$, $[\omega]=[\omega_R\quad\omega_1\quad\omega_2\quad\omega_3\quad\omega_G]^T$, $[T]=[T_{earo}\quad 0\quad 0\quad 0\quad T_e]^T$, and stiffness and damping metrics (i.e., $[K]$ and $[D]$) are given as

$$[K]=\begin{bmatrix}-K_1 & K_1 & 0 & 0 & 0\\ K_1 & -(K_1+K_2) & K_2 & 0 & 0\\ 0 & K_2 & -(K_2+K_3) & K_3 & 0\\ 0 & 0 & K_3 & -(K_3+K_4) & K_4\\ 0 & 0 & 0 & K_4 & -K_4\end{bmatrix} \tag{2.4.9}$$

$$[D]=\begin{bmatrix}-D_1 & D_1 & 0 & 0 & 0\\ D_1 & -(D_1+D_2) & D_2 & 0 & 0\\ 0 & D_2 & -(D_2+D_3) & D_3 & 0\\ 0 & 0 & D_3 & -(D_3+D_4) & D_4\\ 0 & 0 & 0 & D_4 & -D_4\end{bmatrix} \tag{2.4.10}$$

Also, $[J]_{5\times5}^{-1}$ is given as

$$[J]^{-1} = \begin{bmatrix} J_R^{-1} & 0 & 0 & 0 & 0 \\ 0 & J_1^{-1} & 0 & 0 & 0 \\ 0 & 0 & J_2^{-1} & 0 & 0 \\ 0 & 0 & 0 & J_3^{-1} & 0 \\ 0 & 0 & 0 & 0 & J_G^{-1} \end{bmatrix} \tag{2.4.11}$$

One gearbox stage of a multi-mass drivetrain is shown in Figure 2.10 in a block diagram format Figure 2.11 shows generator dynamics as a part of the drivetrain.

2.4.1 *Multi-Mass Drivetrain Natural Frequencies*

Eigenvalues of the drivetrain can be calculated by solving the following equation

$$det\begin{bmatrix} \lambda[I]_{5\times5} & -[I]_{5\times5} \\ -[J]_{5\times5}^{-1}[K]_{5\times5} & \lambda[I]_{5\times5} - [J]_{5\times5}^{-1}[D]_{5\times5} \end{bmatrix} = 0 \tag{2.4.12}$$

Remark: If A, B, M, and N are $n \times n$ matrices and N is invertible, then the determinate of the blocking matrix $\begin{bmatrix} A & B \\ M & N \end{bmatrix}$ is calculated as

$$det\begin{bmatrix} A & B \\ M & N \end{bmatrix} = \det(AN - BN^{-1}MN) \tag{2.4.13}$$

Using this remark, for the worst case scenario when the damping coefficient matrix is neglected, (i.e. $[D]_{5\times5} = [0]_{5\times5}$), natural frequencies of the five-mass drivetrain are given by

$$\det(\lambda^2\ [I]_{5\times5} - [I]_{5\times5}\ \lambda^{-1}\ [I]_{5\times5}\ [J]_{5\times5}^{-1}[K]_{5\times5}\ \lambda[I]_{5\times5}) = 0 \tag{2.4.14}$$

which can be simplified as

$$\det(\lambda^2\ [I]_{5\times5} -\ [J]_{5\times5}^{-1}\ [K]_{5\times5}\ ) = 0 \tag{2.4.15}$$

The natural frequencies are calculated as

$$f = \frac{1}{2\pi}\sqrt{eig([J]_{5\times5}^{-1}\ [K]_{5\times5})}. \tag{2.4.16}$$

This equation can be used to generate compensation torque components at the natural frequencies of the drivetrain in order to develop an active torsional vibration (resonance) mitigation method, as discussed in Chapter 5.

2.4.2 *Integration of Multi-Mass Model into the FAST Model*

Development of the FAST simulator was based only on a two-mass model of the drivetrain [32]. Therefore, a multi-mass model of the drivetrain (gearbox) should be separately developed and coupled to the FAST simulator, as shown in Figure 2.12. As observed from a comparison of Equations (2.2.6) and (2.4.2), dynamics of the rotor low-speed shaft is modeled by the FAST code, where generator torque, T_e, is an input signal to the FAST simulator, as shown in Figure 2.8. Accordingly, the last two terms in Equation (2.4.2) can be defined as T_{e_React} as the input signal to the FAST simulator, while Equations (2.4.3) through (2.4.6) must be constructed in the Matlab/Simulink environment, as shown in Figure 2.12. These equations are also demonstrated in block diagram formats shown in Figures 2.10 and 2.11.

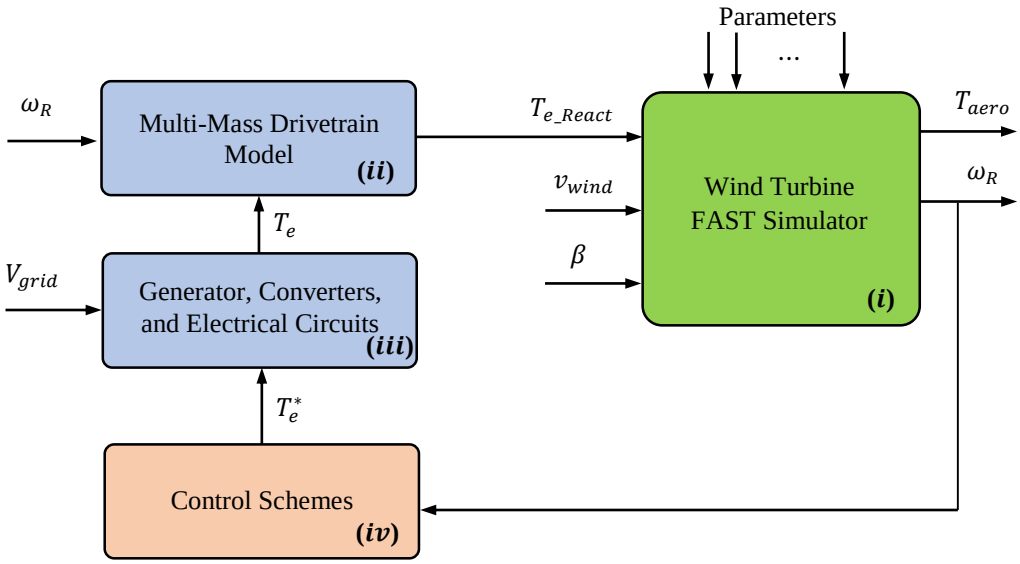

Figure 2.12 Block diagram of interfacing of different subsystems and controllers in the Matlab/Simulink, (i) is developed by others and adapted in this work, (ii) & (iii) developed based on existing knowledge, (iv) original contribution of this dissertation explained in Chapters 4 and 5.

Chapter 3 – Modeling of Electrical Devices in Wind Turbines

In this chapter, all electrical parts of DFIG-based and PMG-based wind turbines are developed in the synchronously rotating $dq0$-reference frame. Developed state-space representations of the electric parts form the electric circuit blocks shown earlier in Figures 2.11 and 2.12 of Chapter 2. These state-space models are able to be easily linked to the FAST wind turbine simulator/code, enabling complicated studies to be performed on various control strategies in variable speed DFIG-based and PMG-based wind turbines in the presence of electrical and mechanical disturbances. In this chapter, full-order models of grid-connected DFIG and PMG are presented. The models of back-to-back converters and their controllers are developed in the $dq0$-reference frame. A compensated power line model is developed in order to study a series capacitor switching in the feeder line between the grid and a wind turbine system.

3.1 DFIG-based and PMG-based Wind Turbine Topologies

Energy conversion in wind energy systems is achieved using two main devices. The first device is the extraction device, which harvests mechanical power of the wind stream that turns the wind turbine rotor, as explained in Chapter 2. The other device is the generator that transforms rotational mechanical energy to electrical energy [48]. As described in Chapter 2, fixed speed wind turbines are typically operated with a squirrel cage induction generator that requires a multi-stage gearbox. However, most high-power (above 500kW) wind turbines have adopted variable speed operation because of extremum power seeking, active control capabilities in response to grid power quality requirements. For these variable speed applications, both (DFIGs) and (PMGs) are commonly used with a multi-stage gearbox and power electronic converters. PMG-based wind turbines are becoming increasingly popular because they eliminate the need for a gearbox resulting

in a lower number of required maintenances [46]. (PMG) and (DFIG) topologies are described in the following subsections.

3.2 Doubly Fed Induction Generator

DFIG currently is the most common type of generator in wind turbine systems. A DFIG consists of two sets of windings on the stator and rotor. Both stator and rotor have three windings that correspond to three phases: phase-a, phase-b, and phase-c. The stator has p number of poles. Stator phases are directly connected to the power grid, whereas the rotor phases (terminals) are connected to the power grid through two back-to-back converters, as shown in Figure 3.1. The back-to-back converter handles only the rotor power rating, which is approximately 30% of the nominal generator power. Therefore, less power loss occurs in the converter of a DFIG compared to that in a PMG where the converter handles the entire captured power [43].

3.2.1 *Normal abc- and $dq0$-Reference Frames*

A three-phase power apparatus or system is generally modeled in a normal abc-reference frame, single-line representation, or $dq0$ (direct-quadrature-zero)-reference frame. For control purposes, control engineers commonly use $dq0$-reference frame models of generators, converters,

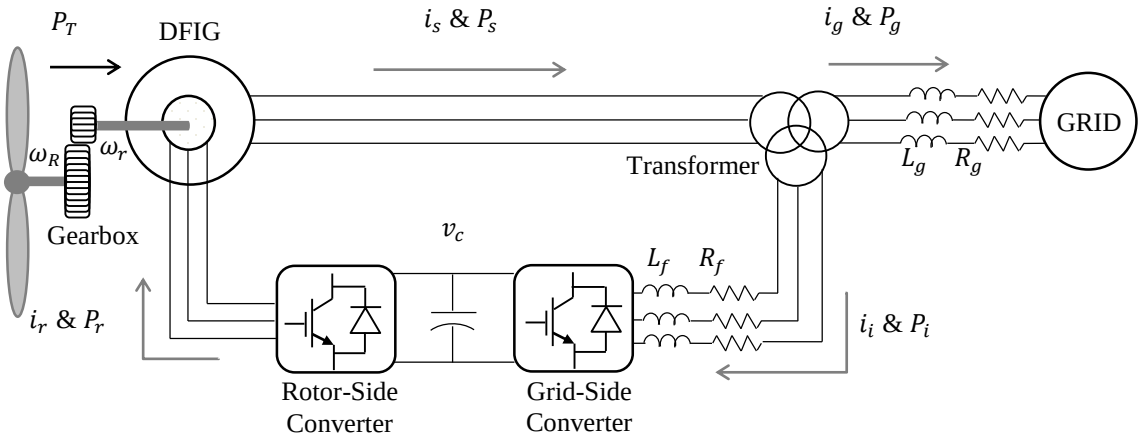

Figure 3.1 Schematic of a DFIG based wind turbine system

filters, and power lines. A $dq0$ model is obtained using a mathematical transformation that rotates in a constant speed in a reference frame that simplifies analysis of three-phase circuits or systems. The $dq0$ formulation presented in this dissertation is identical to the one first proposed by Robert H. Park in 1927, and similar formulations also called $dq0$- transformation exist in the literature. The main advantage of using dqo transformation is that the three AC quantities are reduced to two DC quantities in balanced three-phase systems. Furthermore, in the analysis of three-phase electric machines, this transformation eliminates the effect of time varying inductances. In Figure 3.2, magnetic axes of a three-phase induction machine (generator), are demonstrated in conjunction with corresponding q and d axes. The $dq0$ (or Park's) transformation matrix, T, used in this dissertation to convert abc quantities to $dq0$ reference-frame quantities are given as

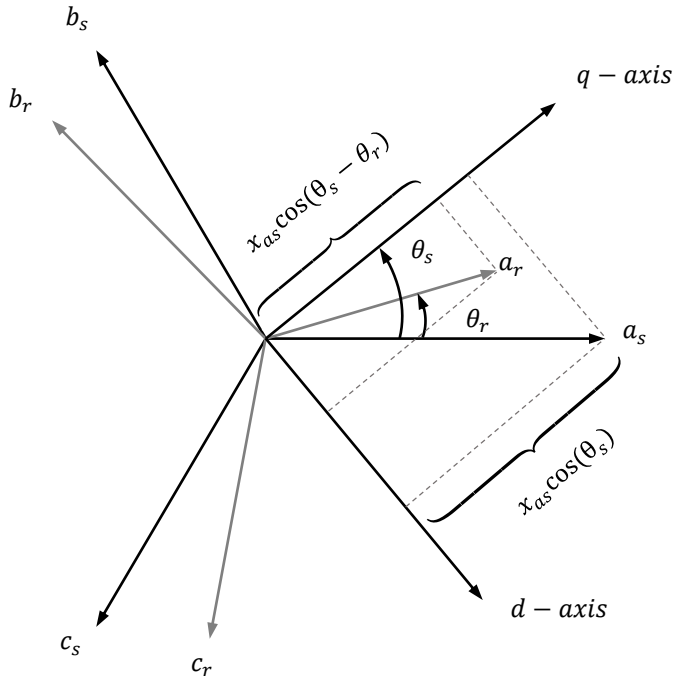

Figure 3.2 Stator and rotor magnetic axes of a three-phase induction machine

$$\begin{bmatrix} x_q \\ x_d \\ x_0 \end{bmatrix} = \frac{2}{3}\begin{bmatrix} \cos(\theta_s) & \cos\left(\theta_s - \frac{2\pi}{3}\right) & \cos\left(\theta_s + \frac{2\pi}{3}\right) \\ \sin(\theta_s) & \sin\left(\theta_s - \frac{2\pi}{3}\right) & \sin\left(\theta_s + \frac{2\pi}{3}\right) \\ \frac{1}{2} & \frac{1}{2} & \frac{1}{2} \end{bmatrix}\begin{bmatrix} x_a \\ x_b \\ x_c \end{bmatrix} \tag{3.2.1}$$

where x can be v, i, or λ. θ_s is the angle between stator phase-a and q-axis. Also, the $2/3$ is an arbitrary coefficient, as for example $\sqrt{2/3}$ is also used by many investigators. The transformation from $dq0$ to abc is obtained from

$$\begin{bmatrix} x_a \\ x_b \\ x_c \end{bmatrix} = \begin{bmatrix} \cos(\theta_s) & \sin(\theta_s) & 1 \\ \cos\left(\theta_s - \frac{2\pi}{3}\right) & \sin\left(\theta_s - \frac{2\pi}{3}\right) & 1 \\ \cos\left(\theta_s + \frac{2\pi}{3}\right) & \sin\left(\theta_s + \frac{2\pi}{3}\right) & 1 \end{bmatrix}\begin{bmatrix} x_q \\ x_d \\ x_0 \end{bmatrix}. \tag{3.2.2}$$

Here after, $T_{\theta s}$, is called the abc to dqo and $T_{\theta s}^{-1}$ is called $dq0$ to abc transformation matrices.

3.2.2 *DFIG Model in abc-Reference Frame.*

Modeling of DFIG begins by applying the Kirchhoff 's Voltage Law (KVL) for stator windings to get

$$\begin{bmatrix} v_{as} \\ v_{bs} \\ v_{cs} \end{bmatrix} = -\begin{bmatrix} R_s & 0 & 0 \\ 0 & R_s & 0 \\ 0 & 0 & R_s \end{bmatrix}\begin{bmatrix} i_{as} \\ i_{bs} \\ i_{cs} \end{bmatrix} + \frac{d}{dt}\begin{bmatrix} \lambda_{as} \\ \lambda_{bs} \\ \lambda_{cs} \end{bmatrix} \tag{3.2.3}$$

where R_s is the resistance value of stator windings in each phase, and the stator linkage flux, λ_s or λ_{abc}^s, includes both the stator and rotor effects (i.e., $\lambda_{abc}^s = \lambda_{abc}^{ss} + \lambda_{abc}^{sr}$). Similarly, rotor winding equations are written as

$$\begin{bmatrix} v_{ar} \\ v_{br} \\ v_{cr} \end{bmatrix} = \begin{bmatrix} R_r & 0 & 0 \\ 0 & R_r & 0 \\ 0 & 0 & R_r \end{bmatrix}\begin{bmatrix} i_{ar} \\ i_{br} \\ i_{cr} \end{bmatrix} + \frac{d}{dt}\begin{bmatrix} \lambda_{ar} \\ \lambda_{br} \\ \lambda_{cr} \end{bmatrix} \tag{3.2.4}$$

where R_r is the resistance value of stator windings in each phase, and the rotor linkage flux includes the rotor and stator effects (i.e., $\lambda_{abc}^r = \lambda_{abc}^{rr} + \lambda_{abc}^{rs}$). Also, the rotor quantities are

referred to the stator side (i.e., $v_{ar} = (n_s/n_r)v_{ar(actual)}$, $R_r = (n_s/n_r)^2 R_{r(actual)}$, $i_{ar} = (n_r/n_s)i_{ar(actual)}$, $\lambda_{ar} = (n_s/n_r)\lambda_{ar(actual)}$), where n_s and n_r are the number of turns per phase in the stator and rotor windings, respectively. This simplifies the rotor and stator equations, as L_m can represent the stator magnetizing inductance, the stator-rotor mutual inductance, and the rotor magnetizing inductance all referred to the stator side. More details on electromagnetic circuits of electric machines are presented in [29].

As mentioned, the stator linkage flux is given as a summation of the stator and rotor magnetic fluxes (i.e., $\lambda^s_{abc} = \lambda^{ss}_{abc} + \lambda^{sr}_{abc}$). This can be written in a matrix format as

$$\begin{bmatrix}\lambda_{as}\\ \lambda_{bs}\\ \lambda_{cs}\end{bmatrix} = -\begin{bmatrix} L_{ls}+L_m & -\frac{1}{2}L_m & -\frac{1}{2}L_m \\ -\frac{1}{2}L_m & L_{ls}+L_m & -\frac{1}{2}L_m \\ -\frac{1}{2}L_m & -\frac{1}{2}L_m & L_{ls}+L_m \end{bmatrix}\begin{bmatrix} i_{as}\\ i_{bs}\\ i_{cs}\end{bmatrix}$$
$$+\begin{bmatrix} L_m\cos(\theta_r) & L_m\cos\left(\theta_r+\frac{2\pi}{3}\right) & L_m\cos\left(\theta_r-\frac{2\pi}{3}\right) \\ L_m\cos\left(\theta_r-\frac{2\pi}{3}\right) & L_m\cos(\theta_r) & L_m\cos\left(\theta_r+\frac{2\pi}{3}\right) \\ L_m\cos\left(\theta_r+\frac{2\pi}{3}\right) & L_m\cos\left(\theta_r-\frac{2\pi}{3}\right) & L_m\cos(\theta_r) \end{bmatrix}\begin{bmatrix} i_{ar}\\ i_{br}\\ i_{cr}\end{bmatrix} \qquad (3.2.5)$$

Similarly, the rotor flux linkages are obtained from

$$\begin{bmatrix}\lambda_{ar}\\ \lambda_{br}\\ \lambda_{cr}\end{bmatrix} = \begin{bmatrix} L_{lr}+L_m & -\frac{1}{2}L_m & -\frac{1}{2}L_m \\ -\frac{1}{2}L_m & L_{lr}+L_m & -\frac{1}{2}L_m \\ -\frac{1}{2}L_m & -\frac{1}{2}L_m & L_{lr}+L_m \end{bmatrix}\begin{bmatrix} i_{ar}\\ i_{br}\\ i_{cr}\end{bmatrix}$$
$$-\begin{bmatrix} L_m\cos(\theta_r) & L_m\cos\left(\theta_r-\frac{2\pi}{3}\right) & L_m\cos\left(\theta_r+\frac{2\pi}{3}\right) \\ L_m\cos\left(\theta_r+\frac{2\pi}{3}\right) & L_m\cos(\theta_r) & L_m\cos\left(\theta_r-\frac{2\pi}{3}\right) \\ L_m\cos\left(\theta_r-\frac{2\pi}{3}\right) & L_m\cos\left(\theta_r+\frac{2\pi}{3}\right) & L_m\cos(\theta_r) \end{bmatrix}\begin{bmatrix} i_{as}\\ i_{bs}\\ i_{cs}\end{bmatrix} \qquad (3.2.6)$$

If the stator and rotor variables are transformed into a rotating reference frame, the stator-rotor mutual inductances become independent of the electrical rotor position, θ_r, and rotor speed, ω_r. However, θ_r and ω_r are related to the generator mechanical angle and speed at the high-speed shaft side of wind turbines described in Chapter 2 as

$$\theta_G = \frac{2}{p}\theta_r \tag{3.2.7}$$

$$\omega_G = \frac{2}{p}\omega_r \tag{3.2.8}$$

where p is the number of poles.

3.2.3 *DFIG Model in $dq0$-Reference Frame*

Appling the $dq0$ transformation matrix, T_{θ_s}, for voltage equations of the stator windings given in (3.2.3), yields

$$\begin{bmatrix} v_{qs} \\ v_{ds} \\ v_{0s} \end{bmatrix} = -T_{\theta_s}\begin{bmatrix} R_s & 0 & 0 \\ 0 & R_s & 0 \\ 0 & 0 & R_s \end{bmatrix} T_{\theta_s}^{-1}\begin{bmatrix} i_{qs} \\ i_{ds} \\ i_{0s} \end{bmatrix} + T_{\theta_s}\,\frac{d}{dt}\left\{ T_{\theta_s}^{-1}\begin{bmatrix} \lambda_{qs} \\ \lambda_{ds} \\ \lambda_{0s} \end{bmatrix}\right\} \tag{3.2.9}$$

where T_{θ_s} and $T_{\theta_s}^{-1}$ matrices were given in (3.2.1) and (3.2.2). This equation can be rewritten as

$$\begin{bmatrix} v_{qs} \\ v_{ds} \\ v_{0s} \end{bmatrix} = -T_{\theta_s}\begin{bmatrix} R_s & 0 & 0 \\ 0 & R_s & 0 \\ 0 & 0 & R_s \end{bmatrix} T_{\theta_s}^{-1}\begin{bmatrix} i_{qs} \\ i_{ds} \\ i_{0s} \end{bmatrix} + T_{\theta_s}\,\frac{dT_{\theta_s}^{-1}}{dt}\begin{bmatrix} \lambda_{qs} \\ \lambda_{ds} \\ \lambda_{0s} \end{bmatrix} + T_{\theta_s}\,T_{\theta_s}^{-1}\frac{d}{dt}\begin{bmatrix} \lambda_{qs} \\ \lambda_{ds} \\ \lambda_{0s} \end{bmatrix}. \tag{3.2.9}$$

Also, $\frac{d}{dt}T_{\theta_s}^{-1}$ can be obtained from

$$\frac{d}{dt}T_{\theta_s}^{-1} = (\omega_s)\begin{bmatrix} -\sin(\theta_s) & \cos(\theta_s) & 0 \\ -\sin\left(\theta_s - \frac{2\pi}{3}\right) & \cos\left(\theta_s - \frac{2\pi}{3}\right) & 0 \\ -\sin\left(\theta_s + \frac{2\pi}{3}\right) & \cos\left(\theta_s + \frac{2\pi}{3}\right) & 0 \end{bmatrix} \tag{3.2.10}$$

where $\omega_s = \frac{d\theta_s}{dt}$. Substituting (3.2.10) into (3.2.9) gives

$$\begin{bmatrix} v_{qs} \\ v_{ds} \\ v_{0s} \end{bmatrix} = -\begin{bmatrix} R_s & 0 & 0 \\ 0 & R_s & 0 \\ 0 & 0 & R_s \end{bmatrix}\begin{bmatrix} i_{qs} \\ i_{ds} \\ i_{0s} \end{bmatrix} + \frac{d}{dt}\begin{bmatrix} \lambda_{qs} \\ \lambda_{ds} \\ \lambda_{0s} \end{bmatrix} + \frac{2}{3}\begin{bmatrix} cos(\theta_s) & cos\left(\theta_s - \frac{2\pi}{3}\right) & cos\left(\theta_s + \frac{2\pi}{3}\right) \\ sin(\theta_s) & sin\left(\theta_s - \frac{2\pi}{3}\right) & sin\left(\theta_s + \frac{2\pi}{3}\right) \\ \frac{1}{2} & \frac{1}{2} & \frac{1}{2} \end{bmatrix}$$

$$\times \ (\omega_s)\begin{bmatrix} -\sin(\theta_s) & \cos(\theta_s) & 0 \\ -\sin\left(\theta_s - \frac{2\pi}{3}\right) & \cos\left(\theta_s - \frac{2\pi}{3}\right) & 0 \\ -\sin\left(\theta_s + \frac{2\pi}{3}\right) & \cos\left(\theta_s + \frac{2\pi}{3}\right) & 0 \end{bmatrix}. \qquad (3.2.11)$$

Using trigonometric identities, (3.2.11) can be further simplified as

$$\begin{bmatrix} v_{qs} \\ v_{ds} \\ v_{0s} \end{bmatrix} = -\begin{bmatrix} R_s & 0 & 0 \\ 0 & R_s & 0 \\ 0 & 0 & R_s \end{bmatrix}\begin{bmatrix} i_{qs} \\ i_{ds} \\ i_{0s} \end{bmatrix} + \frac{d}{dt}\begin{bmatrix} \lambda_{qs} \\ \lambda_{ds} \\ \lambda_{0s} \end{bmatrix} + \begin{bmatrix} 0 & \omega_s & 0 \\ -\omega_s & 0 & 0 \\ 0 & 0 & 0 \end{bmatrix}. \qquad (3.2.12)$$

The same calculation steps can be performed for the rotor winding equations, that is

$$\begin{bmatrix} v_{qr} \\ v_{dr} \\ v_{0r} \end{bmatrix} = -T_{(\theta_s - \theta_r)}\begin{bmatrix} R_r & 0 & 0 \\ 0 & R_r & 0 \\ 0 & 0 & R_r \end{bmatrix} T^{-1}_{(\theta_s - \theta_r)}\begin{bmatrix} i_{qr} \\ i_{dr} \\ i_{0r} \end{bmatrix} + T_{(\theta_s - \theta_r)}\ \frac{d}{dt}\left\{ T^{-1}_{(\theta_s - \theta_r)}\begin{bmatrix} \lambda_{qr} \\ \lambda_{dr} \\ \lambda_{0r} \end{bmatrix}\right\} \qquad (3.2.13)$$

where in $dq0$ transformation for the rotor quantities, the θ_s in (3.2.1) and (3.2.2) must be replaced by $(\theta_s - \theta_r)$. This yields

$$\begin{bmatrix} v_{qr} \\ v_{dr} \\ v_{0r} \end{bmatrix} = \begin{bmatrix} R_r & 0 & 0 \\ 0 & R_r & 0 \\ 0 & 0 & R_r \end{bmatrix}\begin{bmatrix} i_{qr} \\ i_{dr} \\ i_{0r} \end{bmatrix} + \frac{d}{dt}\begin{bmatrix} \lambda_{qr} \\ \lambda_{dr} \\ \lambda_{0r} \end{bmatrix} + \begin{bmatrix} 0 & (\omega_s - \omega_r) & 0 \\ -(\omega_s - \omega_r) & 0 & 0 \\ 0 & 0 & 0 \end{bmatrix}\begin{bmatrix} \lambda_{qr} \\ \lambda_{dr} \\ \lambda_{0r} \end{bmatrix}. \qquad (3.2.14)$$

Stator and rotor flux linkage equations given in (3.2.5) and (3.2.6) can also be converted into the $dq0$ reference frame. Beginning with the stator windings, the stator linkage flux is given by $\lambda^s_{abc} = -L_{ss} i^s_{abc} + L_{sr} i^r_{abc}$. This equation is converted to the $dq0$ reference frame by replacing the abc-reference frame current and flux quantities by their equivalents in the dq0 reference

$$T^{-1}_{\theta_s}\ \lambda^s_{dq0} = -L_{ss}\ T^{-1}_{\theta_s}\ i^s_{dq0} + L_{sr}\ T^{-1}_{\theta_s - \theta_r}\ i^r_{qd0} \qquad (3.2.15)$$

which can be simplified as

$$\lambda^{s}_{dq0} = -T_{\theta_s}\, L_{ss}\, T^{-1}_{\theta_s}\, i^{s}_{dq0} + T_{\theta_s}\, L_{sr}\, T^{-1}_{\theta_s-\theta_r}\, i^{r}_{qd0} \tag{3.2.16}$$

This can be expanded as

$$\begin{bmatrix}\lambda_{qs}\\ \lambda_{ds}\\ \lambda_{0s}\end{bmatrix}$$

$$= -T_{\theta_s}\begin{bmatrix} L_{ls}+L_m & -\frac{1}{2}L_m & -\frac{1}{2}L_m \\ -\frac{1}{2}L_m & L_{ls}+L_m & -\frac{1}{2}L_m \\ -\frac{1}{2}L_m & -\frac{1}{2}L_m & L_{ls}+L_m \end{bmatrix} T^{-1}_{\theta_s}\begin{bmatrix} i_{qs}\\ i_{ds}\\ i_{0s}\end{bmatrix}$$

$$+ T_{\theta_s}\begin{bmatrix} L_m\cos(\theta_r) & L_m\cos\left(\theta_r+\frac{2\pi}{3}\right) & L_m\cos\left(\theta_r-\frac{2\pi}{3}\right) \\ L_m\cos\left(\theta_r-\frac{2\pi}{3}\right) & L_m\cos(\theta_r) & L_m\cos\left(\theta_r+\frac{2\pi}{3}\right) \\ L_m\cos\left(\theta_r+\frac{2\pi}{3}\right) & L_m\cos\left(\theta_r-\frac{2\pi}{3}\right) & L_m\cos(\theta_r) \end{bmatrix} T^{-1}_{(\theta_s-\theta_r)}\begin{bmatrix} i_{qr}\\ i_{dr}\\ i_{0r}\end{bmatrix}. \tag{3.2.17}$$

This can further simplified as

$$\begin{bmatrix}\lambda_{qs}\\ \lambda_{ds}\\ \lambda_{0s}\end{bmatrix} = -\begin{bmatrix} L_{ls}+L_M & 0 & 0 \\ 0 & L_{ls}+L_M & 0 \\ 0 & 0 & L_{ls}\end{bmatrix}\begin{bmatrix} i_{qs}\\ i_{ds}\\ i_{0s}\end{bmatrix} + \begin{bmatrix} L_M & 0 & 0 \\ 0 & L_M & 0 \\ 0 & 0 & 0\end{bmatrix}\begin{bmatrix} i_{qr}\\ i_{dr}\\ i_{0r}\end{bmatrix} \tag{3.2.18}$$

where, $L_M = \frac{3}{2}L_m$. Similarly, rotor flux linkage equations can also be converted to the $dq0$ reference frame

$$\begin{bmatrix}\lambda_{qr}\\ \lambda_{dr}\\ \lambda_{0r}\end{bmatrix}$$

$$= T_{(\theta_s-\theta_r)}\begin{bmatrix}L_{lr}+L_m & -\frac{1}{2}L_m & -\frac{1}{2}L_m\\ -\frac{1}{2}L_m & L_{lr}+L_m & -\frac{1}{2}L_m\\ -\frac{1}{2}L_m & -\frac{1}{2}L_m & L_{lr}+L_m\end{bmatrix}T^{-1}_{(\theta_s-\theta_r)}\begin{bmatrix}i_{qr}\\ i_{dr}\\ i_{0r}\end{bmatrix}$$

$$- T_{(\theta_s-\theta_r)}\begin{bmatrix}L_m\cos(\theta_r) & L_m\cos\left(\theta_r+\frac{2\pi}{3}\right) & L_m\cos\left(\theta_r-\frac{2\pi}{3}\right)\\ L_m\cos\left(\theta_r-\frac{2\pi}{3}\right) & L_m\cos(\theta_r) & L_m\cos\left(\theta_r+\frac{2\pi}{3}\right)\\ L_m\cos\left(\theta_r+\frac{2\pi}{3}\right) & L_m\cos\left(\theta_r-\frac{2\pi}{3}\right) & L_m\cos(\theta_r)\end{bmatrix}T^{-1}_{\theta_s}\begin{bmatrix}i_{qs}\\ i_{ds}\\ i_{0s}\end{bmatrix}. \quad (3.2.19)$$

This can further simplified as

$$\begin{bmatrix}\lambda_{qr}\\ \lambda_{dr}\\ \lambda_{0r}\end{bmatrix} = \begin{bmatrix}L_{lr}+L_M & 0 & 0\\ 0 & L_{lr}+L_M & 0\\ 0 & 0 & L_{lr}\end{bmatrix}\begin{bmatrix}i_{qr}\\ i_{dr}\\ i_{0r}\end{bmatrix} - \begin{bmatrix}L_M & 0 & 0\\ 0 & L_M & 0\\ 0 & 0 & 0\end{bmatrix}\begin{bmatrix}i_{qs}\\ i_{ds}\\ i_{0s}\end{bmatrix}. \quad (3.2.20)$$

3.2.4 *Block Diagram Representation of DFIG Model*

In this subsection, the block diagram representation of DFIG is presented using equations developed in the previous subsection. For balanced systems, including case studies of this dissertation, only the stator and rotor d- and q- axes equations are needed. Therefore, the electrical part of a DFIG model can be represented by four differential equations and four algebraic equations, as given in the following. Differential equations for the stator windings can be written as

$$v_{qs} = -R_s i_{qs} + \frac{d\lambda_{qs}}{dt} + \omega_s\lambda_{ds} \quad (3.2.21)$$

$$v_{ds} = -R_s i_{ds} + \frac{d\lambda_{ds}}{dt} - \omega_s\lambda_{qs} \quad (3.2.22)$$

where R_s is the stator winding resistance per phase and ω_s is the angular speed of the $dq0$-reference frame. Similarly, differential equations for the rotor windings can be written as

$$v_{qr} = R_r i_{qr} + \frac{d\lambda_{qr}}{dt} + (\omega_s - \omega_r)\lambda_{dr} \tag{3.2.23}$$

$$v_{dr} = R_r i_{dr} + \frac{d\lambda_{dr}}{dt} - (\omega_s - \omega_r)\lambda_{qr}. \tag{3.2.24}$$

Stator flux linkage equations can also be converted to the $dq0$ reference frame as

$$\lambda_{qs} = -L_s i_{qs} + L_M i_{qr} \tag{3.2.25}$$

$$\lambda_{ds} = -L_s i_{ds} + L_M i_{dr} \tag{3.2.26}$$

where L_M is the mutual-inductance and L_s is the stator self-inductance. Similarly, rotor flux linkage equations can also be expressed as

$$\lambda_{qr} = L_r i_{qr} - L_M i_{qs} \tag{3.2.27}$$

$$\lambda_{dr} = L_r i_{dr} - L_M i_{ds} \tag{3.2.28}$$

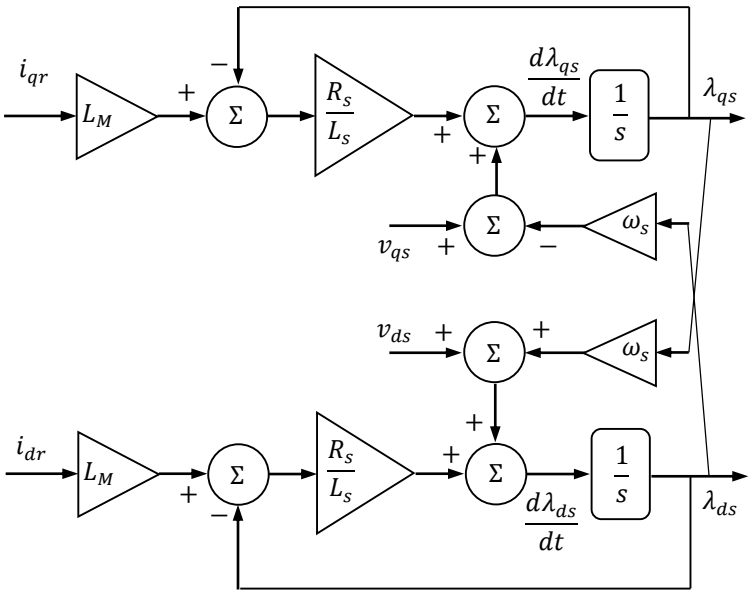

Figure 3.3 Stator flux, λ_{qs} and λ_{ds}, (state variables) calculations from the input signals, v_{qs} , i_{qr} , v_{ds} and i_{dr}

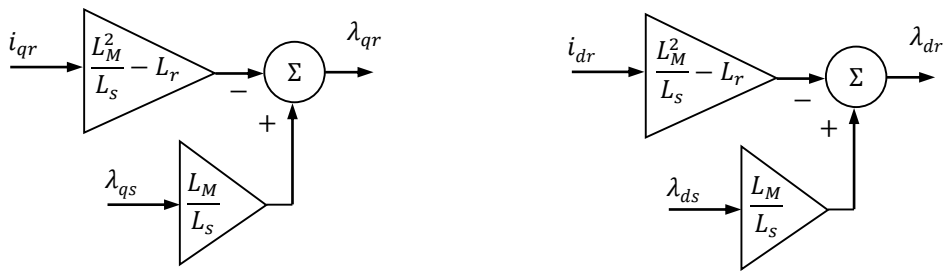

Figure 3.4 Rotor flux, λ_{qr} and λ_{dr}, (state variables) calculations from the input signals, i_{qr} and i_{dr} as well as stator flux λ_{qs} and λ_{ds}

where L_r is the rotor self-inductance. Stator voltages v_{qs} and v_{ds} are determined by the grid, and the rotor currents i_{qr} and i_{dr} are controlled by the rotor side converter, accordingly thereby obtaining λ_{qs} and λ_{ds}. Figures 3.3 and 3.4 illustrate the model of the electrical part of a DFIG in a block diagram, where L_s is equal to $L_{ls} + L_M$. Other quantities can be calculated using algebraic equations (e.g. i_{qs}, i_{ds}, from (3.2.23) and (3.2.24)) neglecting $d\lambda_{qr}/dt$ and $d\lambda_{dr}/dt$ terms. The electrical torque, T_e, formulation is developed in the following subsection.

3.2.1 *Electrical Torque of DFIG in $dq0$-Reference Frame*

In the previous subsection, the DFIG was treated as RL circuits that are magnetically coupled, and its electromechanical feature was ignored. In the following, the power transferred property of a DFIG is taken into account, beginning with stator and rotor power equations. Generated power at the stator terminals of a DFIG can be expressed as

$$P_s = v_{as}i_{as} + v_{bs}i_{bs} + v_{cs}i_{cs}. \tag{3.2.29}$$

This equation can be rewritten in a vector format as

$$P_s = {v_{abcs}}^T i_{abcs} \tag{3.2.30}$$

This can also be converted into the $dq0$ reference frame as

$$P_s = \left(T_{\theta_s}^{-1} v_{dq0}\right)^T \left(T_{\theta_s}^{-1} i_{dq0}\right) = {v_{dq0}}^T ({T_{\theta_s}^{-1}}^T T_{\theta_s}^{-1}) i_{dq0}. \tag{3.2.31}$$

where the term in parenthesis (i.e. ${T_{\theta_s}^{-1}}^T T_{\theta_s}^{-1}$) is given as

$$ {T_{\theta_s}^{-1}}^T T_{\theta_s}^{-1} = \frac{3}{2}\begin{bmatrix} 1 & 0 & 0 \\ 0 & 1 & 0 \\ 0 & 0 & 2 \end{bmatrix} \tag{3.2.32} $$

Again, for a balanced system, the 0-quantities can be neglected, and therefore (3.2.31) can be simply written as

$$ P_s = \frac{3}{2}\left(v_{qs} i_{qs} + v_{ds} i_{ds}\right). \tag{3.2.33} $$

Similarly, the rotor power, P_r, at the rotor terminal can be obtained from the following equation.

$$ P_r = \frac{3}{2}\left(v_{qr} i_{qr} + v_{dr} i_{dr}\right). \tag{3.2.34} $$

This means that the total power generated by the stator and rotor circuits is given by

$$ P_e = P_s + P_r = \frac{3}{2}\left(v_{qs} i_{qs} + v_{ds} i_{ds}\right) + \frac{3}{2}\left(v_{qr} i_{qr} + v_{dr} i_{dr}\right). \tag{3.2.35} $$

Substituting v_{qs}, v_{ds}, v_{qr}, and v_{dr} from the voltage equations in (3.2.21) through (3.2.24) into (3.2.35), assuming an arbitrary rotating speed,ω, for the $dq0$ reference frame, yields

$$ \begin{aligned} P_e &= P_s + P_r \\ &= \frac{3}{2}\left(\left(\frac{d\lambda_{qs}}{dt} - R_s i_{qs} + \omega\lambda_{ds}\right) i_{qs} + \left(\frac{d\lambda_{ds}}{dt} - R_s i_{ds} - \omega\lambda_{qs}\right) i_{ds} \right) \\ &+ \frac{3}{2}\left(\left(\frac{d\lambda_{qr}}{dt} + R_r i_{qr} + (\omega - \omega_r)\lambda_{dr} \right) i_{qr} \right. \\ &\left. + \left(\frac{d\lambda_{dr}}{dt} + R_r i_{dr} - (\omega - \omega_r)\lambda_{qr} \right) i_{dr} \right). \end{aligned} \tag{3.2.36} $$

This equation can be rearranged and then written as

$$P_e = \frac{3}{2}\left(-R_s i_{qs}^2 - R_s i_{ds}^2 + R_r i_{qr}^2 + R_r i_{dr}^2\right) + \frac{3}{2}\left(\frac{d\lambda_{qs}}{dt} i_{qs} + \frac{d\lambda_{ds}}{dt}\ i_{ds} + \frac{d\lambda_{qr}}{dt} i_{qr} + \frac{d\lambda_{dr}}{dt} i_{dr}\right)$$

$$+ \frac{3}{2}\left(\omega\lambda_{ds} i_{qs} - \omega\lambda_{qs} i_{ds} + (\omega - \omega_r)\lambda_{dr} i_{qr} - (\omega - \omega_r)\lambda_{qr} i_{dr}\right) \qquad (3.2.37)$$

As shown in (3.2.37), electrical power can be divided into three terms. The first term represents power dissipations in the stator and rotor windings. The second term relates to the time rate of change of magnetic energy stored in inductances of the stator and rotor windings. The third term contributes to the power conversion from mechanical to electrical. Therefore, electromechanical power is given by

$$P_{em} = \frac{3}{2}\left(\omega\lambda_{ds} i_{qs} - \omega\lambda_{qs} i_{ds} + (\omega - \omega_r)\lambda_{dr} i_{qr} - (\omega - \omega_r)\lambda_{qr} i_{dr}\right) \qquad (3.2.38)$$

This equation is valid for an arbitrary reference frame with an angular speed, ω, so it must also be valid for any speed including the rotor speed $\omega = \omega_r$ meaning that [29]

$$P_{em} = \frac{3}{2}\omega_r\left(\lambda_{ds} i_{qs} - \lambda_{qs} i_{ds}\right) \qquad (3.2.39)$$

Accordingly, the developed electrical torque, T_e, is calculated by

$$T_e = \frac{P_{em}}{\omega_G}. \qquad (3.2.40)$$

Using (3.2.39), and (3.2.8), then

$$T_e = \frac{3}{2}\frac{p}{2}\left(\lambda_{ds} i_{qs} - \lambda_{qs} i_{ds}\right) \qquad (3.2.41)$$

where T_e is not a function of ω, and therefore (as expected) the torque expression is valid for any reference frame, regardless of the angular speed.

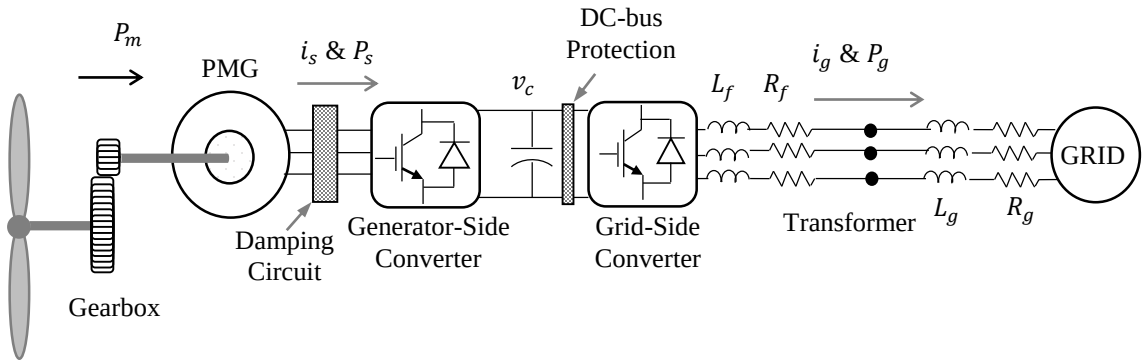

Figure 3.5 Schematic of a PMG based wind turbine system

3.3 Permanent Magnet Generator

In a (PMG), the necessary magnetic field is provided by a permanent magnet mounted on the generator's rotor. The PMG belongs to the synchronous generator category, however, no windings, external DC power supply, or rings are needed on the rotor therefore they require less maintenances. PMGs have received attention from the wind turbine industry because they do not require a multi-stage gearbox, further reducing wind turbine maintenance costs.

Similar to DFIG topology, the stator windings for PMGs correspond to three phases: phase-a, phase-b, and phase-c. However, no windings exist in the rotor, and stator terminals are indirectly connected to the power grid through a back-to-back converter, as shown in Figure. 3.5.

3.3.1 *PMG Model in the abc-Reference Frame*

As the stator windings are electrically structured similar to the one in a DFIG, the stator voltage equations are similarly written as

$$\begin{bmatrix} v_{as} \\ v_{bs} \\ v_{cs} \end{bmatrix} = -\begin{bmatrix} R_s & 0 & 0 \\ 0 & R_s & 0 \\ 0 & 0 & R_s \end{bmatrix} \begin{bmatrix} i_{as} \\ i_{bs} \\ i_{cs} \end{bmatrix} + \frac{d}{dt} \begin{bmatrix} \lambda_{as} \\ \lambda_{bs} \\ \lambda_{cs} \end{bmatrix} \tag{3.3.1}$$

where the stator linkage flux includes the stator and rotor effects (i.e., $\lambda_{abc}^{s} = \lambda_{abc}^{ss} + \lambda_{abc}^{sr}$). The only difference is that the term λ_{abc}^{sr} is produced by the permanent magnets. Therefore the flux linkage equations can be written as

$$\begin{bmatrix}\lambda_{as}\\ \lambda_{bs}\\ \lambda_{cs}\end{bmatrix} = -\begin{bmatrix} L_{ls}+L_m & -\frac{1}{2}L_m & -\frac{1}{2}L_m \\ -\frac{1}{2}L_m & L_{ls}+L_m & -\frac{1}{2}L_m \\ -\frac{1}{2}L_m & -\frac{1}{2}L_m & L_{ls}+L_m \end{bmatrix}\begin{bmatrix} i_{as}\\ i_{bs}\\ i_{cs}\end{bmatrix} - \begin{bmatrix} \Lambda_m \cos(\theta_r) \\ \Lambda_m \cos\left(\theta_r - \frac{2\pi}{3}\right) \\ \Lambda_m \cos\left(\theta_r + \frac{2\pi}{3}\right)\end{bmatrix} \tag{3.3.2}$$

where Λ_m is the magnetic linkage flux produced by the rotor permanent magnets. No equation is needed for the generator rotor circuit.

3.3.2 *PMG Model in the $dq0$-Reference Frame*

Using the $dq0$ transformation matrix, T_{θ_s}, and its inverse, $T_{\theta_s}^{-1}$, the stator circuit equations can be rewritten as

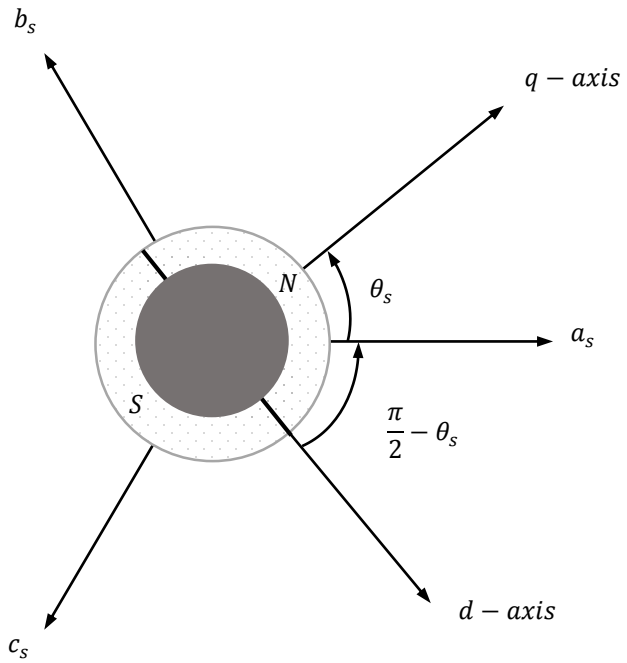

Figure 3.6 Stator and rotor magnetic axes of a three-phase permanent magnet machine

$$\begin{bmatrix} v_{qs} \\ v_{ds} \\ v_{0s} \end{bmatrix} = -T_{\theta_s} \begin{bmatrix} R_s & 0 & 0 \\ 0 & R_s & 0 \\ 0 & 0 & R_s \end{bmatrix} T_{\theta_s}^{-1} \begin{bmatrix} i_{qs} \\ i_{ds} \\ i_{0s} \end{bmatrix} + T_{\theta_s} \frac{d}{dt} \left\{ T_{\theta_s}^{-1} \begin{bmatrix} \lambda_{qs} \\ \lambda_{ds} \\ \lambda_{0s} \end{bmatrix} \right\} \tag{3.3.3}$$

In synchronous machines (herein generators), the rotor and the synchronous speeds are identical. Hence, the d-axis can aligned with the magnetic axis of the rotor (i.e., $\theta_r = \frac{\pi}{2} - \theta_s$) as shown in Figure 3.6. Therefore, θ_r in (3.3.2) can be replaced by $\frac{\pi}{2} - \theta_s$, and (3.3.3) is then simplified as

$$\begin{bmatrix} v_{qs} \\ v_{ds} \\ v_{0s} \end{bmatrix} = -\begin{bmatrix} R_s & 0 & 0 \\ 0 & R_s & 0 \\ 0 & 0 & R_s \end{bmatrix} \begin{bmatrix} i_{qs} \\ i_{ds} \\ i_{0s} \end{bmatrix} + \frac{d}{dt} \begin{bmatrix} \lambda_{qs} \\ \lambda_{ds} \\ \lambda_{0s} \end{bmatrix} + \begin{bmatrix} 0 & \omega_s & 0 \\ -\omega_s & 0 & 0 \\ 0 & 0 & 0 \end{bmatrix} \begin{bmatrix} \lambda_{qs} \\ \lambda_{ds} \\ \lambda_{0s} \end{bmatrix}. \tag{3.3.4}$$

Stator flux linkage equations can also be converted to the $dq0$ reference frame:

$$\begin{bmatrix} \lambda_{qs} \\ \lambda_{ds} \\ \lambda_{0s} \end{bmatrix} = -T_{\theta_s} \begin{bmatrix} L_{ls} + L_m & -\frac{1}{2}L_m & -\frac{1}{2}L_m \\ -\frac{1}{2}L_m & L_{ls} + L_m & -\frac{1}{2}L_m \\ -\frac{1}{2}L_m & -\frac{1}{2}L_m & L_{ls} + L_m \end{bmatrix} T_{\theta_s}^{-1} \begin{bmatrix} i_{qs} \\ i_{ds} \\ i_{0s} \end{bmatrix}$$

$$-T_{\theta_s} \begin{bmatrix} \Lambda_m \cos\left(\frac{\pi}{2} - \theta_s\right) \\ \Lambda_m \cos\left(\frac{\pi}{2} - \theta_s - \frac{2\pi}{3}\right) \\ \Lambda_m \cos\left(\frac{\pi}{2} - \theta_s + \frac{2\pi}{3}\right) \end{bmatrix}. \tag{3.3.5}$$

After mathematical manipulations, (3.3.5) can be simplified as

$$\begin{bmatrix} \lambda_{qs} \\ \lambda_{ds} \\ \lambda_{0s} \end{bmatrix} = -\begin{bmatrix} L_{ls} + L_M & 0 & 0 \\ 0 & L_{ls} + L_M & 0 \\ 0 & 0 & L_{ls} \end{bmatrix} \begin{bmatrix} i_{qs} \\ i_{ds} \\ i_{0s} \end{bmatrix} - \begin{bmatrix} 0 \\ \Lambda_m \\ 0 \end{bmatrix} \tag{3.3.6}$$

where, $L_M = \frac{3}{2}L_m$.

3.3.3 *Block Diagram Representation of PMG Model*

In this subsection, the block diagram representation of PMG is presented using the developed equations from the previous subsection. For a balanced PMG, only the two d-axis and q- axis equations are needed, and 0- quantities can be ignored. Therefore, the electrical part of a PMG model can be represented by two algebraic and two differential equations, as seen in

$$\lambda_{qs} = -(L_{ls} + L_M)i_{qs} \tag{3.3.7}$$

$$\lambda_{ds} = -(L_{ls} + L_M)i_{ds} - \Lambda_m \tag{3.3.8}$$

$$\frac{d\lambda_{qs}}{dt} = v_{qs} + R_s i_{qs} - \omega_s \lambda_{ds} \tag{3.3.9}$$

$$\frac{d\lambda_{ds}}{dt} = v_{ds} + R_s i_{ds} + \omega_s \lambda_{qs}. \tag{3.3.10}$$

These equations can be combined into two state-space equations as

$$\frac{d\lambda_{qs}}{dt} = v_{qs} - \frac{R_s}{L_s}\lambda_{qs} - \omega_s \lambda_{ds} \tag{3.3.11}$$

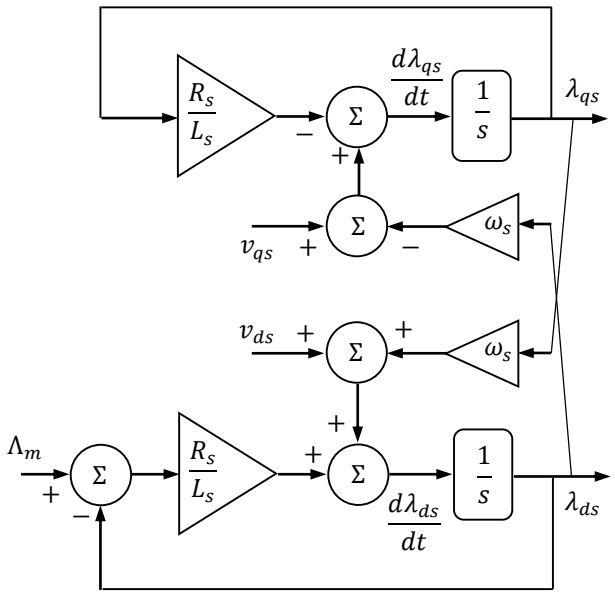

Figure 3.7 Stator flux, λ_{qs} and λ_{ds}, (state variables) calculations from input signals, v_{qs} , v_{ds} and Λ_m

$$\frac{d\lambda_{ds}}{dt} = v_{ds} + \frac{R_s}{L_s}\Lambda_m - \frac{R_s}{L_s}\lambda_{ds} + \omega_s\lambda_{qs} \tag{3.3.12}$$

where L_s is equal to $L_{ls} + L_M$. Figure 3.7 shows a model of the electrical portion of a PMG in a block diagram format. Furthermore, the electrical torque, T_e, formula in (3.2.20) is also valid for a PMG; the torque formula is written only in terms of the stator quantities.

3.4 Back-to-Back Converter

Solid-state-based converters have much faster dynamics than the windmill and generator, therefore, in order to study the slow dynamic phenomena, generator- and grid-side converters can be modeled by their controllers and first-order transfer functions as shown in Figures 3.8 and 3.9. Using KVL for the low-pass filter at the AC side of the grid-side converter shows

$$\begin{bmatrix} v_{as} \\ v_{bs} \\ v_{cs} \end{bmatrix} = \begin{bmatrix} R_f & 0 & 0 \\ 0 & R_f & 0 \\ 0 & 0 & R_f \end{bmatrix} \begin{bmatrix} i_{ai} \\ i_{bi} \\ i_{ci} \end{bmatrix} + \begin{bmatrix} L_f & 0 & 0 \\ 0 & L_f & 0 \\ 0 & 0 & L_f \end{bmatrix} \frac{d}{dt} \begin{bmatrix} i_{ai} \\ i_{bi} \\ i_{ci} \end{bmatrix} + \begin{bmatrix} v_{ai} \\ v_{bi} \\ v_{ci} \end{bmatrix}. \tag{3.4.1}$$

This can be converted to the $dq0$-reference-frame as

$$T_{\theta_s}^{-1} \begin{bmatrix} v_{as} \\ v_{bs} \\ v_{cs} \end{bmatrix} = \begin{bmatrix} R_f & 0 & 0 \\ 0 & R_f & 0 \\ 0 & 0 & R_f \end{bmatrix} T_{\theta_s}^{-1} \begin{bmatrix} i_{qi} \\ i_{di} \\ i_{0i} \end{bmatrix} + \begin{bmatrix} L_f & 0 & 0 \\ 0 & L_f & 0 \\ 0 & 0 & L_f \end{bmatrix} \frac{d}{dt} \left\{ T_{\theta_s}^{-1} \begin{bmatrix} i_{qi} \\ i_{di} \\ i_{0i} \end{bmatrix} \right\} + T_{\theta_s}^{-1} \begin{bmatrix} v_{qi} \\ v_{di} \\ v_{0i} \end{bmatrix}. \tag{3.4.2}$$

Multiplication of both sides by T_{θ_s} yields

$$\begin{bmatrix} v_{as} \\ v_{bs} \\ v_{cs} \end{bmatrix} = T_{\theta_s} \begin{bmatrix} R_f & 0 & 0 \\ 0 & R_f & 0 \\ 0 & 0 & R_f \end{bmatrix} T_{\theta_s}^{-1} \begin{bmatrix} i_{qi} \\ i_{di} \\ i_{0i} \end{bmatrix} + T_{\theta_s} \begin{bmatrix} L_f & 0 & 0 \\ 0 & L_f & 0 \\ 0 & 0 & L_f \end{bmatrix} \frac{d}{dt} \left\{ T_{\theta_s}^{-1} \begin{bmatrix} i_{qi} \\ i_{di} \\ i_{0i} \end{bmatrix} \right\} + T_{\theta_s} T_{\theta_s}^{-1} \begin{bmatrix} v_{qi} \\ v_{di} \\ v_{0i} \end{bmatrix}. \tag{3.4.3}$$

which simplified as

$$\begin{bmatrix} v_{qs} \\ v_{ds} \\ v_{0s} \end{bmatrix} = \begin{bmatrix} R_f & 0 & 0 \\ 0 & R_f & 0 \\ 0 & 0 & R_f \end{bmatrix} \begin{bmatrix} i_{qi} \\ i_{di} \\ i_{0i} \end{bmatrix} + \begin{bmatrix} L_f & 0 & 0 \\ 0 & L_f & 0 \\ 0 & 0 & L_f \end{bmatrix} \frac{d}{dt} \begin{bmatrix} i_{qi} \\ i_{di} \\ i_{0i} \end{bmatrix}$$

$$+\begin{bmatrix} 0 & \omega_s L_f & 0 \\ -\omega_s L_f & 0 & 0 \\ 0 & 0 & 0 \end{bmatrix}\begin{bmatrix} i_{qi} \\ i_{di} \\ i_{0i} \end{bmatrix} + \begin{bmatrix} v_{qi} \\ v_{di} \\ v_{0i} \end{bmatrix}. \tag{3.4.4}$$

The grid-side converter is connected to the grid through an RL circuit that is a simplified representation of the low-pass filter and step-up transformer shown in Figure. 3.1. Again by neglecting 0-quantities, voltage at the inverter (grid-side converter) terminals, v_{qi} and v_{di}, are obtained from

$$v_{qi} = v_{qs} - R_f i_{qi} - L_f \frac{di_{qi}}{dt} - \omega_s L_f i_{di} \tag{3.4.5}$$

$$v_{di} = v_{ds} - R_f i_{di} - L_f \frac{di_{di}}{dt} + \omega_s L_f i_{qi} \tag{3.4.6}$$

In the grid-side converter, DC-bus voltage and power must be measured. The power can be calculated as

$$P_i = \frac{3}{2}\left(v_{qi} i_{qi} + v_{di} i_{di}\right) \tag{3.4.7}$$

where v_{qi} and v_{di} are the quadrature and direct inverter voltages, respectively. Herein, i_{di} is set to zero; therefore, the grid-side converter with the low-pass filter model is shown in Figure 3.8. The the Laplace transform of the q-axis inverter voltage is given by $V_{qi} = V_{qs} - (L_s s + R_s) I_{qi}$, which includes the derivative of the current, i_{qi}. A differentiation operator may cause numerical

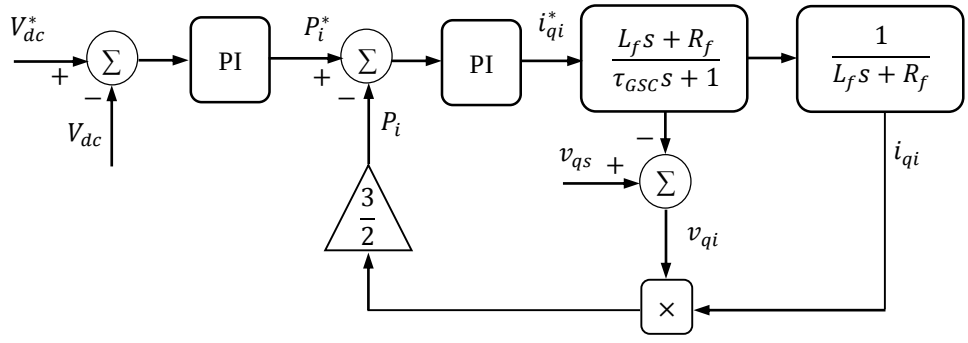

Figure 3.8 Grid-side converter model with a simplified low-pass filter, i_{di} is set to zero and i_{qi} is controlled based on the desired DC-bus voltage, V_{dc}^*

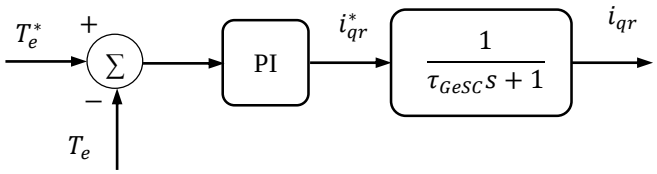

Figure 3.9 Rotor-side converter, i_{dr} is set to zero and i_{qr} is controlled based on the desired generator torque, T_e^*

issues in a simulation; therefore, a time derivation, $\frac{d}{dt}$, with Laplace transform of s, is modeled as $\frac{s}{\tau s+1}$, where τ should be relatively small [49], [50]. In this work, the converter reduced-order model is combined with the filter model as $V_{qi} = V_{qs} - \frac{L_s s+R_s}{\tau_{GSC}s+1} i_{qi}^*$, where i_{qi}^* is the desired value of q-axis current at the inverter (grid-side) terminal. Similarly, for the rotor-side converter, i_{dr} is set to zero, and i_{qr} is controlled based on the desired electrical torque, T_e^*, as shown in Figure 3.9.

The q-axis and d-axis stator voltages, v_{qs} and v_{ds}, are then given by

$$v_{qs} = v_{qg} + R_g(i_{qs} - i_{qi}) + L_g \frac{d(i_{qs} - i_{qi})}{dt} + \omega_s L_g(i_{ds} - i_{di}) \tag{3.4.8}$$

$$v_{ds} = v_{dg} + R_g(i_{ds} - i_{di}) + L_g \frac{d(i_{ds} - i_{di})}{dt} - \omega_s L_g(i_{qs} - i_{qi}) \tag{3.4.9}$$

where R_g is the feeder line resistance and L_g is the feeder line inductance. Also, v_{qg} and v_{dg} are the grid-side voltages that are calculated by

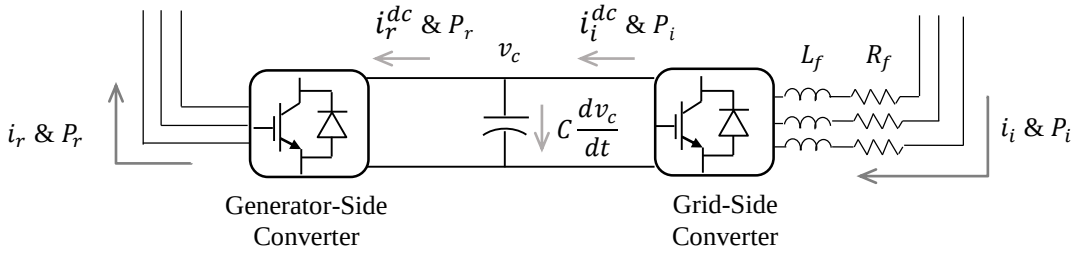

Figure 3.10 DC-bus voltage dynamics behavior in terms of powers in both sides of the back-to-back converter

$$\begin{bmatrix} v_{qg} \\ v_{dg} \\ v_{0g} \end{bmatrix} = T_{\theta_s} \begin{bmatrix} v_{ag} \\ v_{bg} \\ v_{cg} \end{bmatrix} = T_{\theta_s} \begin{bmatrix} V_m \cos(\omega_s t) \\ V_m \cos\left(\omega_s t - \frac{2\pi}{3}\right) \\ V_m \cos\left(\omega_s t + \frac{2\pi}{3}\right) \end{bmatrix} = \begin{bmatrix} V_m \\ 0 \\ 0 \end{bmatrix}. \tag{3.4.10}$$

The DC-bus voltage stays at its nominal value by controlling the flow of power from the grid to the rotor. Neglecting the converters' switching losses and using KCL, the DC-bus voltage can be formulated as

$$C\frac{dv_{dc}}{dt} = i_i^{dc} - i_r^{dc} \tag{3.4.11}$$

where, C is the DC-bus capacitor. Multiplying both sides by the DC-bus voltage, v_{dc}, yields

$$Cv_{dc}\frac{dv_{dc}}{dt} = P_i - P_r \tag{3.4.12}$$

where, $P_r = \frac{3}{2}\left(v_{qr}i_{qr} + v_{dr}i_{dr}\right)$ is the rotor/generator side power and P_i is the grid-side converter power, as shown in Figure 3.10. Because $2v_{dc}\frac{dv_{dc}}{dt} = \frac{d}{dt}(v_{dc})^2$, then (3.4.10) can be written as

$$\frac{d}{dt}(v_{dc})^2 = \frac{2}{C}(P_i - P_r). \tag{3.4.13}$$

This nonlinear differential equation represents DC-bus dynamics. Although the desired electrical torque identifies the desired value of i_{qr} in the generator-side converter, for the grid-side converter,

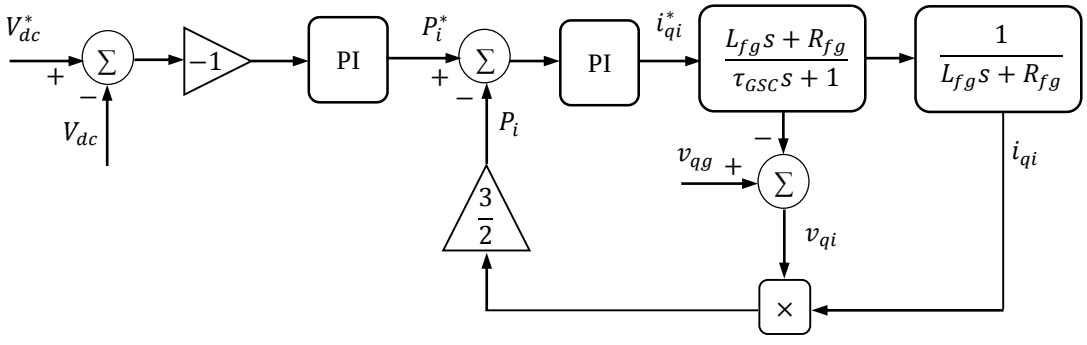

Figure 3.11 Grid side converter model with a simplified low-pass filter of PMG, where i_{di} is set to zero and i_{qi} is controlled based on the desired DC-bus voltage, V_{dc}^*

the desired value of the DC-bus voltage identifies the desired value of active power and subsequently commands the desired value of i_{qi}, as shown in Figures 3.10 and 3.11.

In the PMG block diagram in Figure 3.10, the power flow direction through the back-to-back converter is opposite to the one in the DFIG-based block diagram. Therefore, as the grid-side converter current/power increases, the DC-bus voltage decreases. This reverse proportionality is shown in the block diagram in Figure 3.11 by a negative gain inserted in series with the first PI controller from the left side. Also, the DC-bus voltage and the filter equations for the PMG system should be written as

$$\frac{d}{dt}(v_{dc})^2 = \frac{2}{C}(P_r - P_i) \tag{3.4.14}$$

$$v_{qi} = v_{qg} + \left(R_f + R_g\right)i_{qi} + (L_f + L_g)\frac{di_{qi}}{dt} + \omega_s(L_f + L_g)i_{di} \tag{3.4.15}$$

$$v_{di} = v_{dg} + \left(R_f + R_g\right)i_{di} + (L_f + L_g)\frac{di_{di}}{dt} - \omega_s(L_f + L_g)i_{qi} \tag{3.4.16}$$

which includes the feeder line resistance, R_g, and inductance, L_g, effects. In Figure 3.11, L_{fg} stands for $L_f + L_g$, and $R_{fg} = R_f + R_g$.

3.5 Series-Compensated Power Line

Wind farms are typically connected to the grid through a long transmission line. However, use of a long transmission line to transfer wind farm power to the grid reduces power transmission capacity because of the large inductance of long transmission lines. One economical solution to improve power transmission capacity is the use of a series capacitor to reduce effective inductance of the line, thereby increasing overall system stability.

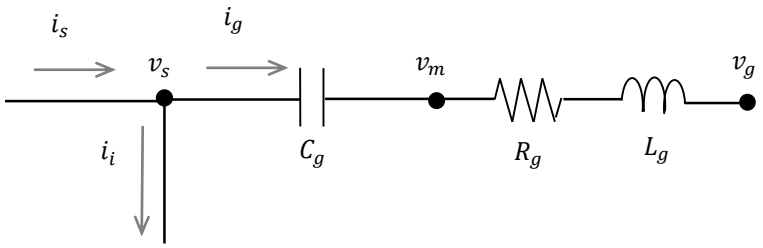

Figure 3.12 Transmission line model with a series compensation capacitor

Figure 3.12 illustrates a series compensation capacitor in the power transmission line in a DFIG-based system. In order to model the effect of a series capacitor, $i - v$ relation for series capacitors is

$$\begin{bmatrix} i_{ag} \\ i_{bg} \\ i_{cg} \end{bmatrix} = \begin{bmatrix} \mathrm{C} & 0 & 0 \\ 0 & \mathrm{C} & 0 \\ 0 & 0 & C \end{bmatrix} \frac{d}{dt} \begin{bmatrix} v_{as} - v_{am} \\ v_{bs} - v_{bm} \\ v_{cs} - v_{cm} \end{bmatrix} \tag{3.5.1}$$

where i_g, v_s, and v_m are shown in Figure 3.12 Using Park's transformation, (3.5.1) can be written as

$$T_{\theta_s}^{-1} \begin{bmatrix} i_{qg} \\ i_{dg} \\ i_{0g} \end{bmatrix} = \begin{bmatrix} C & 0 & 0 \\ 0 & C & 0 \\ 0 & 0 & C \end{bmatrix} \frac{d}{dt} \left\{ T_{\theta_s}^{-1} \begin{bmatrix} \Delta v_q \\ \Delta v_d \\ \Delta v_0 \end{bmatrix} \right\} \tag{3.5.2}$$

where Δv_q and Δv_d represent voltage drops across the series capacitor in the transmission line.

$$\begin{bmatrix} i_{qg} \\ i_{dg} \\ i_{0g} \end{bmatrix} = T_\theta \begin{bmatrix} C & 0 & 0 \\ 0 & C & 0 \\ 0 & 0 & C \end{bmatrix} T_\theta^{-1} \left\{ \frac{d}{dt} \begin{bmatrix} v_q \\ v_d \\ v_0 \end{bmatrix} \right\} + T_\theta \begin{bmatrix} C & 0 & 0 \\ 0 & C & 0 \\ 0 & 0 & C \end{bmatrix} \left\{ \frac{d}{dt} T_\theta^{-1} \right\} \begin{bmatrix} \Delta v_q \\ \Delta v_d \\ \Delta v_0 \end{bmatrix} \tag{3.5.3}$$

which can further be simplified as

$$\begin{bmatrix} i_{qg} \\ i_{dg} \\ i_{og} \end{bmatrix} = \begin{bmatrix} \mathrm{C} & 0 & 0 \\ 0 & \mathrm{C} & 0 \\ 0 & 0 & C \end{bmatrix} \frac{d}{dt} \begin{bmatrix} \Delta v_q \\ \Delta v_d \\ \Delta v_0 \end{bmatrix} + \begin{bmatrix} 0 & \omega_s C & 0 \\ -\omega_s C & 0 & 0 \\ 0 & 0 & 0 \end{bmatrix} \begin{bmatrix} \Delta v_q \\ \Delta v_d \\ \Delta v_0 \end{bmatrix}. \tag{3.5.4}$$

Again, for balanced three-phase systems, only q-axis and d- axis quantities are considered and the grid currents become

$$i_{qg} = C\frac{d\Delta v_q}{dt} + \omega_s C\Delta v_d \tag{3.5.5}$$

$$i_{dg} = C\frac{d\Delta v_d}{dt} - \omega_s C\Delta v_q. \tag{3.5.6}$$

In order to solve for the voltage drops, these equations must be converted to the s-domain using the Laplace transform, which yields

$$\begin{bmatrix}\Delta v_q \\ \Delta v_d\end{bmatrix} = \begin{bmatrix}Cs & \omega_s C \\ -\omega_s C & Cs\end{bmatrix}^{-1}\begin{bmatrix}i_{qg} \\ i_{dg}\end{bmatrix}. \tag{3.5.7}$$

Therefore, the voltage drops are obtained from

$$\begin{bmatrix}\Delta v_q \\ \Delta v_d\end{bmatrix} = \frac{1}{C^2S^2 + \omega_s^2 C^2}\begin{bmatrix}Cs & -\omega_s C \\ \omega_s C & Cs\end{bmatrix}\begin{bmatrix}i_{qg} \\ i_{dg}\end{bmatrix}. \tag{3.5.8}$$

which can be rewritten as

$$\Delta v_q = \frac{\frac{s}{C}}{s^2 + \omega_s^2} i_{qg} - \frac{\frac{\omega_s}{C}}{s^2 + \omega_s^2} i_{dg} \tag{3.5.9}$$

$$\Delta v_d = \frac{\frac{s}{C}}{s^2 + \omega_s^2} i_{dg} + \frac{\frac{\omega_s}{C}}{s^2 + \omega_s^2} i_{qg}. \tag{3.5.10}$$

These equations can be combined with the transmission line equations as shown in Figure 3.13 for only the q-axis.

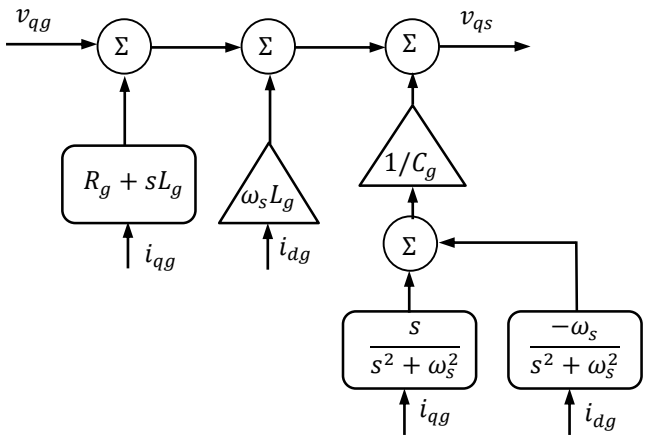

Figure 3.13 Series capacitor implementation into the transmission line model (neglecting parallel capacitors) for the q-axis; the d-axis model can be similarly implemented

3.6 Developed Model Verifications for Constant Electrical Torque

Various simulation results throughout Chapters 4 and 5 demonstrate the effectiveness of the developed models to enabling analysis dynamic phenomena in DFIG-based and PMG-based wind turbine systems. For example, a voltage dip disturbance in the grid can excite eigenvalues of the wind turbine drivetrain. This well-known phenomenon is observed using the developed models, where the frequency of oscillations matches the expected natural frequency of the drivetrain, as discussed in Chapter 5.

As the FAST aerodynamic model has been verified by NREL, herein only the power balancing in sub-synchronous and super-synchronous modes of operation in the 5MW DFIG-based system is examined. In the results presented in Figure 3.14, the 5MW DFIG-based wind turbine model was run at a constant electrical torque of 1.4 kNm when the wind speeds were 7 m/s and 10 m/s. In this test, the 1.4 kNm was chosen such that the system operates at its maximum power seeking ($C_p = 0.48$) for the wind speed of 7 m/s. The measured data points are shown at $t = 800$ sec and $t = 1400$ sec in Figure 3.14. The first observation is that the stator power remains constant as the wind speed varies. In a synchronously rotating reference frame fixed on the grid frequency, $v_{ds} \cong v_{dg} = 0$ and $v_{qs} \cong v_{qg} = V_m$, as given in Equation (3.4.10). Therefore, the stator power is obtained rom $P_s = \frac{3}{2} V_m(i_{qs})$, and thus it stays constant for a given electrical torque. However, the net generated power given by $P_{aero} \cong P_g = P_s - P_i$ (based on the defined directions in Figure 3.1), varies as the wind speed changes. This can be examined using the data provided in Figure 3.14. It is known that both rotor and stator generate power under super-synchronous mode of operation and only the stator circuit generate power under sub-synchronous mode [41]. This fact is examined as follows

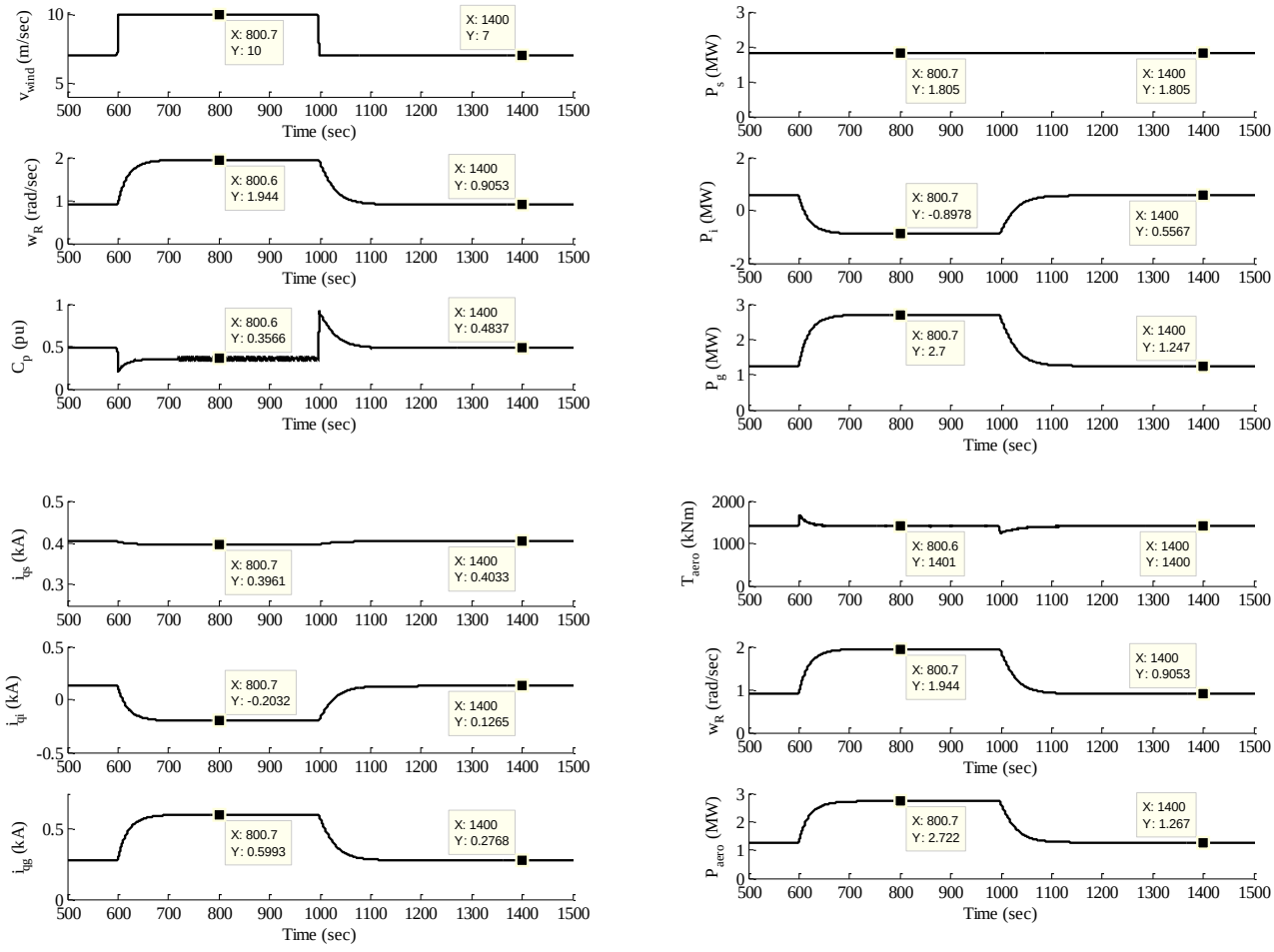

Figure 3.14 Test results of the 5MW DFIG-based wind turbine for a contestant electrical torque

At $t = 800$ sec when the wind speed is 10 m/s, the generated power is $P_g = P_s - P_i = 1.805 + 0.8979 = 2.7$ MW that means both stator and rotor inject power into the grid. Also, the generator speed is $n_{Gen} = N_{gear}\left(\frac{60}{2\pi}\right)\omega_R = 97\left(\frac{60}{2\pi}\right)1.944 = 1800$ rpm, while the synchronous speed for a 6-pole generator is 1200 rpm, therefore as expected the generator operates at super-synchronous mode in this case.

At $t = 1400$ sec when the wind speed is 7 m/s, the generated power is $P_g = P_s - P_i = 1.805 - 0.5567 = 1.247$ MW that means only stator generates power. Also, the generator speed

is $n_{Gen} = N_{gear}\left(\frac{60}{2\pi}\right)\omega_R = 97\left(\frac{60}{2\pi}\right)0.9053 = 838$ rpm, which is less than the synchronous speed and therefore, as expected, the generator operates at sub-synchronous mode.

Chapter 4 – Nonlinear Control Scheme for Extremum Power Seeking

This chapter begins with a background of extremum power-seeking techniques, with emphasis on the perturb-and-observe method and the conventional $k\omega^2$ technique. Also, a background on nonlinear control schemes, Lyapunov, and feedback linearization methods are explained through a second-order example. Then these concepts are applied to develop a nonlinear adaptive extremum power-seeking method. At the end of this chapter, the developed extremum power seeking method is verified through simulation results and compared to the conventional technique.

4.1 Background of Extremum Power Seeking Strategies

Many maximum power-seeking or extremum power-seeking methods have been presented in literature, but two classical methods are presented in the following. In particular, the second method described below is used as benchmark of the developed method presented in this dissertation.

4.1.1 *Perturb-and-Observe Method of Extremum Power Seeking*

Maximum power capturing can be achieved by continuous change of the control variable and observation of the resulting change in power. These algorithms are known as perturb-and-observe or hill climbing, as well as torque and/or speed control based on pre-known system parameters such as the $k\omega^2$ technique. Because these methods do not require information about system parameters, they are independent, simple and flexible. In this method the power and rotor speed increment are sampled and the sign of each is calculated. Based on the sign, a new incremental or decrement of the reference value is calculated. Choosing an appropriate step size is the most important task in this method because it is a compromise between response time and

steady state oscillation. A drawback of this method is the deficiency of difference between power that results from wind speed changes or perturbation change in the system that can cause failure of the maximum seeking.

One algorithm is based on an injected dither signal [14]. This algorithm can best be explained using a typical power curve, P_T versus ω_R of a turbine at a constant wind speed as shown in Figure 4.1. By adding a dither signal equal to $a\ sin(\omega_{dit}t)$ to the reference speed, where a is a constant, the wind turbine control scheme estimates the gradient of the output power. The dither frequency is very slow with respect to dynamics of the overall wind turbine and its amplitude is sufficiently small compared to the rotor speed. The dither signal creates an alternating signal with the same frequency (i.e., $P_T = p_{DC} + a\ k\ sin(\omega_{dit}\ t)$), where k is an estimate of the slope of P_T with respect to ω_R. In order to estimate the gradient of the output power, a high-pass filter is used to remove the DC component of the signal. Then the resulting signal is multiplied by

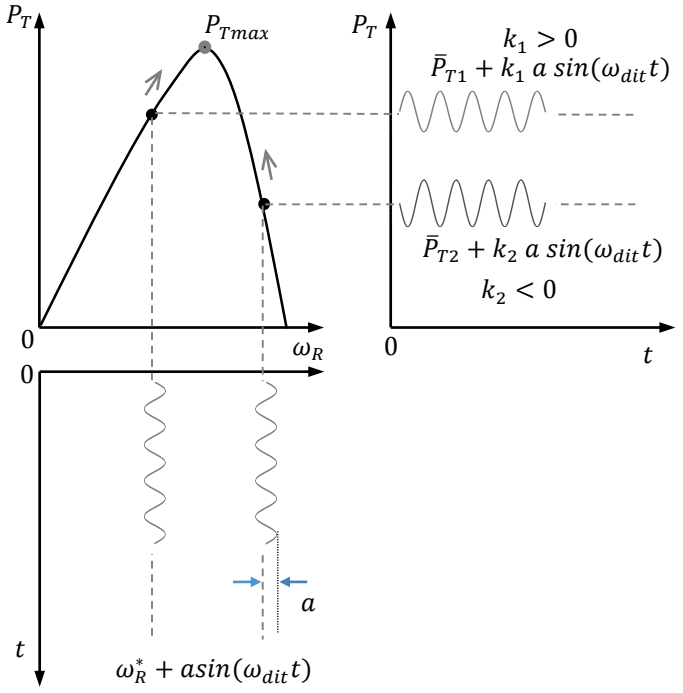

Figure 4.1 Maximum seeking approach via adding a dither signal to the reference signal.

$(2/a)\sin(\omega_{dit}t)$, (i.e., $(2/a\ \sin(\omega_{dit}\ t))(ak\sin(\omega_{dit}\ t))$, which can be simplified as $k - kcos(2\omega_{dit}\ t)$. A low-pass filter is used to remove the AC component of the product in order to obtain the gradient estimation of P_T. Depending on the sign of estimated gradient, (i.e. sign of k) the output of the integrator is either added to (or subtracted from) the reference speed, ω_R^*, and therefore, the desired speed increases or decreases to capture greater power.

4.1.2 *Conventional Method of Extremum Power Seeking*

In the conventional method, the electrical torque is set to be proportional to the generator (or rotor) speed. The main idea is derived from the aerodynamics of wind turbines. As discussed in Chapter 2, aerodynamic torque is formulated as

$$T_{aero} = \frac{C_p(\lambda,\beta)}{2\omega_R}\rho\pi R^2 v^3. \tag{4.1.1}$$

If the optimal rotor tip speed ratio, λ^{opt}, is assumed a constant value where $C_p(\lambda,\beta) = C_p^{opt}$, then (4.1.1) can be written as

$$T_{aero} = \frac{C_p^{opt}}{2\omega_R}\rho\pi R^2\left(\frac{R\omega_R}{\lambda^{opt}}\right)^3 \tag{4.1.2}$$

which can be simplified as

$$T_{aero} = \frac{\rho\pi R^5 C_p^{opt}}{2\lambda^{opt^2}}{\omega_R}^2\,. \tag{4.1.3}$$

Hence, T_{aero} and T_e are essentially equal and opposite for steady wind conditions and the electrical torque can be written

$$T_e = k_{opt}\,{\omega_R}^2. \tag{4.1.4}$$

Although this technique provides an easy control law for capturing extremum power in wind turbines, k_{opt} may change in time due to aging of the wind turbine [51]. In order to overcome this drawback, an adaptive nonlinear control method is developed in the work for this dissertation.

4.2 Background of Nonlinear Feedback Linearization and Lyapunov Methods

Prior to the main discussion on formulations of the proposed method for extremum power seeking, general information about nonlinear techniques of feedback linearization and Lyapunov methods are presented in the following subsections.

4.2.1 *Lyapunov Function Applications in Control Systems*

In general, control theory has two branches: linear and nonlinear control schemes. However, majority of real-world problems are nonlinear systems. In order to design a control scheme, the system dynamic behavior first should be modeled by an n^{th}order differential equation, or by n first-order differential equations. If these equations are linear or can be linearized around an operating point (Jacobian linearization), then linear control theories, such as pole-placement technique, can be applied. Let us define an n^{th} −order system as

$$\dot{x} = f_k(x, u, t) \qquad k = 1, \dots, n \tag{4.2.5}$$

where $f_k \, \epsilon R^n$ is a nonlinear function, $x = [x_1 \quad \cdots \quad x_n]^T$ is the state vector of the system, and $u = [u_1 \quad \dots \quad u_m]^T$ is the input/reference vector. This type of systems can be controlled using linear control theory (e.g., PID controllers) for simple nonlinear systems, such as in power controllers. However, the controller may not provide optimal performance for all operating conditions. The Lyapunov method is used for stability analysis of nonlinear dynamic systems and extraction of control laws that maintain system stability over the range of operating conditions. The second approach is to use the feedback linearization to cancel known nonlinear terms using

feedback loops, that are superimposed with pole placement loops to secure the stability of the overall system. The major issue with this technique is that the nonlinear terms are not always known. The third well-known method is based on sliding mode theory in which the nonlinearity terms are not known. The latter is explained in Chapter 5, but, the Lyapunov and feedback linearization techniques are briefly explained in the following paragraphs.

The Lyapunov method is based on a fundamental physical concept that if energy of a system monotonically decreases after a finite excitation or disturbance, the system will eventually settle down to an equilibrium condition. The Lyapunov method is used to analyze the stability of a nonlinear system, and it can be applied to extract control laws for nonlinear systems. Two methodologies exist for control design (1) hypothesizing a control law and then finding a Lyapunov function to validate the choice, and (2) hypothesizing a Lyapnov function and finding a control law to make it a real Lyapunov function [52]. Prior to presenting the Lyapunov theorem for local and global stabilities, two definitions are given here [52].

Definition 1: A scalar continuous function $V(x)$ is said to be locally positive definite if $V(0) = 0$ and is in a state space neighborhood around the origin, $V(x) > 0$ for $x \neq 0$. If the same holds over the entire state space, then $V(x)$ is said to be globally positive definite.

Definition 2: A scalar continuous function $V(x)$ is said to be locally positive semi-definite if $V(0) = 0$ and is in a state-space region around the origin, $V(x) \geq 0$ for $x \neq 0$. If the same holds over the entire state space, then $V(x)$ is said to be globally positive semi-definite.

if $-V(x)$ is positive definite or semi-definite, then $V(x)$ is negative definite or semi-definite, respectively.

Lyapunov Local Stability Theorem: If a scalar function $V(x)$ with continuous first partial derivatives exists in a state space region around the origin such that

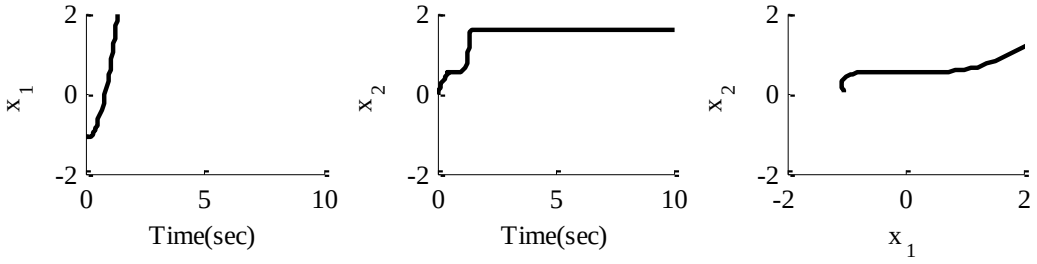

Figure 4.2 State variables and state trajectory of an unstable situation

- $V(x)$ is positive definite
- $\dot{V}(x)$ is negative semi-definite

then the equilibrium point is stable.

For ease of explaining the control theories used in this section, consider a second-order dynamic system of

$$\begin{bmatrix}\dot{x}_1\\ \dot{x}_2\end{bmatrix} = \begin{bmatrix}f_1(x_1, x_2, u_1, u_2)\\ f_2(x_1, x_2, u_1, u_2)\end{bmatrix} \tag{4.2.6}$$

For local stability, the system can be linearized for an operating point ($[x_{10} \quad x_{20}]^T$ and $u_0 = [u_{10} \quad u_{20}]^T$) as

$$\begin{bmatrix}\dot{x}_1\\ \dot{x}_2\end{bmatrix} = \begin{bmatrix}\frac{\partial f_1}{\partial x_1} & \frac{\partial f_1}{\partial x_2}\\ \frac{\partial f_2}{\partial x_1} & \frac{\partial f_2}{\partial x_2}\end{bmatrix}\Bigg|_{\substack{x_0\\u_0}} \begin{bmatrix}x_1\\x_2\end{bmatrix} + \begin{bmatrix}\frac{\partial f_1}{\partial u_1} & \frac{\partial f_1}{\partial u_2}\\ \frac{\partial f_2}{\partial u_1} & \frac{\partial f_2}{\partial u_2}\end{bmatrix}\Bigg|_{\substack{x_0\\u_0}} \begin{bmatrix}u_1\\u_2\end{bmatrix}. \tag{4.2.7}$$

A nonlinear system can be represented by a linear approximation when its dynamic behavior on the operating point is not critical for the far away points. However, this linear approximation cannot always be applied to any system, particularly if f_k is an unknown function. Consider the following nonlinear second-order system

$$\begin{bmatrix}\dot{x}_1\\ \dot{x}_2\end{bmatrix} = \begin{bmatrix}x_1 + 5x_2\\ x_1^4 \cos(x_2) + u\end{bmatrix} \tag{4.2.8}$$

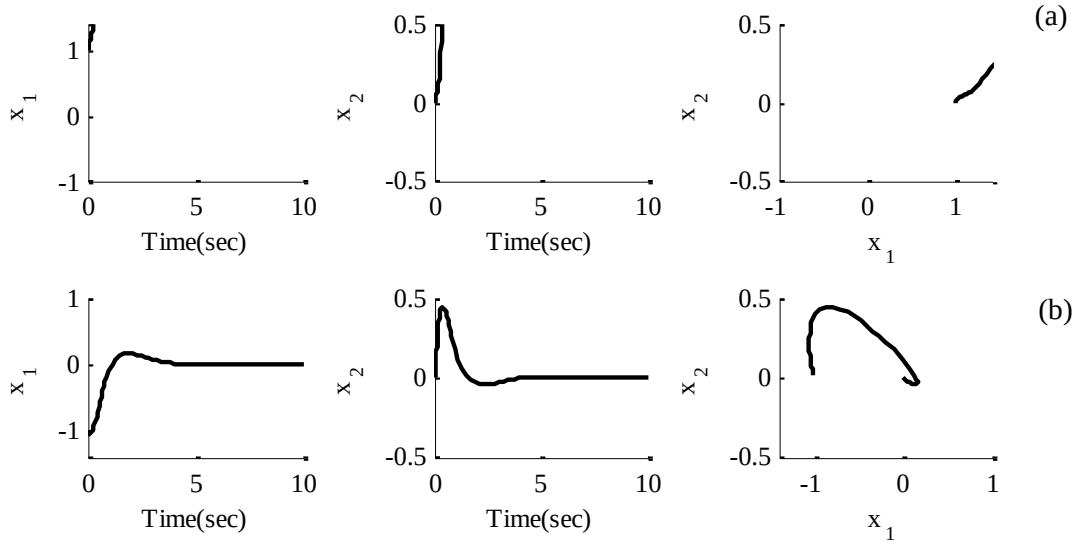

Figure 4.3 State variables and state trajectories after applying a linear controller for two initial conditions: (a) is unstable situation and (b) stable situation

and linearize it around the $(0,0)$ operating point. The linearized system is given by

$$\begin{bmatrix}\dot{x}_1\\ \dot{x}_2\end{bmatrix} = \begin{bmatrix}1 & 5\\ 0 & 0\end{bmatrix}\begin{bmatrix}x_1\\ x_2\end{bmatrix} + \begin{bmatrix}0\\ u\end{bmatrix} \tag{4.2.9}$$

where its eigenvalues are 0 and 1, representing an unstable system at this operating point. Assuming that the input signal is set to be zero and the state variables move to $(-1, 0)$, as shown in Figure 4.2, then x_1 goes to infinity while x_2 settles down to a constant value.

A linear pole placement controller could be designed based on the (Jacobian) linearized system in (4.2.9). The new eigenvalues could be moved to $-1 \mp j$ by choosing the following input signal.

$$u = -x_1 - 3x_2. \tag{4.2.10}$$

This should make the system stable for small disturbances around the origin. In order to show the problem of using the linear control theory in nonlinear systems, two tests with two initial conditions (i.e. $(1,0)$ and $(-1,0)$) were performed, and the results are shown in Figure 4.3. Results

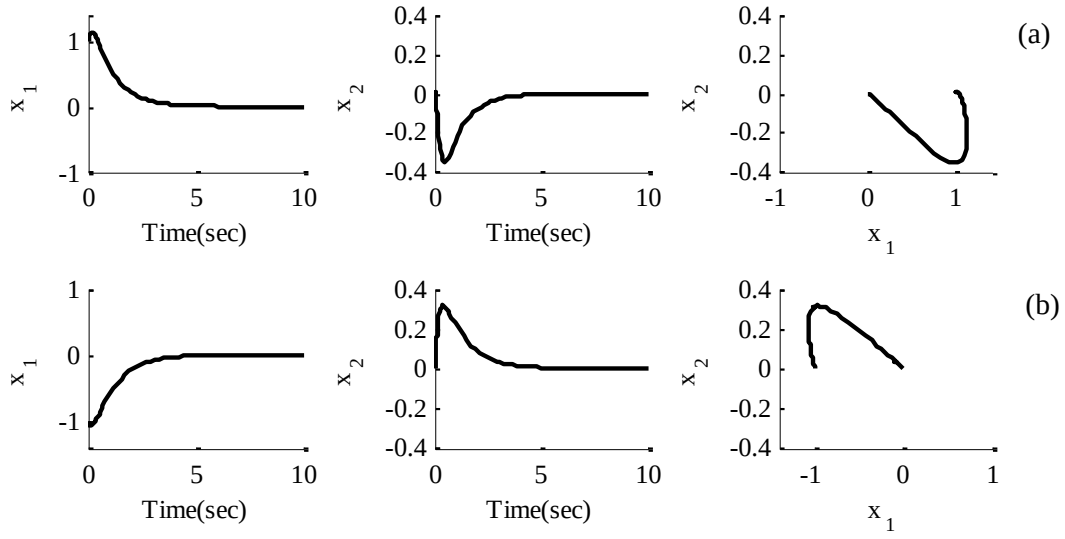

Figure 4.4 Results of the nonlinear control law in (4.2.13) derived from the Lyapunov method.

show that, although distances of these initial points to the origin are identical, one remain stable while the other is unstable.

As mentioned, the Lyapunov method can be used to design a controller. First, a positive definite function should be defined such as $(x) = \frac{1}{2}(x_1 + x_2)^2$, $V(0) = 0$, and $V(x) > 0$ for $x \neq 0$. Then,

$$\dot{V}(x) = (x_1 + x_2)(\dot{x}_1 + \dot{x}_2) \tag{4.2.11}$$

Substituting for $\dot{x}_1$ and $\dot{x}_2$ from (4.2.8) yields

$$\dot{V}(x) = (x_1 + x_2)(x_1 + 5x_2 + x_1^4 \cos(x_2) + u) \tag{4.2.12}$$

The system becomes asymptotically stable if $\dot{V}(x) < 0$ for any $x \neq 0$. This can be achieved by choosing the input signal as

$$u = -x_1^4 \cos(x_2) - 2x_1 - 6x_2 \tag{4.2.13}$$

which makes $\dot{V}(x) = \frac{-1}{2}(x_1 + x_2)^2 < 0$ for any $x \neq 0$. The outcome of the designed nonlinear control law in (4.2.13) is shown in Figure 4.4.

4.2.2 *Feedback Linearization Technique*

A nonlinear controller often offer advantages such as more accuracy, reduced control energy, and faster speed, which explain why the nonlinear control design procedure is more appropriate and challenging. As demonstrated by a comparison of results shown in Figures 4.3 and 4.4. If the nonlinear term (function) is known or can be estimated, the feedback linearization method can be effectively implemented as a nonlinear controller, but the feedback linearization method must be defined [52]. The nonlinear second-order system in (4.2.8) can be used for this definition. The first step is to determinant a nonlinear function of state variables in order to cancel the nonlinear term. That is

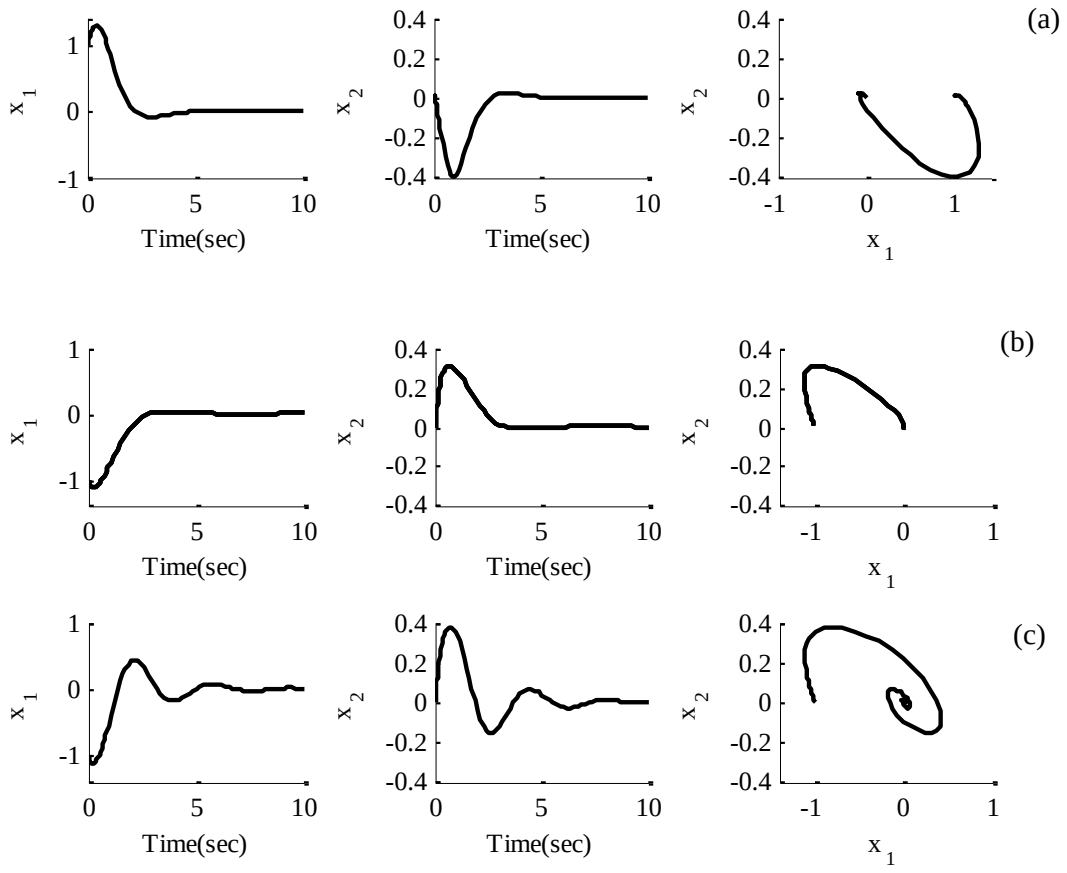

Figure 4.5 Results of the nonlinear control law in (4.2.17) derived from the feedback linearization method

$$u = g(x_1, x_2, u^*) \tag{4.2.14}$$

Substituting u from (4.2.14) into (4.2.8) yields

$$\begin{bmatrix} \dot{x}_1 \\ \dot{x}_2 \end{bmatrix} = \begin{bmatrix} x_1 + 5x_2 \\ x_1^4 \cos(x_2) + g(x_1, x_2, u^*) \end{bmatrix} \tag{4.2.15}$$

As demonstrated if $g(x_1, x_2, u^*) = -x_1^4 \cos(x_2) + u^*$, then (4.2.15) is converted to a linear system

$$\begin{bmatrix} \dot{x}_1 \\ \dot{x}_2 \end{bmatrix} = \begin{bmatrix} x_1 + 5x_2 \\ u^* \end{bmatrix} \tag{4.2.16}$$

which represents a linear dynamic system, and $u^* = -k_1 x_1 - k_2 x_2$ can be used to move the eigenvalues of this converted/virtual linear system. The control law contains two portions: (1) nonlinear term cancellation or feedback linearization inner loop, and (2) pole placement outer loop, as given below:

$$u = -x_1^4 \cos(x_2) - k_1 x_1 - k_2 x_2 \tag{4.2.17}$$

Figure 4.5 shows simulation results of the case study that implemented a control scheme based on the developed feedback linearization method, in which k_1 and k_2 for the first two cases are selected to be 1 and 3, respectively, whereas these coefficients are 1 and 2 for the third case, shown in the third row.

4.3 Proposed Method for Extremum Power Seeking

In the proposed technique, three control loops/laws are implemented to (*i*) determine the desired electrical/generator torque, T_e^*, in the DFIG, as shown in Figure 4.6, (*ii*) estimate the wind turbine power capture coefficient, $\hat{C}_P$, and (*iii*) calculate the desired rotor speed, ω_R^*, at which the wind turbine captures the maximum available wind power, as shown in Figure 4.7. These control laws are described in the following subsections.

4.3.1 *Feedback Linearization for Torque Control*

As explained in the previous section, feedback linearization implements a feedback loop in order to transform the nonlinear system into an equivalent linear system by changing the control input signal. As discussed in Chapter 2, aerodynamic or mechanical torque is the nonlinear term of the equation of motion in wind turbines. If the aerodynamic torque can be estimated then the nonlinearity of the equation of motion can be approximately cancelled using the control law

$$T_e^* = \hat{C}_p f(v, \omega_R) - u(t) \tag{4.3.1}$$

where $\hat{C}_p$ is the estimated value of the power capture coefficient and $f(v, \omega_R) = (\rho A v^3 / 2\omega_R) \propto \omega_R^2$ as defined in Chapter 2. The strategy is to make T_e follows the desired value, T_e^*, resulting in a linear input-output dynamic behavior for the equation of motion (i.e., $J\dot{\omega}_R + C_D\omega_R = u(t)$). Therefore, the key is to estimate the power coefficient, as explained in the next subsection.

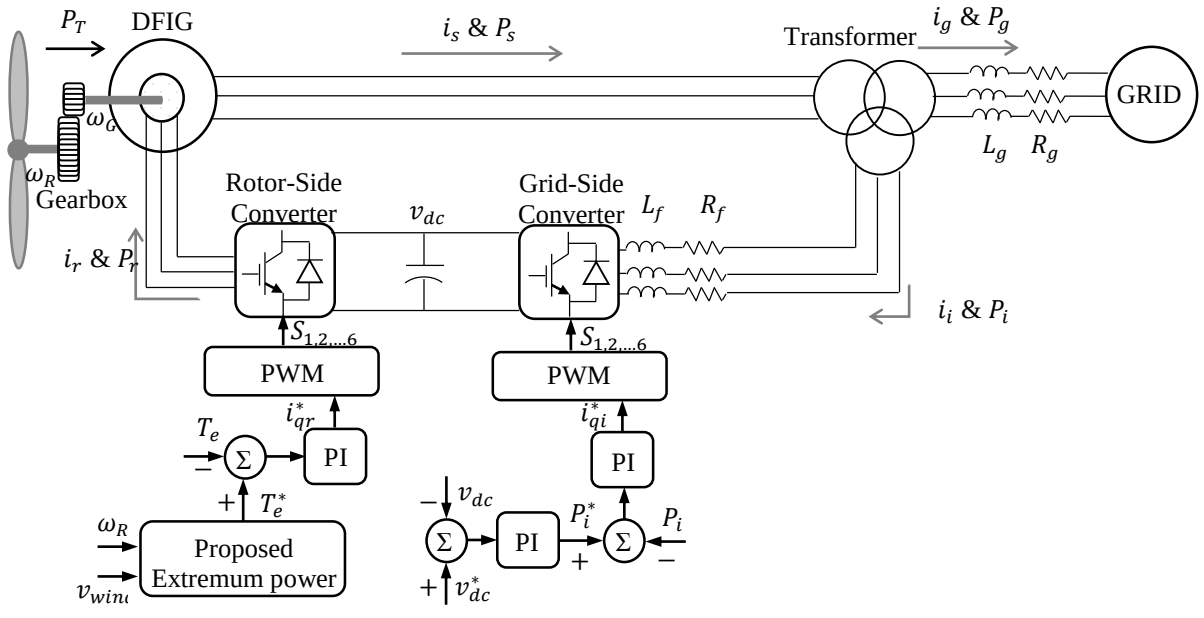

Figure 4.6 Schematic of a DFIG based wind turbine system.

4.3.2 *Lyapunov Approach for Power Capture Coefficient Estimation*

Estimation of the power capture coefficient, C_p, is used herein for maximizing power capturing. From the equation

$$C_p = \frac{P_T}{P_{avail}} = \frac{P_T}{(1/2)\rho A v^3} \tag{4.3.2}$$

where parameters are defined in Chapter 2, the C_p value can be calculated using rotor power or torque measurements; however, the torque measurement requires an additional sensor. Therefore, the common approach is to estimate the torque indirectly via the generator power measurement. In this work, the estimation of C_p is achieved using a Lyapunov-based method. The candidate Lyapunov function, V, is chosen as

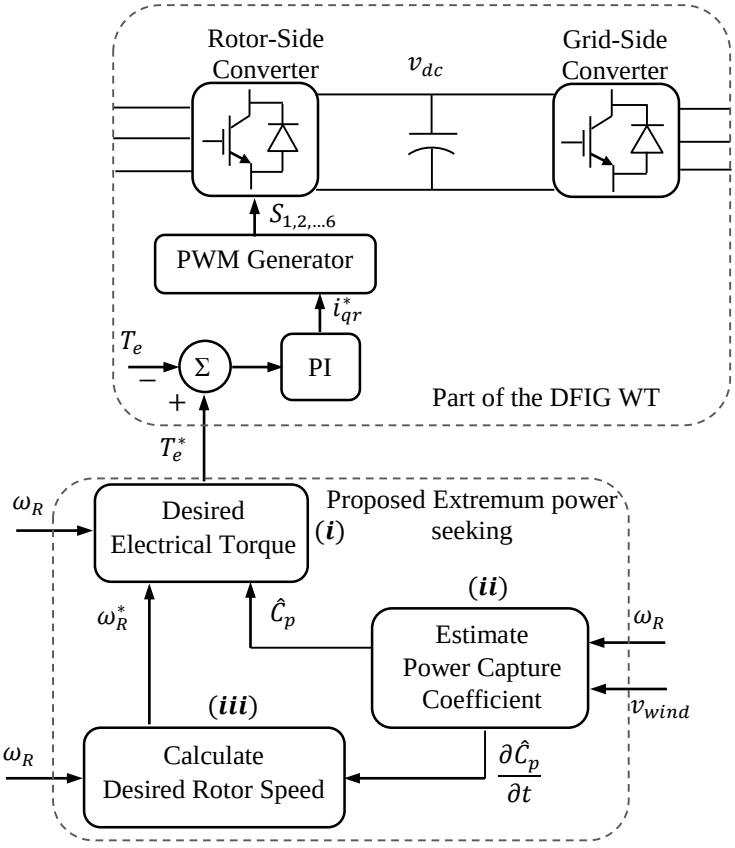

Figure 4.7 Block diagram of the proposed control scheme for extremum power seeking in DFIG-based wind turbines, including (*i*) the desired electrical torque calculator, (*ii*) wind turbine power capture coefficient, $\hat{C}_p$, estimator, and (*iii*) a desired rotor speed, ω_R^*, calculator

$$V = \frac{1}{2}J\tilde{\omega}_R^2 + \frac{1}{2}\gamma\tilde{C}_p^2 \tag{4.3.3}$$

where γ is a constant to be determined, $\tilde{\omega}_R = \omega_R^* - \omega_R$, and $\tilde{C}_p = C_p^* - \hat{C}_p \geq 0$, in which C_p^* is is the maximum value of C_p. Computing the time derivative of (4.3.3) yields

$$\dot{V} = J\tilde{\omega}_R\dot{\tilde{\omega}}_R + \gamma\tilde{C}_p\dot{\tilde{C}}_p. \tag{4.3.4}$$

Applying $\dot{\tilde{\omega}}_R = \dot{\omega}_R^* - \dot{\omega}_R$ and $\dot{\tilde{C}}_P = \dot{C}_p^* - \dot{\hat{C}}_p$ yields

$$\dot{V} = J\tilde{\omega}_R(\dot{\omega}_R^* - \dot{\omega}_R) + \gamma\tilde{C}_p\left(\dot{C}_p^* - \dot{\hat{C}}_p\right). \tag{4.3.5}$$

Neglecting the viscous damping torque, $C_D\omega_R$, of the overall system, and then substituting $\dot{\omega}_R$ from the equation of motion yields

$$\dot{V} = J\tilde{\omega}_R\left(\dot{\omega}_R^* - \frac{1}{J}(T_{aero} - T_e)\right) - \gamma\tilde{C}_p - (\dot{C}_p^* - \dot{\hat{C}}_p) \tag{4.3.6}$$

which can be simplified as

$$\dot{V} = J\tilde{\omega}_R\dot{\omega}_R^* - \tilde{\omega}_R\left(C_pf - \hat{C}_pf + u\right) - \gamma\tilde{C}_p(\dot{C}_p^* - \dot{\hat{C}}_p) \tag{4.3.7}$$

C_p^* is chosen to be Betz constant; therefore, (4.3.7) can be rewritten as

$$\dot{V} = J\tilde{\omega}_R\dot{\omega}_R^* - \tilde{\omega}_R\left(C_pf - \hat{C}_pf + u\right) + \gamma\tilde{C}_p\dot{\hat{C}}_p \tag{4.3.8}$$

Substituting for $\tilde{C}_p$ into (4.3.8), yields

$$\dot{V} = J\tilde{\omega}_R\dot{\omega}_R^* - \tilde{\omega}_R\left(C_pf - \hat{C}_pf + u\right) - \gamma\dot{\hat{C}}_p\left(C_p^* - \hat{C}_p\right) \tag{4.3.9}$$

This last result can be rewritten as

$$\dot{V} = \hat{C}_p\left(\tilde{\omega}_Rf + \gamma\dot{\hat{C}}_p\right) - \tilde{\omega}_Ru + J\tilde{\omega}_R\dot{\omega}_R^* - C_pf\tilde{\omega}_R - \gamma C_p^*\dot{\hat{C}}_p \tag{4.3.10}$$

The strategy is to make $\dot{V}$ a non-positive quantity. The first term in (4.3.10) is chosen to be zero, that is,

$$\hat{C}_p\left(\tilde{\omega}_Rf + \gamma\dot{\hat{C}}_p\right) = 0. \tag{4.3.11}$$

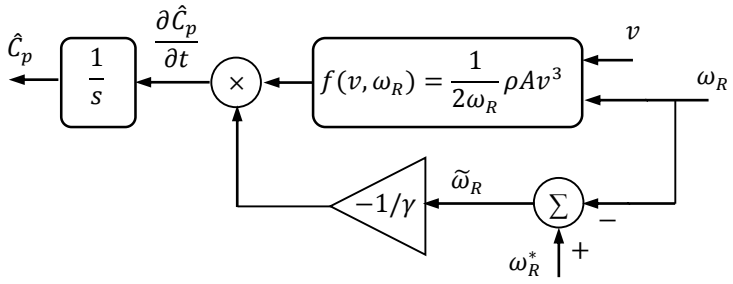

Figure 4.8 Estimation of wind turbine power coefficient, $\hat{C}_p$, value in the control scheme

Therefore, the derivative of the Lyapunov function, i.e. (4.3.10), is simplified as

$$\dot{V} = -\widetilde{\omega}_R u + J\widetilde{\omega}_R \dot{\omega}_R^* - C_p f \widetilde{\omega}_R - \gamma C_p^* \dot{\hat{C}}_p. \tag{4.3.12}$$

Herein, $\hat{C}_p$ in (4.3.11) is not always equal to zero; therefore, the term in the parenthesis must be zero, resulting in the following differential equation

$$\dot{\hat{C}}_p = -\frac{1}{\gamma}\widetilde{\omega}_R f(v,\omega_R), \tag{4.3.13}$$

the solution of which provides the estimated power capture coefficient (Figure 4.8). In order to keep the second term on the right in (4.3.10) a non-positive value, the control input can be chosen as $u(t) = k_p\widetilde{\omega}_R$. Therefore, the main control law in (4.3.1) can be rewritten as

$$T_e^* = -\frac{1}{\gamma} f(v,\omega_R) \int \widetilde{\omega}_R f(v,\omega_R) dt - k_p \widetilde{\omega}_R. \tag{4.3.14}$$

The torque control scheme including the feedback linearization loop and the power capture coefficient estimation is shown in Figure 4.9. The result in (4.3.14) can be written as an adaptive PI controller:

$$T_e^* = -k_{I1}(t) \int \widetilde{\omega}_R k_{I2}(t) dt - k_p \widetilde{\omega}_R \tag{4.3.15}$$

where $k_{I1}(t)$ and $k_{I2}(t)$ are time-varying parameters.

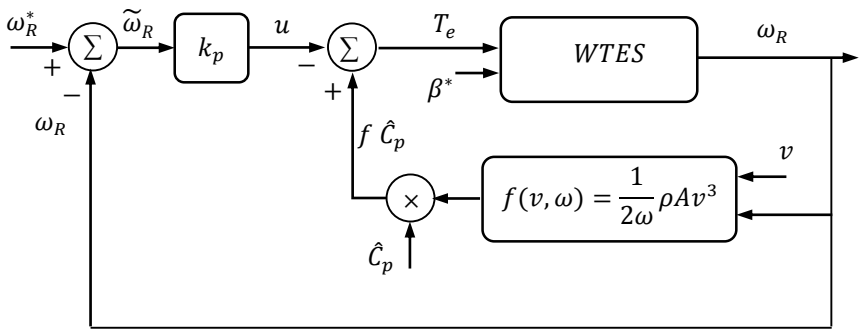

Figure 4.9 Feedback linearization technique for rotor speed control in wind turbine systems

4.3.3 *Extremum Power Seeking Strategy*

The maximum-seeking law can also be extracted from the Lyapunov function. Substitution of $u(t) = k_p\widetilde{\omega}_R$ and $\dot{\hat{C}}_p$ from (4.3.13) in (4.3.12) to obtain

$$\dot{V} = -k_p\widetilde{\omega}_R^2 + J\widetilde{\omega}_R\dot{\omega}_R^* + \left(C_p^* - C_p\right)\widetilde{\omega}_R f. \tag{4.3.16}$$

In the following, $\dot{\omega}_R^*$ is identified to ensure that (4.3.16) is always a non-positive value. In order to hold $\dot{V} \leq 0$ in (4.3.16), one can choose $\dot{\omega}_R^* \propto (-\widetilde{\omega}_R)$ and select k_p adequately large that the first term holds a sufficiently large negative value with respect to the third term in (4.3.16), as shown in the results demonstrated in Section 4.6. Because $\dot{\hat{C}}_p \propto (-\widetilde{\omega}_R)$, and by choosing $\dot{\omega}_R^* \propto (-\widetilde{\omega}_R)$, the desired rotor speed can be formulated as

$$\dot{\omega}_R^* = k\dot{\hat{C}}_p \tag{4.3.17}$$

This is consistent with the fact that the maximum value of $C_p = P_T/P_{avail}$ and captured power, P_T, for a constant wind speed occurs at the same point at which $\partial P_T/\partial\omega_R = 0$, as shown in Chapter 2. In the hill-climbing and perturb-and-observe techniques, maximum power is sought according to the sign of $\partial P_T/\partial\omega_R$ such that if the wind turbine operating point is on the left side of the maximum point of the power curve, the desired rotor speed must be increased; if it is on the right side of the maximum point, then the rotor speed must be decreased. The forgoing discussion is

valid for a constant or a slowly varying wind speed case. However, if the wind speed suddenly changes, two scenarios are possible:

wind speed increases thus, $\dot{\omega}_R > 0$ and $\dot{P}_T > 0$, or

wind speed decreases thus, $\dot{\omega}_R < 0$ and $\dot{P}_T < 0$.

Using the chain rule, the conclusion can be made that for both scenarios $(\partial P_T/\partial \omega_R) > 0$ meaning that the hill-climbing and perturb-and-observe techniques can fail in the case of a sudden wind speed change [11]. The same argument is true if the sign of $\partial C_p/\partial \omega_R$ is used. Although C_p is not available, $\hat{C}_P$ and its derivative are available from the control scheme shown in Figure 4.8. However, in order to prevent a mistake in extremum power seeking due to a sudden wind speed change, and according to (4.3.15), the proposed formula for $\dot{\omega}_R^*$ is given as

$$\dot{\omega}_R^* = k_e \frac{\partial \hat{C}_P/\partial t}{|\partial \omega_R/\partial t|} \tag{4.3.18}$$

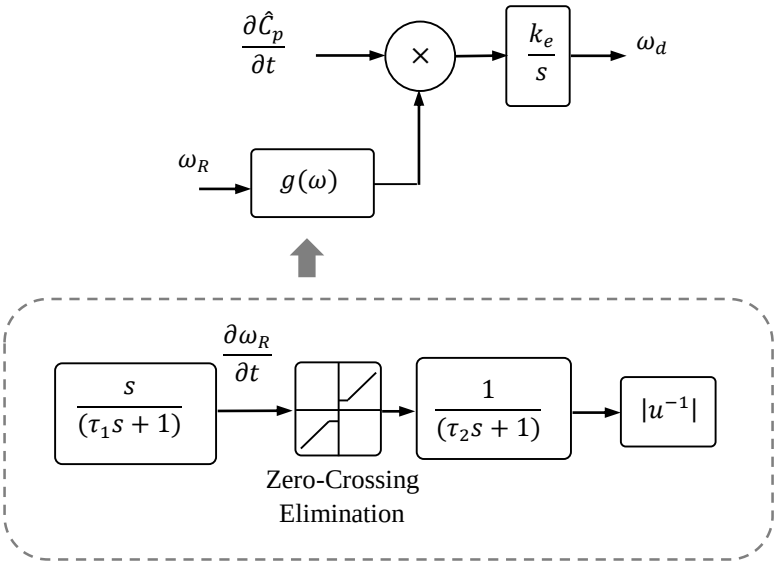

Figure 4.10 Desired rotor speed, ω_R^* , in the control scheme

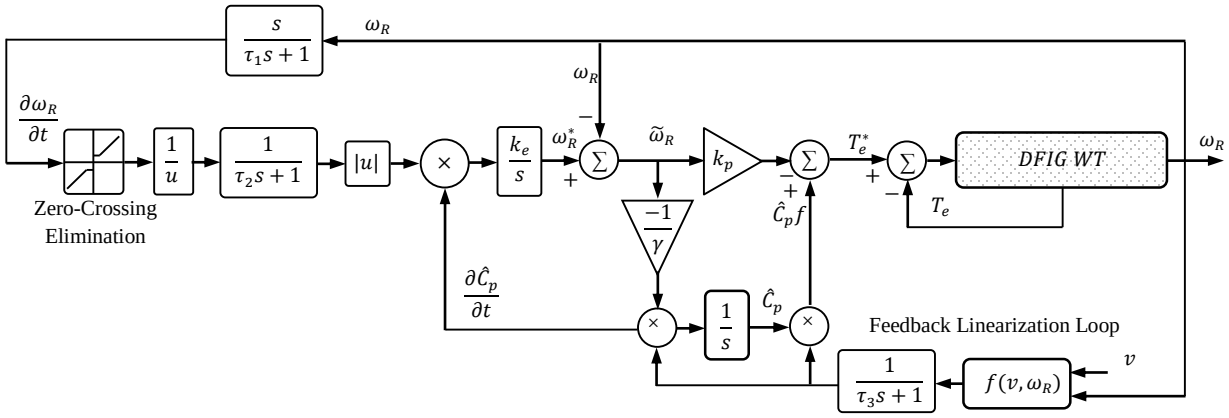

Figure 4.11 Detailed control loops of the proposed extremum power seeking block

where the denominator adaptively controls the rate of change in the desired rotor speed such that the gain in (4.3.18) is inversely updated based on rotor acceleration. In practice, a zero-crossing elimination for the $|\partial\omega_R/\partial t|$ calculation is needed to prevent any potential numerical problem, as shown in Figure 4.10. In this figure, the first transfer function is designed to obtain the time derivative of the angular speed ω_R. Accordingly, τ_1 and τ_2 are chosen such that slow dynamics of the mechanical system can be observed, while measurement noise and spikes due to numerical calculation are effectively filtered. The values of k_e and τ_2 play important roles in the extremum power seeking control scheme, when the wind speed suddenly increases or decreases.

The proposed technique captures maximum power without the dither/perturbation signal and it does not fail in the case of a sudden change in wind speed. The three control loops of the proposed extremum seeking are demonstrated in Figure 4.11. The wind speed profile must be sufficiently rich, as defined in [53], in order to achieve optimum results. Also, the experience gained in tuning the control system demonstrated that the constant k_e in (4.3.16) and the constant γ in (4.3.12) have the greatest influence in achieving the power capture peak by either slowing or hastening attainment of the proper value of ω_R^* for a given wind speed. The constant γ can be chosen as a value below the wind turbine inertia.

4.4 Sensitivity Analysis of Control Parameters

In this section, sensitivity of the proposed control scheme for extremum power seeking is studied in terms of variations of two main control parameters for various wind speeds. For this study, the two main control parameters in (4.3.13) (i.e., k_p and γ) were changed within their acceptable limits and the power capture coefficient, C_p, was measured for the 5MW wind turbine. For variations of γ and k_p, the outcomes of this study are shown in Figure 4.12 (a) and (b), respectively. In Figure 4.12 (a), C_p varies between 0.4829 and 0.4059 for a wide range of γ and three wind speeds ($v = 7$, 8, and 9 m/s) in Region 2. Also, in Figure 4.12 (b), C_p varies between 0.4840 and 0.4563 for the wind speed and various k_p values. As shown, the control scheme is more sensitive to γ than k_p. Also, C_p remains above the acceptable value of 0.477, and values of $\partial C_p/\partial\gamma$ and $\partial C_p/\partial k_p$ are insignificant for $10^6 \leq \gamma \leq 10^7$ and $10^5 \leq k_p \leq 10^6$, respectively. In

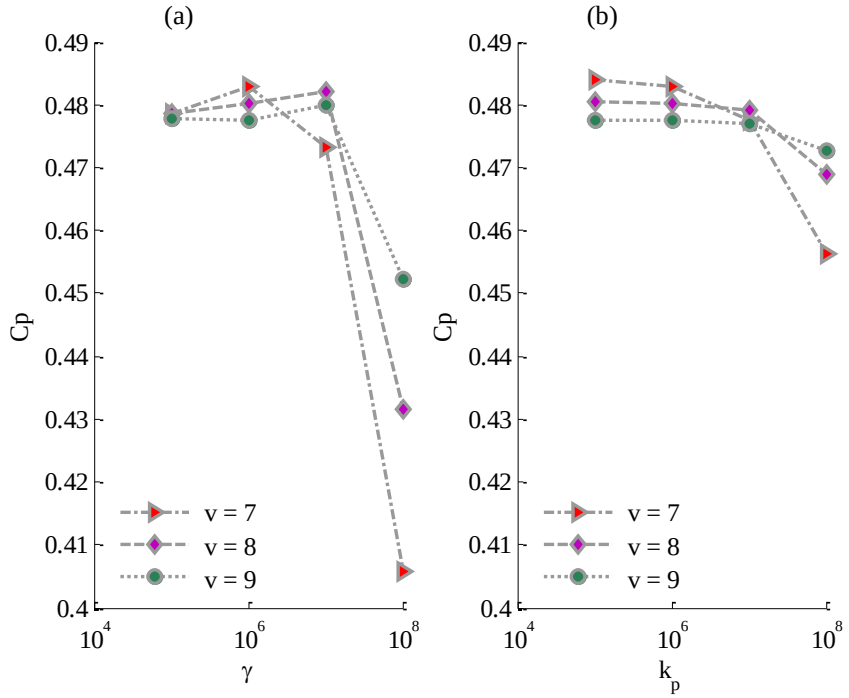

Figure 4.12 The control scheme sensitivity to control parameters for three different wind speed values, plot of (a) C_p versus γ for $k_p = 10^6$, and (b) $C_p$versus k_p for $\gamma = 10^6$.

addition to results shown in the previous section for various wind speed profiles, these plots confirm that extremum power seeking can successfully be achieved over relatively wide ranges of the control parameters, but optimum results occur at $\gamma \cong 2 \times 10^6$ and $k_p = 0.1 \times 10^6$.

4.5 Transition between Region 2 and Region 3

A technical challenge for any extremum power seeking scheme for wind turbines is to provide seamless transitions between Regions 2 and 3. For this study, extremum power seeking is only performed in Region 2 and the blade pitch control is activated to maintain rotor speed and power at their rated values in Region 3. The control strategy in Region 3 is to regulate generator torque at its maximum value (i.e., $P_{rated}/\omega_{R\,max}$) at the low-speed shaft. Consequently, as wind speed increases in Region 3, the accelerating torque (i.e., $T_{aero} - T_e$) increases, and thus, the rotor speed increases. However, an increase in blade pitch angle can reduce T_{aero} . Therefore, rotor speed can be controlled at its rated value (i.e., $\omega_{R\,max}$) and the output power remains at its rated value. Moreover, for a seamless transition between regions in the proposed control scheme, f in (4.3.11) can be herein defined as

$$f = \begin{cases} \dfrac{1}{2}\dfrac{\rho A v^3}{\omega_{R\,min}}, & 0 \le \omega_R < \omega_{R\,min} \quad Region\ 1 \\ \dfrac{1}{2}\dfrac{\rho A v^3}{\omega_R}, & \omega_{R\,min} \le \omega_R < \omega_{R\,max} \quad Region\ 2 \\ \dfrac{P_{rated}}{\omega_{R\,max} C_{p\,max}}, & \omega_R \ge \omega_{R\,max} \quad Region\ 3 \end{cases} \tag{4.5.1}$$

where $\omega_{R\,min}$ and $\omega_{R\,max}$ are the rated minimum and maximum rotor speed values, respectively. Also, a region called Region 2.5 can be implemented into the proposed scheme to further smooth the transition between Regions 2 and 3. The calculated f should be passed through a first-order low-pass filter to avoid any sudden change in (4.5.1) caused by wind speed variations or transitions

between regions. In the proposed controller, a compensator torque command signal is fed to the generator to suppress rotor speed overshoot during the transition from Region 2 to 3.

4.6 Simulation Verifications and Analysis of Results

In order to investigate performance of the proposed control scheme, the system shown in Figure 4.11 has been modeled in the MATLAB/Simulink environment. The model consists of the NREL 5 MW reference turbine simulator connected to a DFIG through a gearbox with a 1:97 gear ratio, as well as power converters and a transmission line. Electrical parameters are given in Table 4.1. The control system was also developed in the Matlab/Simulink environment, and control parameters are given in Table 4.2.

Two wind speed profiles, sudden wind speed step changes and wind turbulence in the Region 2 of the 5MW wind turbine were used to investigate the validity of the proposed technique and results are presented in this section. In the tests, control parameters, γ and k_p, were set to be equal to 2×10^6 and 0.1×10^6, respectively, and k_e was defined as a function of the wind speed in Region 2. However, a much larger value for k_e, such as $k_e = 1$, was used in Region 1(i.e., when $v < 5$ m/sec or $\omega_R < 7.2$ rad/sec) for the 5MW wind turbine. In the first case study, wind speed is set to contain two step changes. The first step change is from 8 m/sec to 7 m/sec at $t = 800$ sec, the second step change is from 7 m/sec to 9 m/sec at $t = 1400$ sec. Figures. 4.13(a)-(d) show the wind speed, desired and actual rotor speed, aerodynamic and desired electrical torque, and the actual and estimated power capture coefficient, respectively. Figure 4.13(b) shows that the actual rotor speed closely follows the desired rotor speed that is calculated from the extremum seeking control scheme given in (4.3.15). The speed regulation is such that it is difficult to discern any difference between the desired rotor speed and the actual rotor speed. Figure 4.13(c) shows that the aerodynamic torque also follows the control torque obtained from (4.3.13). As shown in Figure

4.13 (d), the actual power capture coefficient (calculated from the FAST wind turbine simulator output data) and the estimated $\hat{C}_P$ reside near the maximum value of 0.48 for the 5MW wind turbine. The desired rotor speed is adjusted in response to wind speed step changes in order to retain the maximum power capture coefficient. Figure 4.14 (a)-(d) show the aerodynamic and grid power, DC bus voltage, Lyapunov function, and time derivative of the the Lyapunov function, respectively. Figure 4.14 (a) shows that the aerodynamic power follows the power obtained from the grid. Figure 4.14 (b) shows that although no protection exists in the system, the DC bus voltage remained nearly constant due to control from the grid-side converter. Figures 4.14 (c) and (d) show the stability of the system since the Lyapunov function is a positive definite and its derivative is negative semi-definite.

In the second case, the system response to real wind turbulence occurring between $t = 700$ sec and $t = 1650$ sec was investigated. For $0 < t < 700$ and $t > 1650$, the average wind speed value was set to 9 m/sec. Figure 4.15 (a) illustrates the wind speed profile, and Figure 4.15 (b) shows the desired rotor speed and its actual value. As shown, rotor speed follows the desired speed. The desired rotor speed, ω_R^*, in Figures 4.13 and 4.15 is controlled to track maximum available power, and the actual rotor speed closely follows it during wind speed turbulence. Figure 4.15 (c) shows the aerodynamic torque and the control law torque given by (4.3.13) for this case study. As shown, the generator torque follows the aerodynamic torque. According to results shown in Figures 4.13 and 4.15, the calculated desired speed is adjusted automatically to keep $\hat{C}_P$ at its maximum value, or 0.48 p.u. Thus, the desired rotor speed changes and tracks the desired value. In addition, the controller works in various wind speed conditions, thereby maintaining the estimated power capture coefficient at its maximum value even in the event of sudden step changes and turbulence in the wind speed. The estimated power capture coefficients in Figures 4.14 (d) and

4.15 (d) show that, regardless of wind speed profiles, the estimated power coefficient attempts to stay near the extremum value.

Figures 4.16 (a)- (d), show aerodynamic and grid power, DC bus voltage, Lyapunov function, and the derivative of the Lyapunov function, respectively. Figure 4.16 (a) shows that the aerodynamic power follows the power obtained from grid. Again, Figure 4.16 (b) shows that although no protection existed in the system, the DC bus voltage remained nearly constant due to control by the grid-side converter. Figures. 4.16 (c) and (d) show stability of the system since the Lyapunov function is a positive definite and its derivative is negative semi-definite.

Table 4.1 DFIG-based wind turbine electrical part parameters

Parameter	Value	Unit
Generator No. of Poles, p	6	--
Generator Stator Rated Voltage	3.75	kV
Stator Resistance, R_s	30.7	mΩ
Rotor Resistance, R_r	40.3	mΩ
Stator Leakage Inductance, L_{ls}	0.49	mH
Rotor Leakage Inductance, L_{lr}	0.59	mH
Magnetizing Inductance, L_M	44.5	mH
DC-bus Rated Voltage	4.00	kV
DC-bus Capacitor, C	8000	μF
Converter Filter Resistance, R_f	10	mΩ
Converter Filter Inductance, L_f	0.5	mH
Transformer Ratio	1:10	--
Transmission Line Resistance, R_g	10	mΩ
Transmission Line Inductance, L_g	100	mH

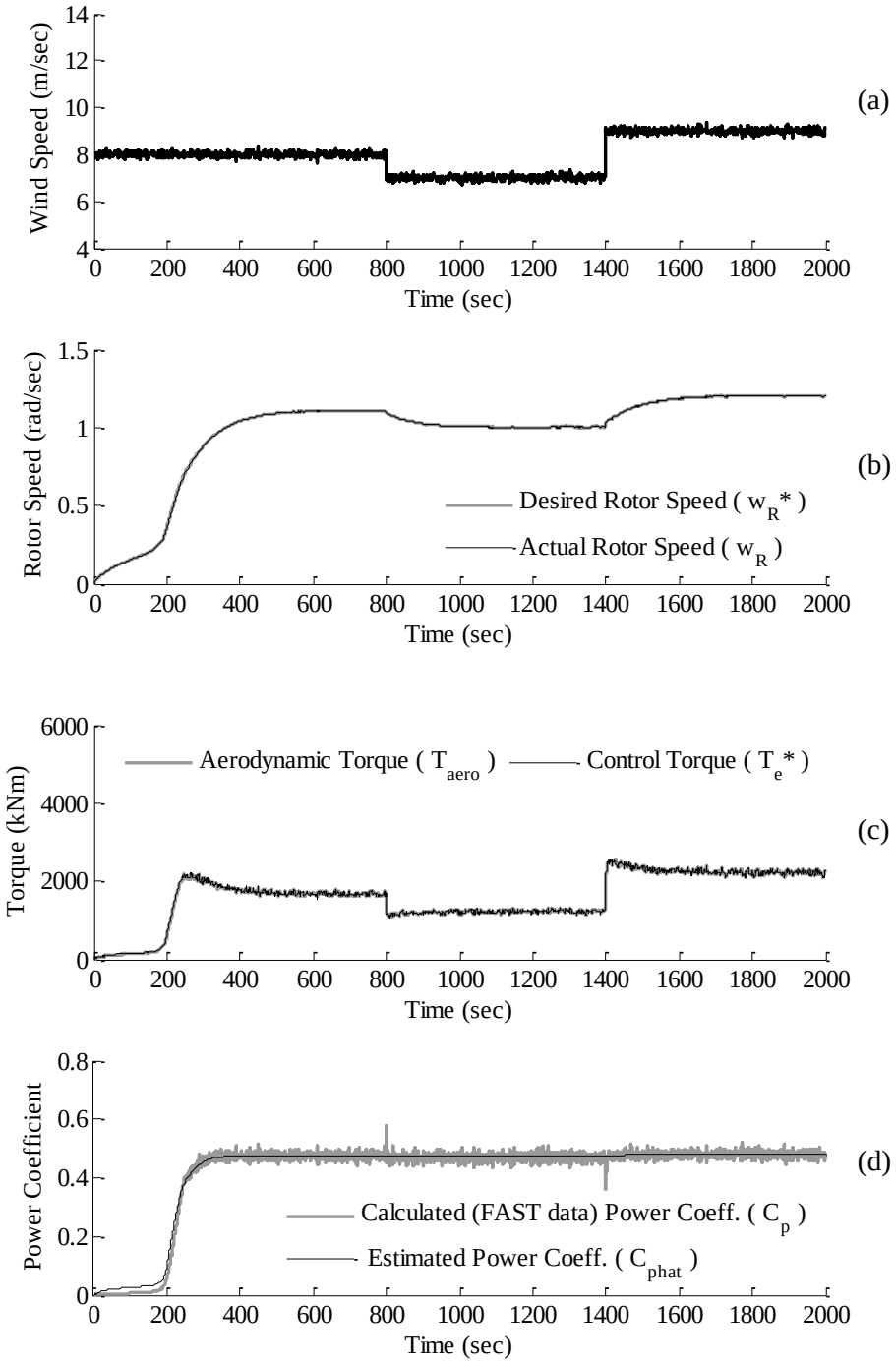

Figure 4.13 System response to wind speed changes: (a) wind speed in m/sec (b) actual, ω_R, and desired, ω_R^*, rotor speed in rad/sec, (c) aerodynamic torque and control torque in kNm, and (d) actual and estimated power coefficient— $\hat{C}_p$ reaching its extremum value

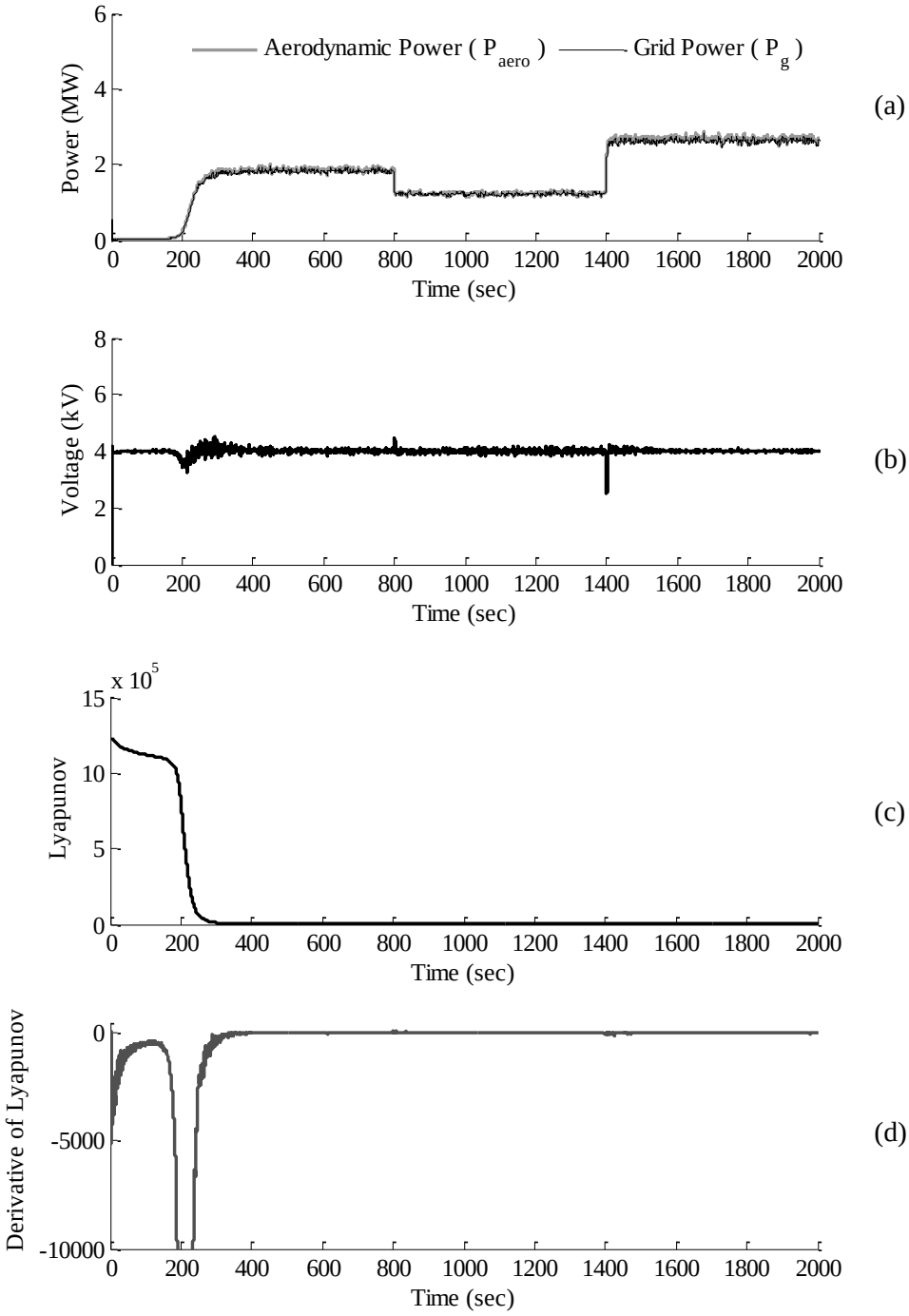

Figure 4.14 System response to wind speed changes (a) aerodynamic and grid power P_{aero}, P_g (b) DC- bus voltage v_{DC}, (c) Lyapunov function, V, and (d) derivative of Lyapunov function, $\dot{V}$

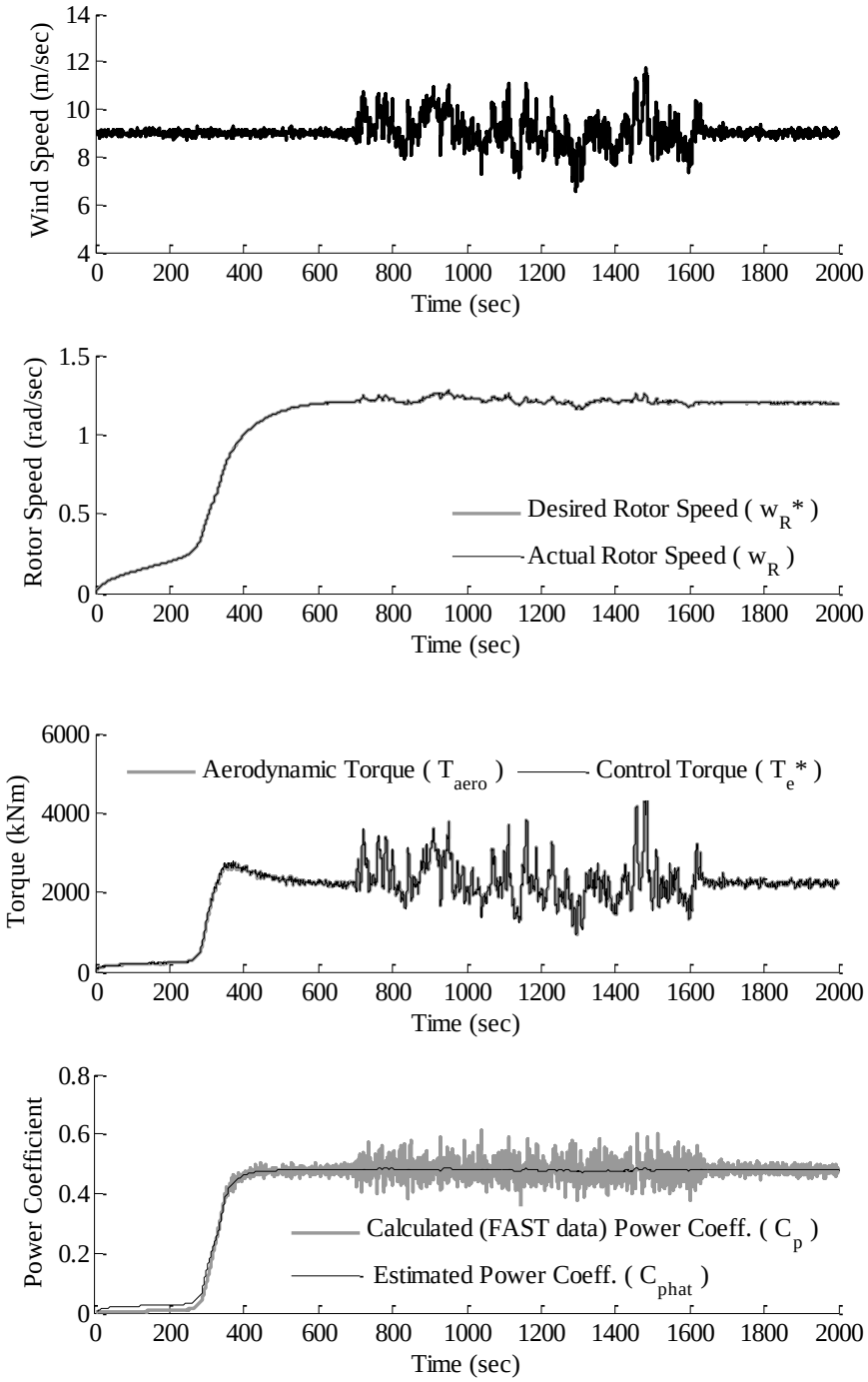

Figure 4.15 System response to wind speed turbulence occurring between t =700 and 1650 sec, (a) wind speed profile in m/sec, (b) actual and desired rotor speed in rad/sec, (c) Aerodynamic torque and control torque in kNm, and (d) actual and estimated power coefficient, $\hat{C}_p$, holds its extremum value

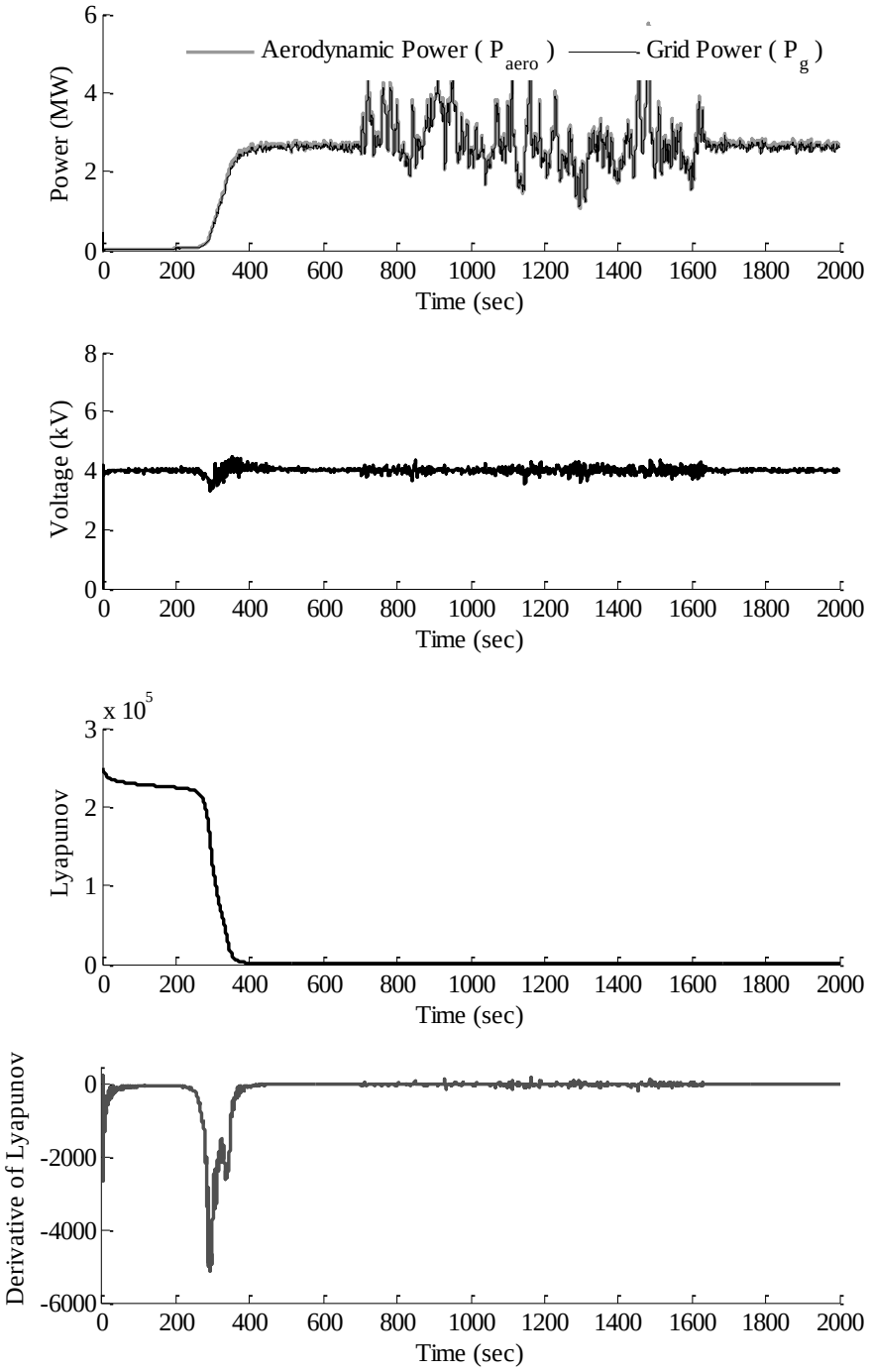

Figure 4.16 System response to wind speed turbulence occurring between t =700 and 1650 sec, (a) aerodynamic and grid power, (b) DC bus voltage, (c) Lyapunov function, (d) derivative of Lyapunov function

Table 4.2 Control parameters for the extremum power seeking technique

Parameter	Value	Unit
Coefficient (k_p)	10^5 – 10^6	--
Coefficient (γ)	10^6 – 10^7	--
Time Constant (τ_1)	0.1	sec
Time Constant (τ_2)	4	sec
Time Constant (τ_3)	2	sec
Coefficient (k_e)	$0.002 - 0.02$	--

4.7 Comparison between $k\omega^2$ and the Proposed Control Scheme

A comparison between the desired (control) torque equation in the conventional method (i.e., $T_e^* = k_{opt}\omega^2$) and in the proposed method, (4.1.1), substituting $v = \omega_R R/\lambda_{opt}$ highlighted the similarity between the two methods. Despite the disadvantages of the conventional method mentioned in the literature, e.g., in [8] , [9], and [10], the ease of implementation is the key advantage. However, dynamic behaviors of the two methods are different as three control parameters, k_e, γ and k_p, exist in the proposed method. This can provide the flexibility to obtain maximum C_p, while the rotor speed variation is less than that of $k\omega_R^2$ at the event of a sudden change in wind speed. The small variation in rotor speed results in less mechanical stresses on drivetrain parts such as the gearbox, shaft, and blades, consequently extending the life of the wind turbine. In order to demonstrate this difference, results obtained from both methods are compared in Figure 4.17, in which k_{opt} is set to 1.8×10^6 for the case study of the 5MW DFIG-based wind turbine in order to obtain $C_p = 0.48$. Power capture, rotor speed, and mechanical torque are shown in Figure. 4.17. The only difference between the simulated systems was the controller or command

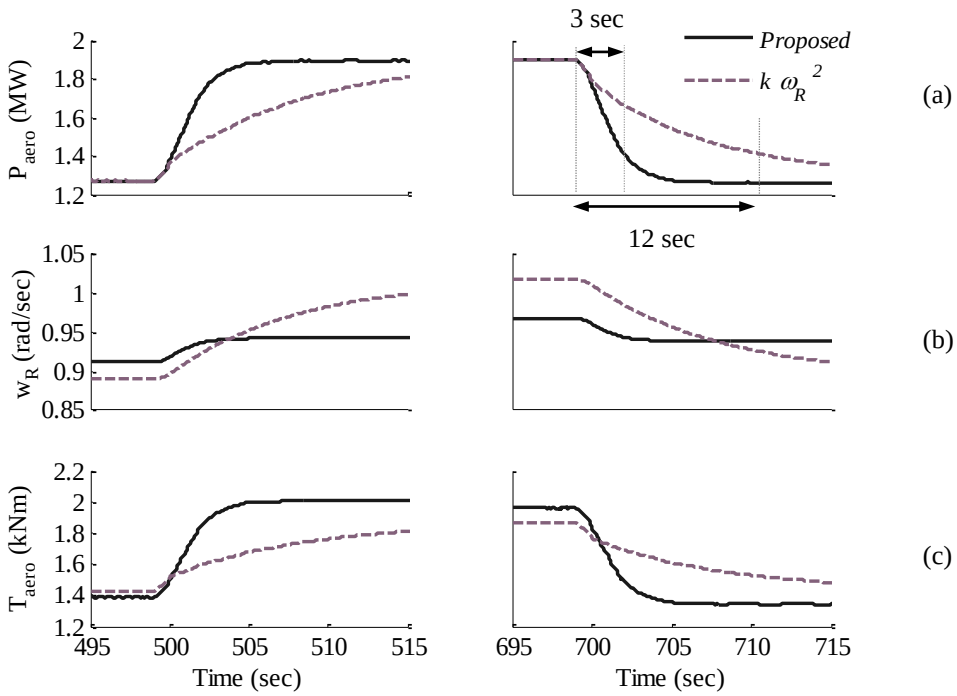

Figure 4.17 System responses (solid-lines indicate he results of the proposed method and dashed-lines indicate results of the conventional method) to two step changes in wind speed profile (7 - 8 m/sec at t=499sec, and 8 -7 m/sec at t=699 sec) (a) Rotor speed in rad/sec (b) mechanical (aerodynamic) torque in kNm, and (c) power injected to the power grid in MW

torque signal, T_e^*. In the figure, wind speed demonstrates a step change at $t = 499\ sec$ from 7 to $8\ m/s$ and then back to 7 at $t = 699\ sec$. The rise-time response of power in the proposed technique is approximately 3 sec whereas in the conventional method, the rise-time is approximately 12 sec, as shown in Figure. 4.17. A comparison between these figures demonstrates that the dynamic response of the proposed controller is faster than the conventional, $k\omega^2$, controller, but the rotor speed variation due to a step change in wind speed is small for the proposed controller.

Chapter 5 – Mitigation of Torsional Vibrations in Wind Turbines

A nonlinear control scheme for the mitigation of torsional vibrations in the drivetrain of wind turbines is presented in this chapter. The mitigation is achieved by superimposing a compensation torque at specific natural frequencies of the drivetrain to the maximum power seeking torque through the generator and generator-side converter. The developed technique uniquely applies the nonlinear sliding mode control theory to mitigate torsional vibrations in wind turbines. The chapter begins with the background of vibration mitigation techniques, then eigenvalues of a 750kW wind turbine are identified using the discussion presented in Chapter 2. The sliding mode theory for controlling the stability of nonlinear systems is studied using the same example presented in Chapter 4. The sliding mode theory is then applied for mitigation of torsional vibrations in wind turbines. At the end of the chapter, the developed scheme is verified in DFIG-based and PMG-based wind turbine systems with mechanical and electrical disturbances.

5.1 Background of Torsional Vibration Mitigation Techniques

One major technical challenge associated with wind turbines is the mitigation of torsional vibrations caused by interaction between the wind turbine drivetrain and the power grid due to electrical or mechanical events, as shown in Figure 5.1.

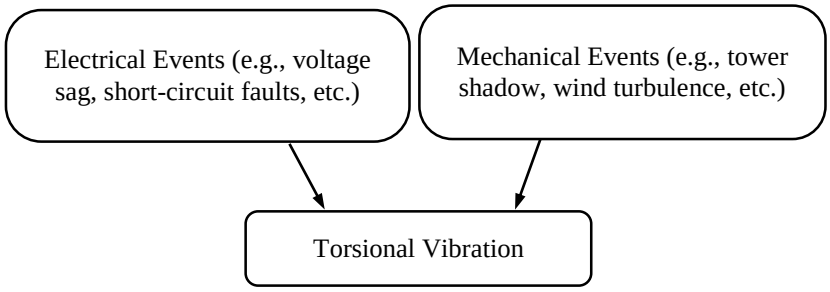

Figure 5.1 Main causes of torsional vibrations in wind turbines

Torsional vibrations in the wind turbine drivetrain reduce the gearbox lifespan and increase wind turbine maintenance cost [54]. The use of a series capacitor in transmission lines can lead to potential sub-synchronous resonance between the wind turbine drivetrain and the transmission line. Rapid changes in voltage magnitude, such as voltage sag, and transient phenomena, such as switching in the power grid, can result in power oscillation and consequential torsional vibrations in the drivetrain of wind turbines. The source of torsional vibrations can also originate from wind turbine aerodynamics, such as tower shadow and wind speed turbulence. Recent investigations have shown that torsional vibrations in wind turbines can be effectively mitigated by controlling the generator torque using a generator-side converter [30], [24].

The generator torque compensation method can efficiently mitigate torsional vibrations caused by mechanical and electrical events. FACTS devices can mitigate power oscillations in the power grid and resultant torsional vibrations, but they may not effectively mitigate torsional vibrations caused by wind turbine aerodynamics. A compensation torque can be added to the electrical torque using the generator-side converter. Various methods are available to implement compensation torque. For example, virtual inertia controller (VIC) has been used to damp the torsional vibration. In the VIC method, the first derivative of the generator speed is used as the input signal to create a deceleration torque, $-\Delta J\dot{\omega}_R$, which is added to the reference torque only at the dominant drivetrain natural frequency. The generator-side converter can create compensation torque components at dominant drivetrain natural frequencies that are superimposed on the normal torque to suppress the mechanical vibration. This methodology has been implemented in various approaches [7]. In virtual damping, generator speed has been used to create a virtual damping torque at drivetrain natural frequencies in order to mitigate torsional vibration caused by a step change in the generator torque [24].

Another vibration mitigation technique is virtual stiffness or active damping of torsional vibrations caused by tower shadow effect. Resonance occurs when the blades pass in front of the tower. In vibration absorption, a band-pass filter is required around the rotor frequencies. Using the generator speed, the controller regulates the generator torque to damp the dominant modes of vibration based on feedback control. This method is addressed in [35], [36]. FACTS devices can diminish resonance in the electrical side. For example, a gate controlled series capacitor (GCSC), that contains a pair of switches in parallel with the capacitor to enable control of the transmission line effective reactance and power flow, has been used for (SSR) damping [26].

In this chapter, a new nonlinear control scheme based on the sliding mode control theory is proposed to damp drivetrain torsional vibrations. In contrast to existing techniques, the control scheme applies two state variables, rotor speed and position, in order to adjust the rotor current through the rotor-side converter. The proposed technique is verified using a comprehensive model of 750kW DFIG-based and PMG-based wind turbines that includes a full order model of the generator, converters, multi-mass drivetrain, and transmission line with series compensator, all of which are integrated into the FAST aerodynamics wind turbine simulation model, as discussed in Chapters 2 and 3.

5.2 Turbine-Drivetrain Dynamics

The drivetrain dynamics include the rotor, the gearbox, and the generator. In the study of torsional vibrations, a detailed model of gearbox must be studied. As mentioned, a five-mass drivetrain of a 750 kW wind turbine is used in this work. In general, the five-degree-of-freedom model has five natural frequencies that can be described by the following differential equations

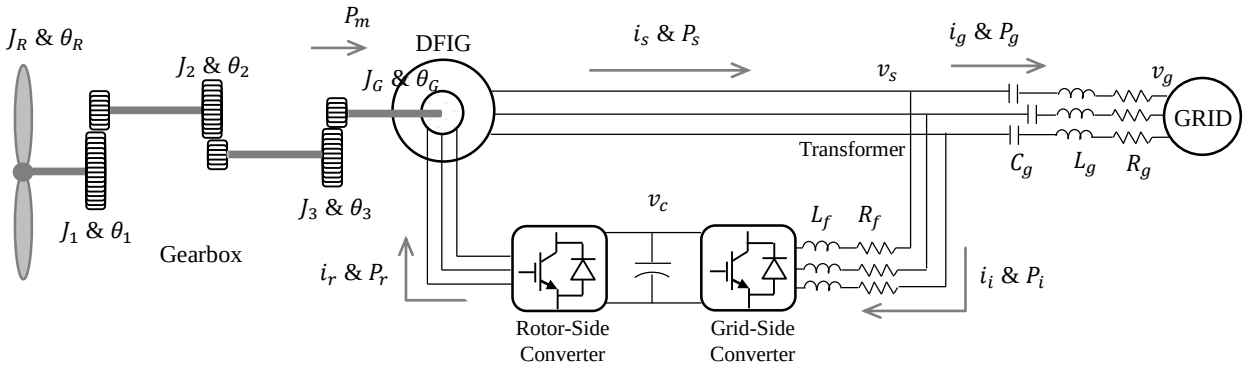

Figure 5.2 Schematic of a DFIG based wind turbine system including five mass drivetrain

$$J_R \frac{d\omega_R}{dt} = T_{aero} - K_1(\theta_R - \theta_1) - D_1\,(\omega_R - \omega_1) \tag{5.2.1}$$

$$J_i \frac{d\omega_i}{dt} = K_i(\theta_{i-1} - \theta_i) + D_i\,(\omega_{i-1} - \omega_i) - K_{i+1}(\theta_i - \theta_{i+1}) - D_{i+1}\,(\omega_i - \omega_{i+1}) \tag{5.2.2}$$

$$J_G \frac{d\omega_G}{dt} = K_4(\theta_3 - \theta_G) + D_4\,(\omega_3 - \omega_G) - T_e \tag{5.2.3}$$

where, $J_i\ \{i = 1, 2, 3\}$ represents the lumped moments of inertia for each mass, K_i represents the stiffness value of each shaft stage, and $D_i\ \{i = 1, 2, 3\}$ represents the viscous damping coefficient. In Equations (5.2.1) through (5.2.3), $\theta_0 = \theta_R$, $\omega_0 = \omega_R$, $\theta_4 = \theta_G$, and $\omega_4 = \omega_G$, as shown in Figure 5.2. For the case study of the 750kW wind turbine, drivetrain inertias and stiffness coefficients referred to the low-speed shaft are given in Tables 5.1, 5.2, and 5.3.

Using (2.4.16), i.e., $f = \frac{1}{2\pi}\sqrt{eig(J^{-1}K)}$ and the data provided in Tables 5.1 through 5.3, the drivetrain natural frequencies are calculated and shown in Table 5.4.

Table 5.1 Five-mass drivetrain gear ratios

N_1	N_2	N_3
4.714	3.565	4.0

Table 5.2 Five-mass drivetrain stiffness coefficient

	K_1	K_2	K_3	K_4
Actual value	3.69×10^7	2.45×10^7	2.70×10^8	2.08×10^6
Referred to LSS	3.69×10^7	5.44×10^8	7.62×10^{10}	9.39×10^9

Table 5.3 Five-mass drivetrain moment of inertias

	J_R	J_1	J_2	J_3
Referred to LSS	998138.4	139.4	817.8	1327.4

Table 5.4 Five-mass drivetrain natural frequencies

f_{n1}	f_{n2}	f_{n3}	f_{n4}	f_{n5}
0	2.95	291.9	371.5	1974.2

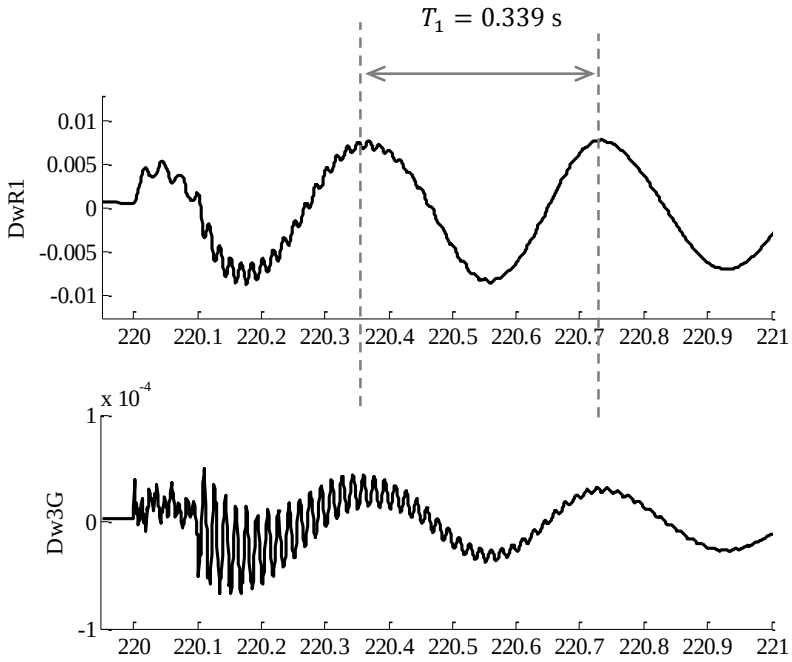

Figure 5.3 Drivetrain internal speeds, $\Delta\omega_{R1}$ and $\Delta\omega_{3G}$, of the five-mass drivetrain

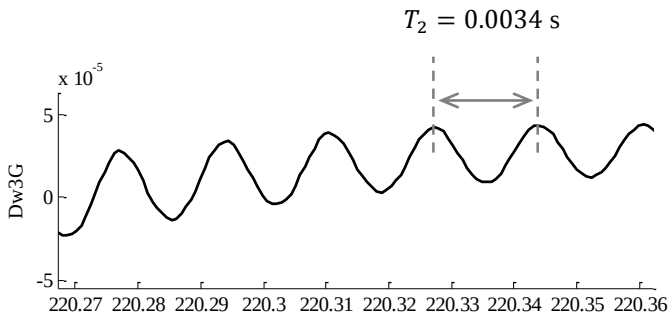

Figure 5.4 Time expansion (zoom) of $\Delta\omega_{3G}$ around 220.3 seconds from Figure 5.3

The dominant natural frequency is 2.95 Hz, when the higher frequencies are inherently suppressed in the low-speed shaft side of the drivetrain, as shown in Figure 5.3. Drivetrain speed differences, $\Delta\omega_{R1} = \omega_R - \omega_1$, and $\Delta\omega_{3G} = \omega_3 - \omega_G$ of the 750kW wind turbine after a voltage dip on the grid (i.e., v_g) are shown in Figure 5.3. It can be seen that, $\Delta\omega_{R1}$ oscillates mainly at a single frequency of 2.95 Hz with the period of 0.339 sec, and $\Delta\omega_{3G}$ waveform has 2.95 Hz oscillation and higher frequencies including the 291 Hz with the period of 0.0034 sec, as shown in Figure 5.4. These two frequencies are the natural frequencies of the drivetrain that are excited after a voltage dip disturbance.

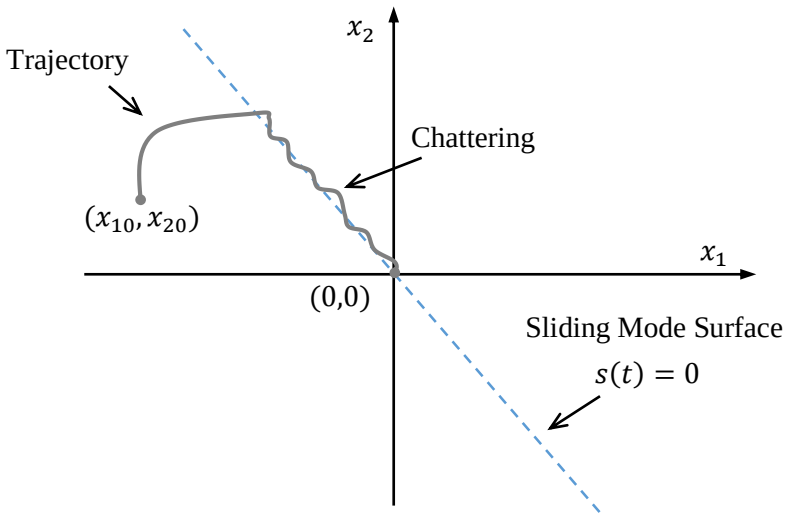

Figure 5.5 Graphical demonstration of the sliding model control theory

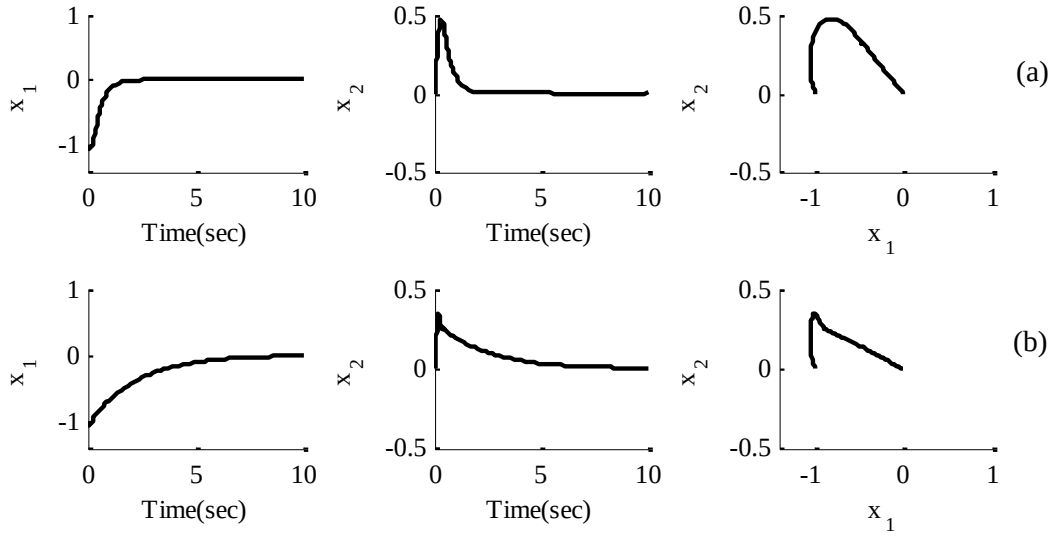

Figure 5.6 State variables and state trajectories after applying two sliding mode surfaces

5.3 Sliding Mode Control Scheme - Background

The sliding mode theory provides a robust control approach for controlling nonlinear systems in which the nonlinear term is unknown or uncertainties exist in the system parameters. In this theory, a surface is built in terms of the state-space variables of a dynamic system, $s(t)$, which is also called a switching surface (manifold). If the system state trajectory is "above" the surface (i.e., $s(t) > 0$), a feedback path (or control signal) has one gain value and a different gain if the trajectory locates "below" the surface (i.e., $s(t) < 0$). Therefore, the switching control law is designed to drive the trajectory of state variables on the surface towards an equilibrium point. Although the sliding mode controller tolerates parameter uncertainties, an unknown nonlinear term must be bounded by a finite value within the system's operating region. Also, a sliding mode requires fast gain switching; therefore, an oscillatory trajectory may occur as the state variables approach the equilibrium point, called chattering, as shown in Figure 5.5.

The second-order dynamic model used in Chapter 4 can be considered to demonstrate the effectiveness of the sliding mode control. If the sliding mode surface is assumed to be $s = \gamma x_1 + x_2$, $\gamma > 0$, then the objective is to force the trajectory of state variables to slide on the line of $s(t) = 0$, or $\gamma x_1 + x_2 = 0$, towards the equilibrium point $(0,0)$. This can be achieved using a switching control law such as $u = \gamma x_1 + \rho sgn(s)$. Simulation results for two sliding mode surfaces (e.g., $s_1 = 0.7x_1 + x_2$ and $s_2 = 0.3x_1 + x_2$) are shown in Figure 5.6 (a) and (b), respectively.

5.4 Proposed Torsional Mitigation Technique

The proposed mitigation technique can be formulated based on the equation of motion for the dominant sub-synchronous eigenvalue as

$$\frac{d}{dt}\begin{bmatrix}\tilde{\theta}_G \\ \tilde{\omega}_G\end{bmatrix} = \begin{bmatrix}0 & 1 \\ 0 & 0\end{bmatrix}\begin{bmatrix}\tilde{\theta}_G \\ \tilde{\omega}_G\end{bmatrix} + \frac{1}{J}\begin{bmatrix}0 \\ (\tilde{T}_{aero} - \tilde{T}_e)\end{bmatrix} \tag{5.4.1}$$

where the $(\tilde{T}_{aero} - \tilde{T}_e)/J$ term can be rewritten as a summation of a compensation torque, u , and an unknown disturbance function, $f_D(\tilde{\theta}_G, \tilde{\omega}_G, t)$, representing an electrical and/or mechanical disturbance signal at the corresponding dominant sub-synchronous eigenvalue (i.e., the 2.95 Hz of the five-mass drivetrain of the 750kW wind turbine). Therefore, Equation (5.4.1) can be written as

$$\frac{d}{dt}\begin{bmatrix}\tilde{\theta}_G \\ \tilde{\omega}_G\end{bmatrix} = \begin{bmatrix}0 & 1 \\ 0 & 0\end{bmatrix}\begin{bmatrix}\tilde{\theta}_G \\ \tilde{\omega}_G\end{bmatrix} + \begin{bmatrix}0 \\ f_D(\tilde{\theta}_G, \tilde{\omega}_G, t) + u\end{bmatrix} \tag{5.4.2}$$

The problem is to design a feedback control law that damps rotor speed oscillation, $\tilde{\omega}_G$, caused by an unknown disturbance. For the system described in (5.4.2) with no unknown disturbances, a feedback control law would be sufficient to damp the shaft speed oscillations. Using the concept of sliding mode control theory, shaft speed oscillations at the dominant natural frequency of the

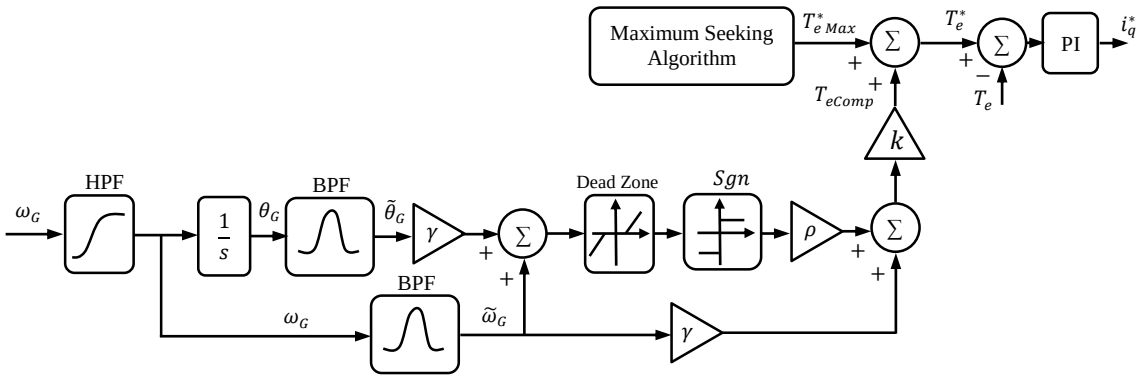

Figure 5.7 Proposed sliding-mode control schematic to mitigate torsional vibrations

drivetrain can be damped even in the presence of a nonlinear time-varying disturbance. The sliding mode variable or surface, σ, is added to the state variables of the system as

$$\sigma = \tilde{\omega}_G + \gamma\tilde{\theta}_G \tag{5.4.3}$$

and its time derivative can be written as

$$\dot{\sigma} = u + f_D\left(\tilde{\theta}_G, \tilde{\omega}_G, t\right) + \gamma\tilde{\omega}_G. \tag{5.4.4}$$

If a Lyapunov function is chosen as

$$V = \frac{1}{2}\,\sigma^2 + \frac{1}{2}\,k\gamma^2\tilde{\theta}_G^2 \geq 0, \tag{5.4.5}$$

then, the input signal, u, must be found such that oscillations of the $\tilde{\omega}_G$ and $\tilde{\theta}_G$ asymptotically approach zero (i.e., $\sigma = 0$), meaning that the time derivative of the Lyapunov function must be a non-positive value. Therefore, the control signal u, is computed to satisfy the above condition and drive the variable σ to zero in finite time. The time derivative of the Lyapunov function is

$$\dot{V} = \sigma\dot{\sigma} + k\gamma^2\tilde{\theta}_G\dot{\tilde{\theta}}_G. \tag{5.4.6}$$

Using (5.4.4), $\dot{V}$ can be rewritten as

$$\dot{V} = \sigma\left(u + f_D\left(\tilde{\theta}_G, \tilde{\omega}_G, t\right) + \gamma\tilde{\omega}_G\right) + k\gamma^2\tilde{\theta}_G\tilde{\omega}_G. \tag{5.4.7}$$

Assuming $u = -\gamma k\tilde{\omega}_G - \gamma\tilde{\omega}_G + v$ and substituting it into (5.4.7) results in

$$\dot{V} = -\gamma k\tilde{\omega}_G^2 + \sigma f_D\left(\tilde{\theta}_G, \tilde{\omega}_G, t\right) + \sigma v \leq -\gamma k\tilde{\omega}_G^2 + |\sigma|L + \sigma v\,. \tag{5.4.8}$$

where $L > 0$ is the maximum probable value of $f_D\left(\tilde{\theta}_G, \tilde{\omega}_G, t\right)$. Equation (5.4.8) can be rewritten as

$$\dot{V} \leq -\gamma k\tilde{\omega}_G^2 + |\sigma|\left(L + \frac{\sigma}{|\sigma|}v\right). \tag{5.4.9}$$

In order to enforce $\dot{V} \leq 0$, v must be selected as $-\rho k sgn(\sigma)$, where $\rho k > L$ and $sgn(\sigma)$ is the signum function. Therefore, a compensation torque, which is added to the desired torque, is defined as

$$T_{eComp} = -u = (k+1)\gamma\tilde{\omega}_G + k\rho sgn(\sigma). \tag{5.4.10}$$

In order to achieve a smooth response with less chattering in the control signal, T_{eComp}, the sgn function can be replaced by $\sigma/(|\sigma| + \varepsilon)$ for a small value of $\varepsilon > 0$. In order to extract the dominant frequency component of the generator-side rotor angular speed and position (i.e., $\tilde{\omega}_G$ and $\tilde{\theta}_G$), band-pass and high-pass filters are used, as shown in Figure 5.7. Also, a dead zone function is utilized to make the $\rho sgn(\sigma)$ component of the compensation torque active only for $|\sigma| > \varepsilon$. For the high-pass filter shown in Figure 5.7, the following fourth-order Bessel filter

$$H_{HP}(s) = \frac{\left(\frac{s}{\omega_c}\right)^4}{\left(\frac{s}{\omega_c}\right)^4 + 10\left(\frac{s}{\omega_c}\right)^3 + 45\left(\frac{s}{\omega_c}\right)^2 + 105\left(\frac{s}{\omega_c}\right) + 105} \tag{5.4.11}$$

is used where ω_c is the cut-off frequency of the high-pass filter. For the low-pass filters, a second-order filter with a center frequency of 2.95 Hz and narrow bandwidth of 1.475 Hz is used as given by

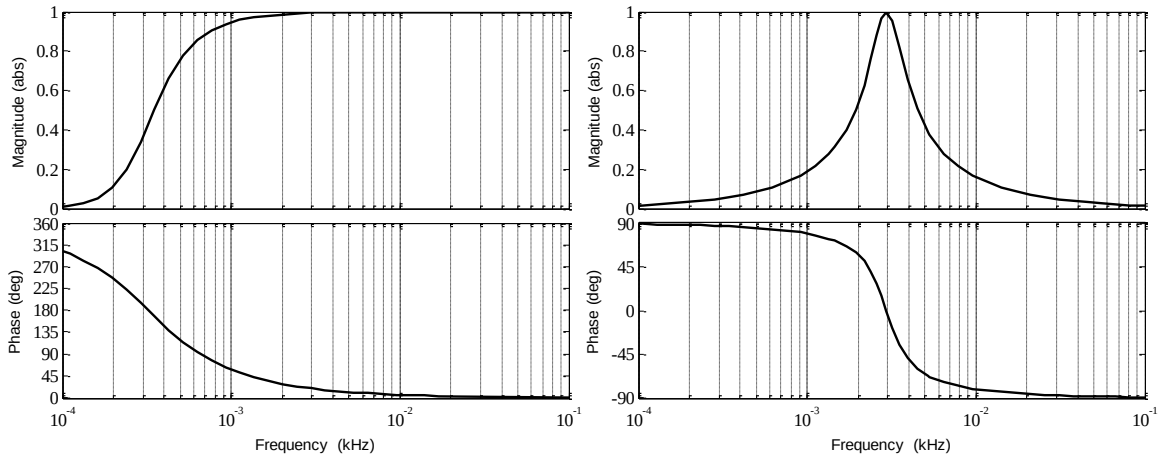

Figure 5.8 The frequency responses of the 4th order Bessel high-pass (left) and 2nd order band-pass (right) filters

$$H_{LP}(s) = \frac{\frac{s}{\omega_0 Q}}{\left(\frac{s}{\omega_0}\right)^2 + \left(\frac{s}{\omega_0 Q}\right) + 1} \tag{5.4.12}$$

where the center frequency is $\omega_0 = 2\pi(2.95) = 18.35$ rad/sec, and $Q = 2$ as the bandwidth is calculated by $\Delta f = f_0/Q$. The frequency responses of these filters are demonstrated in Figure 5.8. The cut-off frequency of the high-pass filter was set to $0.1\ Hz$ to cancel out only the DC component of the generator speed.

5.5 Simulation Verifications and Analysis of Results

In order to investigate the performance of the presented control scheme, the system shown in Figure 5.7 has been entirely modeled in the MATLAB/Simulink environment. The model consists of the NREL 750 kW turbine simulator connected to a DFIG or PMG generator through a five-mass drivetrain/gearbox with gear ratios given earlier in Section 5.2. Parameters of the simulated DFIG and PMG generators are given in Table 5.5 and 5.6, respectively. Notice that, the

Table 5.5 Parameters of the simulated 750kW DFIG

Parameter	Value	Unit
Generator No. of Poles, p	4	----
Generator Stator Rated Voltage	690	V
Stator Resistance, R_s	10.2	mΩ
Rotor Resistance, R_r	10.2	mΩ
Stator Leakage Inductance, L_{ls}	0.1	mH
Rotor Leakage Inductance, L_{lr}	0.1	mH
Magnetizing Inductance, L_M	4.31	mH

generator parameters are transferred into the stator side. Also, the simulated systems contain many subsystems as their formulations were presented in Chapters 2 and 3.

5.6 Comparison of DFIG-based and PMG-based Drivetrain Dynamics

The drivetrain response to mechanical and electrical distortions is different in DFIG-based and PMG-based wind turbines. However, multi-mass drivetrain with multi stage gearbox is typically in DFIG-based wind turbines, and most of PMG-based systems are direct-drive.

Table 5.6 Parameters of the simulated 750kW PMG

Parameter	Value	Unit
Generator No. of Poles, p	8	----
Generator Stator Rated Voltage	690	V
Stator Resistance, R_s	0.426	mΩ
Stator Inductance, L_s	0.654	mH
Flux, Λ_M	825	mWb

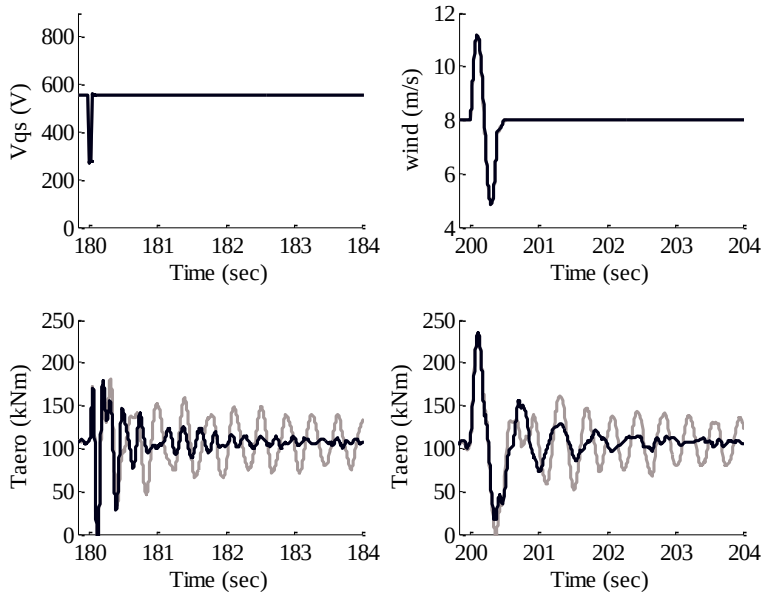

Figure 5.9 Aerodynamic torques, T_{aero}, of the DFIG- based wind turbine after two events: (*i*) voltage dip at t =180 sec and (*ii*) wind speed change at t =200 sec, with (black) and without (gray) compensation

Therefore, the focus of this section is on the test simulated results obtained from the case study 750 kW wind turbine. Four different events are studied in this section. The first two events are (*i*) a 50% voltage dip at t =180 sec for three cycles, and (*ii*) a wind speed swing between 5 and 11 m/s started at t =200 sec for 0.4 sec. These events have been modeled for the DFIG-based system and the corresponding aerodynamic torque profiles are shown in Figure 5.9. The same have done in the PMG-based system and the results are shown in Figure 5.10. The control parameters were held the same in these tests, i.e. $T_{comp} = 15000\ \tilde{\omega}_G + 45sgn(\sigma)$, where $\sigma = 2\tilde{\theta}_G + \tilde{\omega}_G$ and the input signals, $\tilde{\theta}_G$ and $\tilde{\omega}_G$, are referred to the low-speed-shaft.

A comparison between the aerodynamic torque profiles reveals that the electrical disturbance has almost no impact on the aerodynamic torque of the PMG-based wind turbine, but an identical disturbance in the DFIG-based wind turbine can excite the 2.95Hz natural frequency of the 750kW drivetrain. The second observation is that the controller can damp aerodynamic

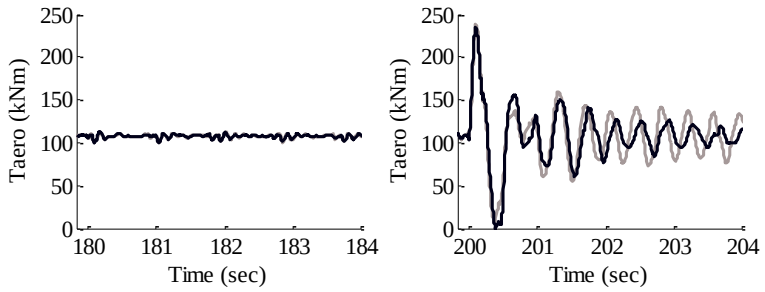

Figure 5.10 Aerodynamic torques, T_{aero}, of the PMG- based wind turbine after two events (i) voltage dip at t =180 sec, and (ii) wind speed change at t =200 sec, shown in Figure 5.9, with (black) and without (gray) compensation

oscillations more effectively in the DFIG-based system. This might be due to the fact that DFIG contributes more to the overall system's damping.

In Figure 5.11, the voltage oscillations in black and gray colors represent the DC-bus voltages of the system for the events shown in Figure 5.9 with and without superimposing compensation torques, respectively. Therefore, the third observation is that active vibration mitigation transfers the stress from mechanical side into the electrical side. Therefore, as the amplitude of the compensation torque increases, the amplitude of the DC-bus overvoltage increases. It should be noticed that all back to back converters have an overvoltage protection system while a designer may implement slightly larger DC-bus capacitor to improve the regulation of the DC-bus voltage.

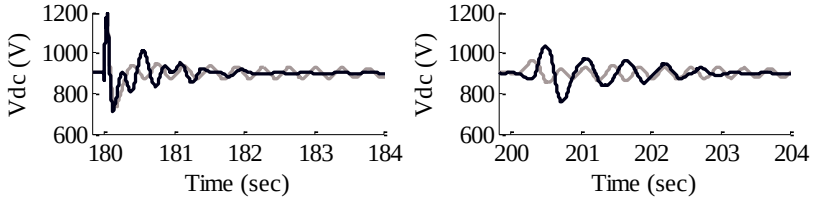

Figure 5.11 The DC-bus voltage oscillations after the events shown in Figure 5.9, with (black) and without (gray) compensation

5.7 Mitigation Technique Response in the DFIG-based System

In this section, the effectiveness of the proposed technique is examined. In Figures 5.12 through 5.15 the simulation results for the first two events (i.e. (*i*) 50% voltage dip, and (*ii*) wind speed variation) are demonstrated. The compensation torque, T_{comp}, and its components, $T_{c1} = k\,\rho\,sgn(\sigma)$ and $T_{c2} = k\,\gamma\,\tilde{\omega}_G$ (where $k = 7500$, $\gamma = 2$, and $\rho = 6 \times 10^{-3}$), for the two aforementioned events are demonstrated in Figure 5.12. In these tests, the sgn function was replaced by $\frac{\sigma}{|\sigma|+\varepsilon}$ (where $\varepsilon = 0.15 \times 10^{-3}$) cascaded by a dead-zone function to eliminate the chattering phenomenon described in Section 5.3. As in Figure 5.12, T_{c1} has rectangular bang-bang pulses with smooth edges, in which, the level of smoothness is a function of the ε value. Also, T_{c1} becomes zero for the input σ magnitudes less than a predetermined value set in the dead-zone block in Figure 5.7. The left and right columns in Figures 5.13 through 5.15 demonstrate control responses to the disturbances shown in Figure 5.9.

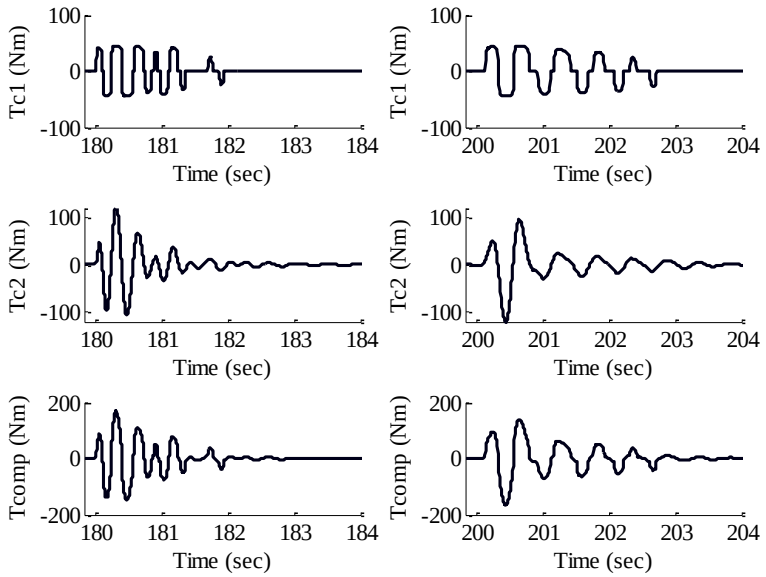

Figure 5.12 Compensation torque, T_{Comp}, and its components (DFIG-based wind turbine) after the two events shown in Figure 5.9

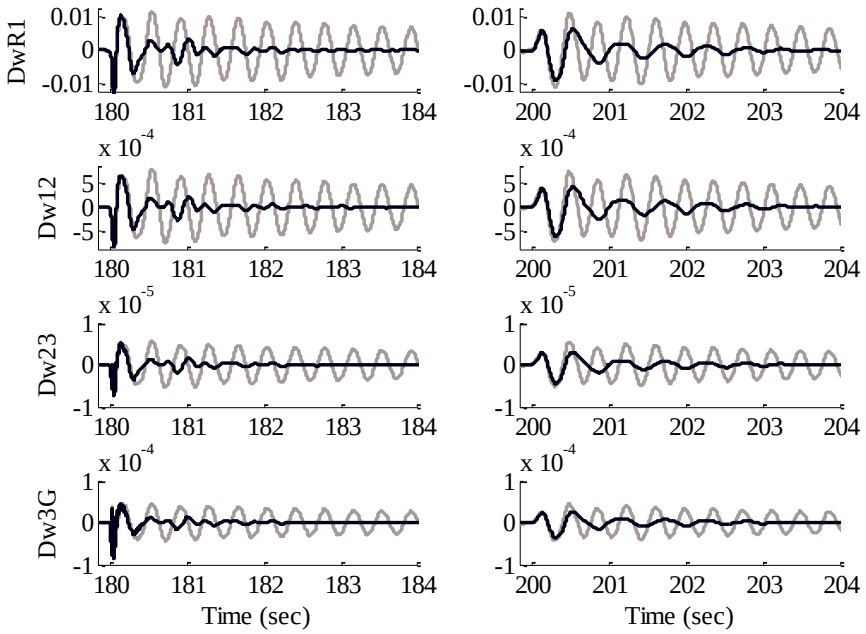

Figure 5.13 Torsional angular speeds, $\Delta\omega_{R1} = \omega_R - \omega_1$, $\Delta\omega_{12} = \omega_1 - \omega_2$, $\Delta\omega_{23} = \omega_2 - \omega_3$, and $\Delta\omega_{3G} = \omega_3 - \omega_G$, in rad/sec for the DFIG-based wind turbine after the two events shown in Figure 5.9, with (black) and without (gray) compensation

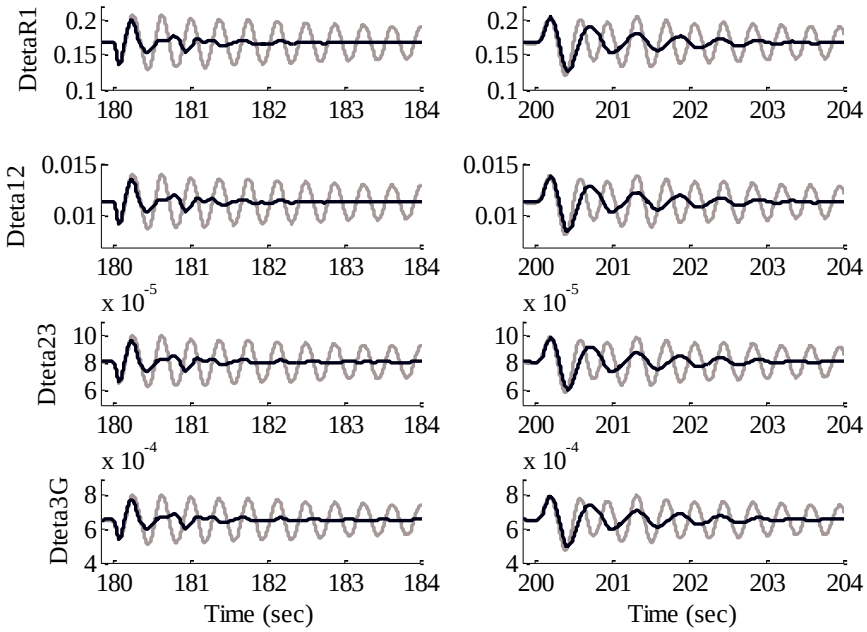

Figure 5.14 Torsional angles, $\Delta\theta_{R1} = \theta_R - \theta_1$, $\Delta\theta_{12} = \theta_1 - \theta_2$, $\Delta\theta_{23} = \theta_2 - \theta_3$, and $\Delta\theta_{3G} = \theta_3 - \theta_G$, in degrees for the DFIG-based wind turbine for the two events shown in Figure 5.9, with (black) and without (gray) compensation

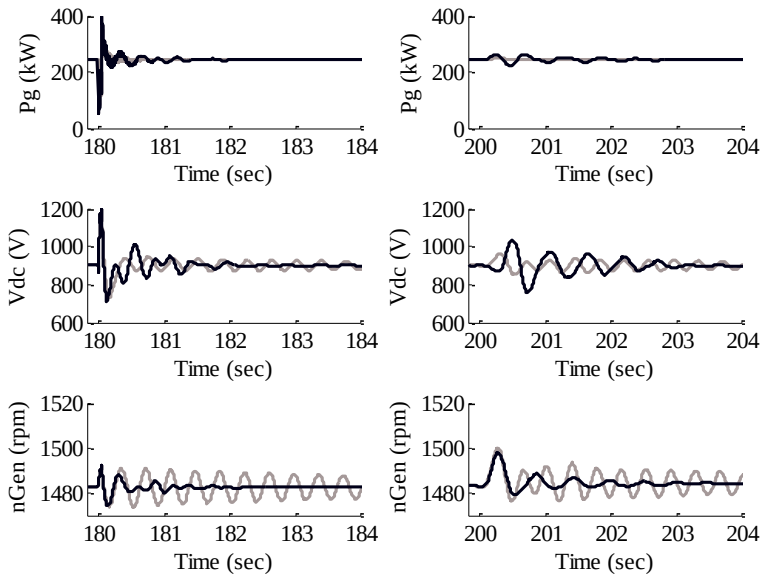

Figure 5.15 Grid power, DC-bus voltage and generator speed of the DFIG-based wind turbine after the two events shown in Figure 5.9, with (black) and without (gray) compensation

Figure 5.13 shows the torsional speeds of the drivetrain gear stages, (i.e. $\Delta\omega_{R1} = \omega_R - \omega_1$, $\Delta\omega_{12} = \omega_1 - \omega_2$, $\Delta\omega_{23} = \omega_2 - \omega_3$, and $\Delta\omega_{3G} = \omega_3 - \omega_G$) for the DFIG system with (black) and without (gray) compensation torque. As demonstrated, these torsional speeds are effectively damped within approximately 1 second.Figure 5.14 shows torsional angles of the drivetrain gear stages (i.e., $\Delta\theta_{R1} = \theta_R - \theta_1$, $\Delta\theta_{12} = \theta_1 - \theta_2$, $\Delta\theta_{23} = \theta_2 - \theta_3$, and $\Delta\theta_{3G} = \theta_3 - \theta_G$), for the DFIG-based wind turbine for the two events. The gray and black waveforms illustrate results obtained from the DFIG-based system with and without compensation, respectively. As shown, the control scheme effectively damps torsional vibrations. Figure 5.15 shows the injected power to the grid, P_g, in kW side by side with the DC-bus voltage, V_{dc}, and the generator angular speed, $n_{Gen} = (60/2\pi)\omega_G$, in rpm after the two disturbances shown in Figure 5.9. As shown, the injected power to the grid asymptotically converge to its initial value approximately 1 second after the disturbances. These simulation results demonstrate the validity and effectiveness of the proposed control scheme.

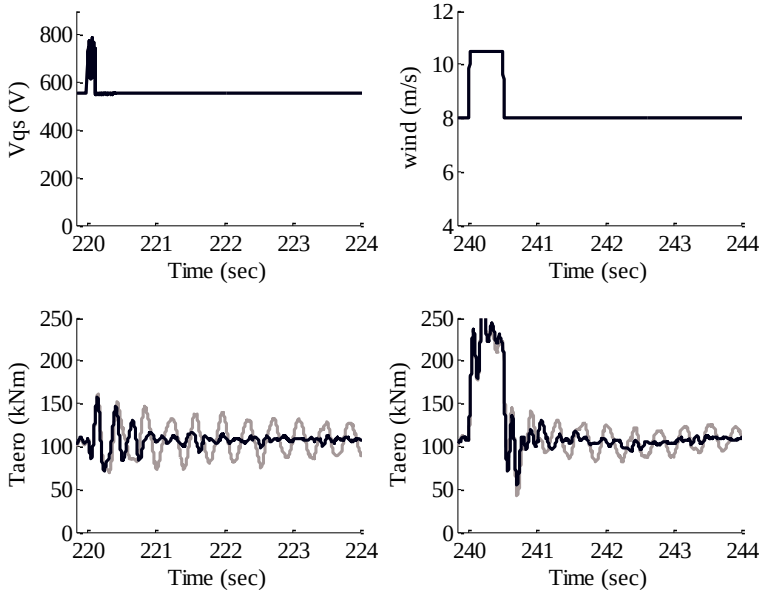

Figure 5.16 Aerodynamic torques, T_{aero}, of the DFIG- based wind turbine after two events (*i*) series capacitor switch causes a voltage swell at t =220 sec, and (*ii*) wind speed change at t =240 sec with (black) and without (gray) compensation

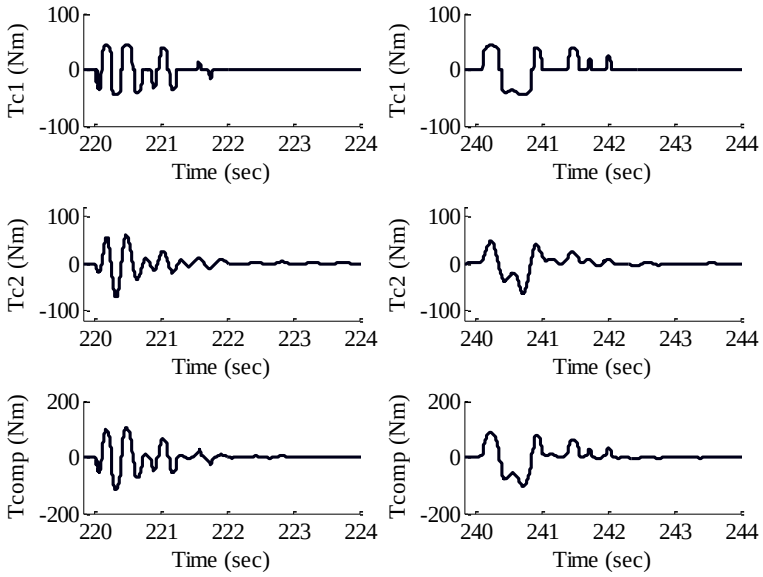

Figure 5.17 Compensation torque, T_{comp}, and its components in the DFIG-based wind turbine after two events shown in Figure 5.16

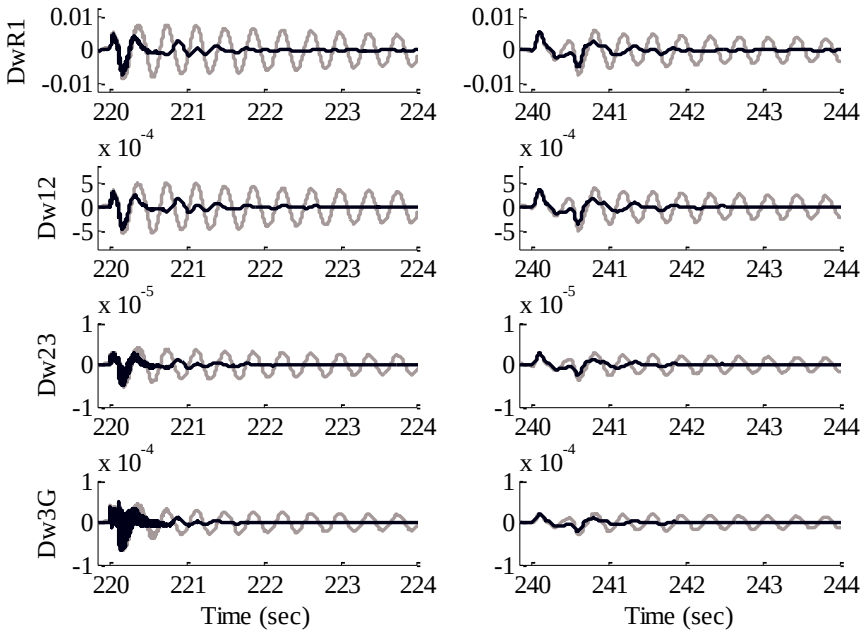

Figure 5.18 Torsional angular speeds, $\Delta\omega_{R1} = \omega_R - \omega_1$, $\Delta\omega_{12} = \omega_1 - \omega_2$, $\Delta\omega_{23} = \omega_2 - \omega_3$, and $\Delta\omega_{3G} = \omega_3 - \omega_G$, in rad/sec for the DFIG-based wind turbine after the two events shown in Figure 5.16

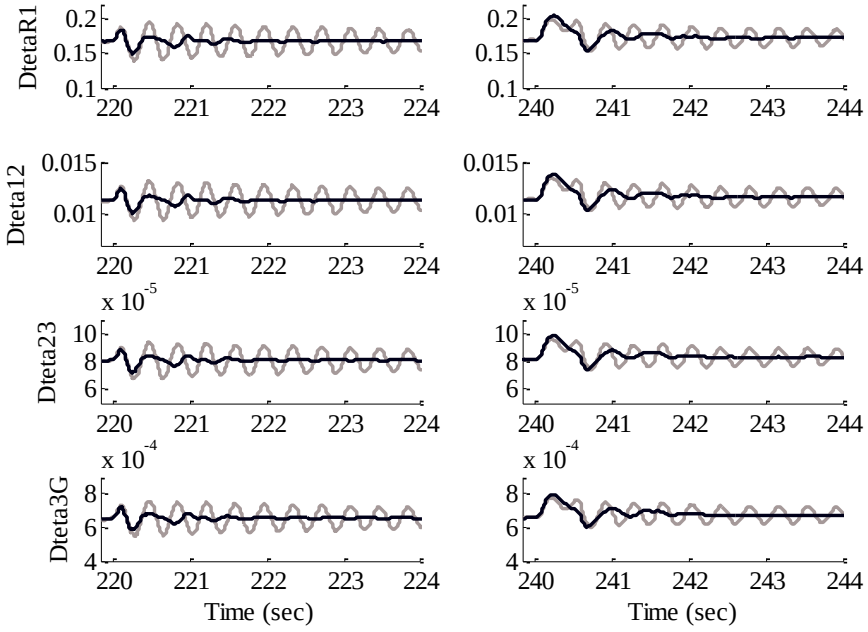

Figure 5.19 Torsional angles, $\Delta\theta_{R1} = \theta_R - \theta_1$, $\Delta\theta_{12} = \theta_1 - \theta_2$, $\Delta\theta_{23} = \theta_2 - \theta_3$, and $\Delta\theta_{3G} = \theta_3 - \theta_G$, in degrees for the DFIG-based wind turbine after the two events shown in Figure 5.16 with (black) and without (gray) compensation

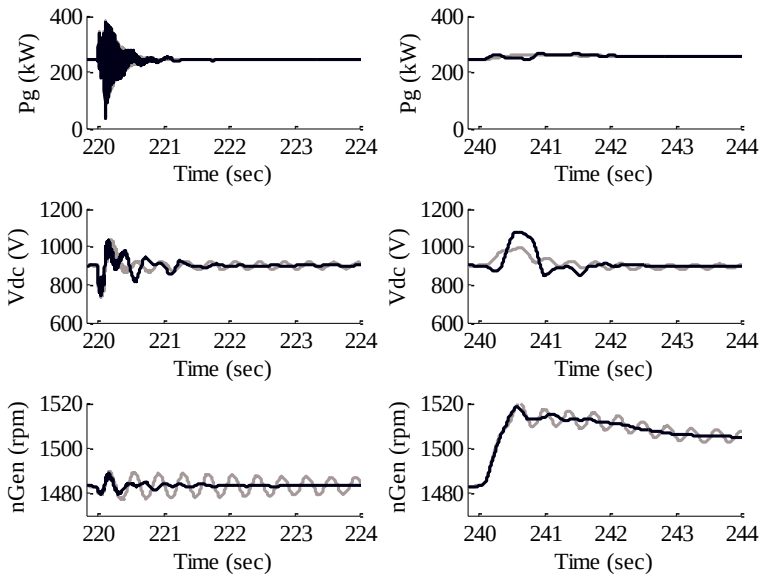

Figure 5.20 Grid power, DC-bus voltage and generator speed of the DFIG-based wind turbine after the two events shown in Figure 5.16

In order to further examine the effectiveness of this technique, simulation results for the two new events are demonstrated in Figures 5.17 through 5.20. Compensation torque formulation and coefficients were kept the same for all cases presented in this chapter. The new events included: (i) switching the 50% series compensation for three cycles between 220 and 220.05 sec and (ii) a sudden wind speed change for 30 cycles (i.e., $30/60 = 0.5$ sec), between 240 and 240.5 sec. As shown in Figures 5.17 through 5.20, use of the proposed technique effectively damped torsional vibrations at the dominant frequency, $f = 2.95Hz$, caused by the case study events.

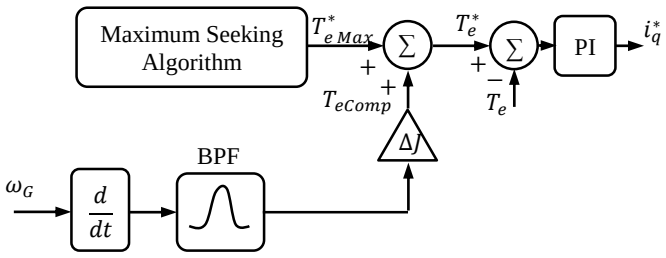

Figure 5.21 Virtual inertia method for damping torsional vibration in wind turbines.

Again, the controller held the same in these tests, i.e. $T_{comp} = 15000\,\tilde{\omega}_G + 45sgn(\sigma)$, where $\sigma = 2\tilde{\theta}_G + \tilde{\omega}_G$ and $\tilde{\theta}_G$ and $\tilde{\omega}_G$, are referred to the low-speed-shaft.

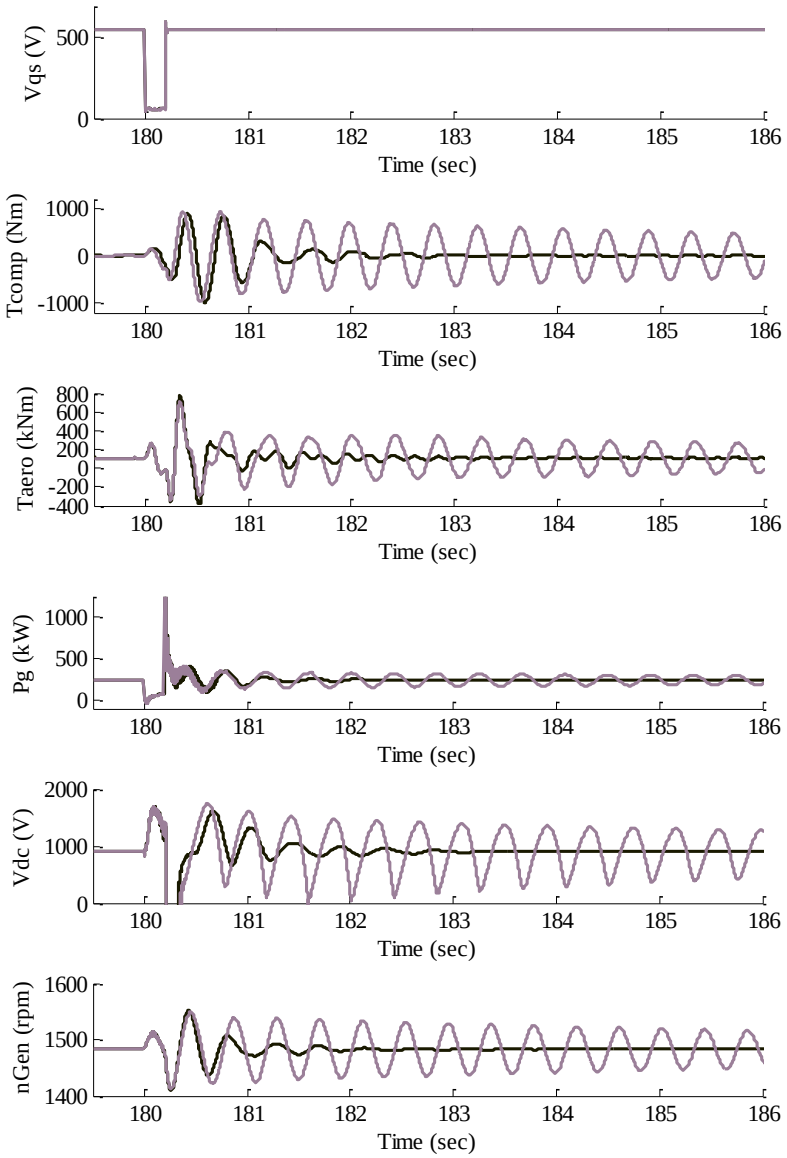

Figure 5.22 The stator voltage, V_{qs}, compensation torque, T_{comp} , aerodynamic torques, T_{aero}, injected power to the grid, P_g, DC-bus voltage, V_{dc}, and the generator speed, n_{Gen} of the 750 kW DFIG- based wind turbine using the proposed (black) vs virtual inertia (gray) methods

5.1 Virtual Inertia Damping Technique Versus the Proposed Technique

This section presents a comparison study between the proposed technique and a recently reported approach [24], called virtual inertia technique. Performance of the proposed vibration mitigation technique is compared with the virtual inertia method is investigated through simulation results

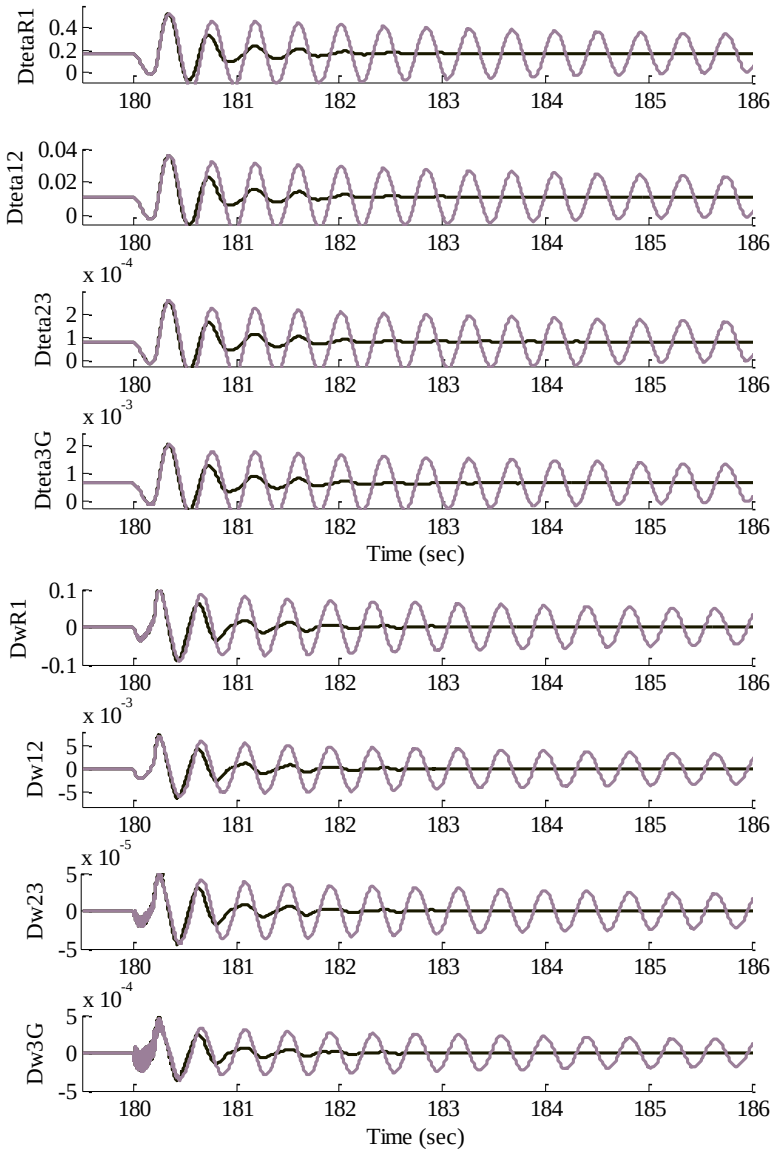

Figure 5.23 Torsional angles in degrees and angular velocities in rad/sec of the 750 kW DFIG- based wind turbine using the proposed (black) versus virtual inertia (gray) damping method

obtained from the 750kW DFIG-based wind turbine system. The virtual inertia damping method, $T_{eComp} = \Delta J \frac{d\tilde{\omega}_G}{dt}$, is demonstrated in Figure 5.21.

Both vibration mitigation methods were implemented in the 750 kW DFIG-based system case study. For comparison and to distinguish the differences, a relatively large disturbance, (i.e, 90% voltage dip at the grid-side) was simulated. In Figures 5.22 and 5.23, the results obtained from the proposed and virtual inertia methods are shown in black and gray colors, respectively.

Although the compensation torque, T_{ecomp} in these tests are almost the same over the first few cycles, the virtual inertia method clearly needs more time to damp the oscillations.

These simulation results have demonstrated that the torsional vibrations in the drivetrain can be mitigated effectively using the proposed technique, and in comparison with the virtual inertia damping method, has superior performance.

Chapter 6 – Conclusion and Future Work

This chapter summarizes the three main contributions to the modeling and control of variable speed DFIG-based and PMG-based wind turbine systems, as presented in this dissertation. Several suggestions for future research paths on the subjects of this dissertation are also provided.

6.1 Summary of Contributions

First, a comprehensive model of electrical subsystems, including back-to-back converters, DFIG and PMG generators, and power lines, as well as multi-mass drivetrain were developed to be easily connected to the FAST simulator. Although main algebraic and differential equations of these subsystems exist in the literature, in this work, the developed models are made to be easily coupled to the FAST simulator in the Matlab/Simulink environment. These models allow investigation of the effects of various control schemes with internal and external disturbance events in wind turbines. The developed models in the Matlab/Simulink environment also provided relatively fast (short simulation time) tools for researchers.

Second, an adaptive nonlinear control scheme for DFIG-based wind turbines was developed using a Lyapunov-based analysis and feedback linearization. The control scheme was built from three control laws including (i) determining the desired generator torque, (ii) estimating the wind turbine power capture coefficient, and, (iii) calculating the desired rotor speed at which the wind turbine captures maximum available wind power. The control scheme adaptively estimated the wind power capture coefficient using real-time wind and rotor speed values. This control system was developed in the Matlab/Simulink environment, and the overall system was simulated using the NREL 5MW FAST reference turbine connected to a developed DFIG, back-to-back converters, and a transmission line between the DFIG and the power grid. The two main control schemes (i.e., power capture coefficient estimation with rotor speed regulation and desired

rotor speed calculation based on maximizing the estimated power capture coefficient), showed robust dynamic behaviors. The role of the controller is to adaptively reach the maximum power capture coefficient as wind speed changes. The significance of the presented technique compared to existing methods is that a perturbation signal was not required. Also, neither the maximum power capture coefficient, nor the optimum tip-speed ratio was assumed as a known parameter. Moreover, the presented technique demonstrated a robust dynamic performance in the presence of wind turbulence and sudden speed changes. Numerical results demonstrated the validity and robustness of the developed control scheme.

Third, the dissertation presented a novel technique based on the sliding mode theory was developed and presented in order to mitigate torsional vibrations in wind turbines using a rotor-side converter. Simulation results demonstrated that torsional vibrations in the drivetrain can be effectively mitigated using the proposed technique. Effectiveness of the proposed control scheme was demonstrated through simulation results of three case studies that evaluated impacts of voltage sag, a wind speed variation, and a series capacitor switching in the power line on the five-mass drivetrain of a 750 kW wind turbine. Furthermore, this technique was compared with the virtual inertia compensation method with voltage dip disturbance. The comparison has demonstrated that the performance of the proposed technique is superior to the recently reported virtual inertia compensation approach for damping torsional vibration.

6.2 Recommended Future Work

In addition to contributions accomplished in this effort, some potential studies are suggested as recommended future work. Potential future work based on results of this dissertation is described in the following paragraphs.

Maximum power capturing in variable speed wind turbines is commonly performed in Region 2, as described in Chapter 2. In Region 3, as wind speed increases, the accelerating torque and rotor speed increases. Therefore, the control strategy in Region 3 regulates power capture at the generator nominal power. During transition between Region 2 and 3, a compensation torque command fed to generator to suppress rotor speed overshoot. Several methods have been reported in the literature, but an optimal nonlinear control scheme that can provide a seamless transition between Region 2 and 3 with minimum stress on the drivetrain is a challenging task as a recommended future work.

The proposed control strategy shows great torsional vibration reduction on the drivetrain of wind turbines as discussed in Chapter 5. The proposed method, as well as other techniques reported in the literature, damps dominant natural frequency of the drivetrain. In these techniques, dominant natural frequency is assumed a known time-invariant design parameter. Also, it is desirable that the control scheme damp all vibration modes over time. Therefore, active dominant modes identification will be significantly helpful because drivetrain stiffness and other parameters change over time.

Bibliography

[1] B. Dudley, "BP energy outlook 2035," British Petrolium, London, United Kingdom, Jan 2014.

[2] "http://www2.epa.gov/energy/learn-about-energy-and-environment," United States Environmental Protection Agency, 8 Oct 2015. [Online]. Available: http://www2.epa.gov/energy/learn-about-energy-and-environment. [Accessed 18 Oct 2015].

[3] "Global Status Report," 2014. [Online]. Available: http://www.gwec.net/wp-content/uploads/2015/03/GWEC_Global_Wind_2014_Report_LR.pdf.

[4] "Renewables 2014 Global Status Report," 2015.

[5] F. Blaabjerg and K. Ma, "Future on power electronics for wind turbine systems," *IEEE Journal of Emerging and selected topics in power electonics*, vol. 1, no. 3, pp. 139 - 152, Sep. 2013.

[6] M. Malinowski, A. Milczarek, R. Kot, Z. Goryca and J. T. Szuster, "Optimized energy conversion systems for small wind turbines," *IEEE Power Electronics Magazine*, vol. 2, no. 3, pp. 16-30, Sep 2015.

[7] I. P. Girsang, J. S. Dhupia, E. Muljadi, M. Singh and J. Jonkman, "Modeling and control to mitigate resonant load in variable-speed wind turbine drivetrain," *IEEE Journal of Emerging and Selected Topics in Power Electronics*, vol. 1, no. 4, pp. 277 - 286, 2013.

[8] B. Connor and W. Leithead, "Control of variable speed wind turbines: Design task," *International Journal of Control,* vol. 73, no. 13, pp. 1189-1212, 2000.

[9] K. E. Johnson, L. J. Fingersh, M. J. Balas and L. Y. Pao, "Methods for increasing region 2 priable-speed wind turbine," *Journal of Solar Eng,* vol. 126, pp. 1092-1100, 2004.

[10] L. Y. Pao and K. E. Johnson, "A tutorial on the dynamics and control of wind turbines and wind farms," in *American Control Conference*, St. Louis, 2009.

[11] M. A. Abdullah, A. M. Yatim, C. W. Tan and R. Saidur, "A review of maximum power point tracking algorithms for wind energy systems," *Renewable and Sustainable Energy Reveiws,* vol. 16, pp. 3220-3227, 2012.

[12] S. Musunuri and H. L. Ginn, "Comprehensive review of wind energy maximum power extraction algorithms," in *IEEE Power and Energy Society General Meeting*, San Diego, CA, 2011.

[13] T. Hawkins, W. N. White, G. Hu and F. D. Sahneh, "Region II wind power capture maximization using robust control and estimation with alternating gradient search," in *American Control Conference*, San Francisco, CA, July 2011.

[14] A. Ghaffari, M. Kristic and S. Seshagiri, "Power optimization and control in wind energy conversion systems using extremum seeking," *IEEE Transactions on Energy Conversion*, vol. 22, no. 5, pp. 1684-1695, Sep. 2014.

[15] R. Chedid, S. Karaki and C. El-Chamali, "Adaptive fuzzy control for wind-diesel weak power systems," *IEEE Transactions on Energy Conversion*, vol. 15, no. 1, pp. 71-78, 2000.

[16] M. g. Simoes, B. K. Bose and R. J. Spiegel, "Fuzzy logic based intelligent control of a variable speed cage machine wind generation system," *IEEE Transactions on Power Electronics*, vol. 12, no. 1, pp. 87-95, 1997.

[17] H. Li, K. L. Shi and P. McLaren, "Neural network based sensorless maximum wind energy capture with compensated power coefficient," *IEEE Transactions on Industrial Application*, vol. 41, no. 6, pp. 2600-2608, Dec 2005.

[18] M. Pucci and M. Cirrincione, "Neural MPPT control of wind generators with induction machines without speed sensors," *IEEE Transactions on Industrial Electronics*, vol. 58, no. 1, pp. 37-47, Jan 2011.

[19] Q. Chen, Y. Li, Z. Yang, J. Seem and J. Creaby, "Self-optimizing-robust control of wind power generation with doubly-fed induction generator," in *IEEE Conference Dynamic Systems and Control*, Cambridge, MA, Sep 2010.

[20] B. Boukhezzar and H. Siguerdidjane, "Nonlinear control of a variable-speed wind turbine using a two-mass model," *IEEE Transactions on Energy Conversion*, vol. 26, no. 1, pp. 149-162, March 2011.

[21] E. Iyasere, M. Salah, D. Dawson, J. Wagner and E. Tatlicioglu, "Optimum seeking-based non-linear controller to maximise energy capture in a variable speed wind turbine," *IET Control Theory & Application*, vol. 6, no. 4, pp. 526-532, 2012.

[22] B. Beltran, T. Ahmed-Ali and M. Benbouzid, "High order sliding –mode control of variable-speed wind turbines," *IEEE Transactions on Industrial Electronics*, vol. 56, no. 9, pp. 3314-3321, Sep 2009.

[23] L. D. Guerra, F. D. Adegas, J. Stoustrup and M. Monros, "Adaptive control algorithm for improving power capture of wind turbines in turbulent winds.," in *American Control Conference*, Montreal, QC, June 2012.

[24] G. Mandic, A. Nasiri, E. Muljadi and F. Oyag, "Active torque control for gearbox load reduction in a variable-speed wind turbine," *IEEE Transactions on Industrial Application*, vol. 48, no. 6, pp. 2424-2432, Nov/Dec 2012.

[25] J. Licari, C. E. Ugalde-Loo and J. B. Ekanayake, "Damping of torsional vibrations in a variable-speed wind turbine," *IEEE Transactions on Energy Conversion*, vol. 28, no. 1, pp. 172-180, March 2013.

[26] H. A. Mohammadpour, R. Y. Shin and E. Santi, "SSR analysis of a DFIG-based wind farm interfaced with a gate controlled series capacitor," in *IEEE Applied Power Electronics Conference and Exposition*, Fort Worth, TX, 2014.

[27] L. Livemore, C. E. Ugalde-Loo, Q. Mu, J. Lian, J. B. Ekanayake and N. Jenkins, "Damping of subsynchronous resonance using a voltage source converter-based high-voltage direct-current link in a series-compensated Great Britain transmission network," *IET Generation, Transmission and Distribution*, vol. 8, no. 3, pp. 542-551, March 2014.

[28] R. K. Varma, S. Auddy and Y. Semsedini, "Mitigation of subsynchronous resonance in a series-compensated wind farm using FACTS controllers," *IEEE Transactions on Power Delivery*, vol. 23, no. 3, pp. 1645-1654, July 2008.

[29] D. W. Novotny and T. A. Lipo, Vector control and dynamics of AC drives, Oxford: Clarendon press, 1996.

[30] I. P. Girsang, J. S. Dhupia, E. Muljadi, M. Singh and L. Y. Pao, "Gearbox and drivetrain models to study dynami effects of modern wind turbines," in *IEEE Energy Conversion Congress and Exposition*, Denver, Colorado, Sep 2013.

[31] J. Jonkman, S. Butterfield, W. Musial and J. Scott, "Definition of a 5-MW reference wind turbine for offshore system development," National Renewable Energy Laboratory, NREL/TP-500-38060, Golden, Colorado, 2009.

[32] M. Singh, E. Muljadi, J. Jonkman, V. Gevorgian, I. Girsang and J. Dhupia, "Simulation for wind turbine generators-with FAST and MATLAB-Simulink modules," National Renewable Energy Labratory, Golden, Colorado, April 2014.

[33] F. Fateh, W. N. White and D. Gruenbacher, "A nonlinear control scheme for extremum power seeking in wind turbine energy conversion systems," in *American Control Conference*, Portland, Oregon, June 2014.

[34] F. Fateh, W. N. White and D. Gruenbacher, "A maximum power tracking technique for grid-connected DFIG-based wind turbines," *IEEE Journal of Emerging and Selected Topics in Power Electronics,* vol. pp, no. 99, pp. 1-9, 2015.

[35] F. Fateh, W. White and D. Gruenbacher, "Mitigation of torsional vibrations in the drivetrain of DFIG-based grid-connected wind turbine," in *IEEE Energy Conversion Congress & Exposition,* Montreal, Quebec, Sep 2015.

[36] W. N. White, F. Fateh and D. Gruenbacher, "Torsional resonance active damping in grid tied wind turbines with gearbox, DFIG, and power converters," in *American Control Conference*, Chicago, Illinois, July 2015.

[37] F. Fateh, W. N. White and D. Gruenbacher, "Torsional vibrations in the drivetrain of DFIG- and PMG-based wind turbines — comparison and mitigation," in *ASME Dynamic Systems and Control Conference,* Columbus, Ohio, 2015.

[38] R. Nobilea, M. Vahdati, J. F. Barlow and A. Mewburn-Crookd, "Unsteady flow simulation of a vertical axis augmented wind turbine: A two-dimensional study," *Journal of Wind Engineering and Industrial Aerodynamics,* vol. 125, p. 168–179, Feb 2014.

[39] F. Iov , M. Ciobotaru and F. Blaabjerg, "Power electronics control of wind energy in distributed power systems," in *International Conference on Optimization of Electrical and Electronic Equipment*, Barsov, Romania, May 2008.

[40] H. Li and Z. Chen, "Overview of different wind generator systems and their comparisons," *IET, Renewable Power Generation,* vol. 2, no. 2, pp. 123-138, 2008.

[41] A. Kushwaha and I. Singh, "Lierature review paper on doubly fed induction generator wind turbine technology," *International Journal of Enhanced Research in Science Technology and Engineering*, vol. 2, no. 9, pp. 44-50, Sep 2013.

[42] A. Gupta, S. N. Singh, R. uttarakhand and D. K. Khatod, "Modeling and simulation of doubly fed induction generator coupled with wind turbine- an overview," *Journal of Engineering , Computers and Applied Science,* vol. 2, no. 8, pp. 45-50, Aug 2013.

[43] S. Benelghali, S. Benbouzid and M. E. H. Charpentier, "Comparison of PMSG and DFIG for marine current turbine applications," in *International Conference on Electrical Machines,* Rome, Italy, Sep 2010.

[44] M. Ragheb and A. M. Ragheb, Wind Turbines Theory - The Betz equation and optimal rotor, Fundamental and advanced topics in wind power, IL, USA: InTech, 2011.

[45] J. M. Jonkman and M. L. Buhl Jr., "FAST User's Guide, NREL/EL-500-29798," National Renewable Energy Laboratory, Golden, Colorado, Aug 2005.

[46] F. Oyague, "Gearbox modeling and load simulation of a baseline 750-kW wind turbine using state-of-the-art simulation codes," National Renewable Energy Laboratory/TP- 500-41160, Golden, Colorado, Feb 2009.

[47] Z. Xing, L. Liang , H. Guo and X. Wang, "Damping contrl study of the drive train of DFIG wind turbine," in *International Conference on Energy and Environmental Technology*, Guilin, Guangxi , 2009.

[48] A. Peterson, T. Thiringer and L. Harnefors, "Modeling and experimental verification of grid interaction of a DFIG wind turbine," *IEEE Transactions on Energy conversion*, vol. 20, no. 4, pp. 875-886, Dec 2005.

[49] B. Novakovic, Y. Duan, M. Solveson and A. Nasiri, "Comprehensive modeling of turbine systems from wind to electric grid," in *IEEE Energy Conversion Congress and Exposition*, Denver, Colorado, Sep 2013.

[50] S. L. Ferreira, J. P. Arruda, F. A. S. Neves, P. A. C. Rosas and M. C. Cavalcanti, "Reduced order model for grid connected wind turbines with doubly fed induction generators," in *IEEE International Symposium on Industrial Electronics*, Vigo, spain, June 2007.

[51] K. E. Johnson, L. Y. Pao, M. J. Balas and L. J. Fingersh, "Control of variable-speed wind turbines," *IEEE Control Systems Magazine*, pp. 70-81, June 2006.

[52] J. E. Slotine and W. Li, Applied Nonlinear Control, Prentice Hall, 1991.

[53] S. Boud and S. Sastry, "On parameter convergence in adaptive control," *Systems & Control Letters 3*, pp. 311-319, Dec. 1989.

[54] P. Cazelitz, W. Kleinkauf, T. Kruger and J. Petsch, "Reduction of fatigue loads on wind energy converters by advanced control methods," in *European Wind energy Conference*, Dublin, Ireland, 1997.

[55] G. M. Masters, Renewable and Efficient Electric Power Systems, New Jersey: John Wiley & Sons Inc., 2004.

[56] Aeolos Wind Energy Ltd, [Online]. Available: http://www.windturbinestar.com/hawt-vs-vawt.html.